A STUDY ON THE MATERIAL CHARACTERIZATION AND FINITE ELEMENT ANALYSIS OF DIGITAL MATERIALS AND THEIR APPLICATIONS

A Thesis

Submitted to the Faculty

of

Purdue University

by

Eduardo Salcedo Lopez

In Partial Fulfillment of the

Requirements for the Degree

of

Masters of Science in Mechanical Engineering

December 2017

Purdue University

Indianapolis, Indiana

THE PURDUE UNIVERSITY GRADUATE SCHOOL
STATEMENT OF COMMITTEE APPROVAL

Dr. Jong E. Ryu, Chair

Department of Mechanical Engineering

Dr. Andres Tovar

Department of Mechanical Engineering

Dr. Diane Wagner

Department of Mechanical Engineering

Approved by:

Dr. Sohel Anwar

Chair of the Graduate Program

To my family and friends.

ACKNOWLEDGMENTS

I would like to begin by thanking my advisor, Dr. Jong E. Ryu, for all the guidance and support he provided throughout the duration of my research. His help allowed me to find an area of interest and pursue my research goals.

Next, I would like to thank the other members of my committee, Dr. Andres Tovar, and Dr. Diane Wagner, for taking the time to review my work. I would like to thank Dr. Tovar for providing invaluable advice and help in several matters throughout my time as a researcher at IUPUI. I would also like to thank Dr. Diane Wagner for providing both the tools and council for conducting the multi-material testing in my research.

I am also much obligated to Dr. Dongcheon Baek for his tremendous help with the testing of the material samples and his advice on several topics related to my research.

My sincerest gratitude also extends to the other researchers in our group who not only made it possible but also fun to conduct research in our lab. I could not have hoped for better lab partners.

Finally, I would like to thank my family and friends whom without I would not have been able to be where I am at. I would also like to acknowledge my parents for their support and encouragement through my whole academic career.

TABLE OF CONTENTS

Page

LIST OF TABLES

LIST OF FIGURES

Figure Page

Figure Page

ABSTRACT

Salcedo Lopez, Eduardo M.S.M.E., Purdue University, December 2017. A Study on the Material Characterization and Finite Element Analysis of Digital Materials and Their Applications. Major Professor: Jong E. Ryu.

Material jetting (MJ) additive manufacturing (AM) has experienced an increased adoption in several industry areas and as well as research applications. One of MJs distinct benefits is the ability to print tunable composites, digital materials (DM) by carefully adjusting the ratio of droplets of heterogeneous base-polymeric inks. However, the lack of material information usable in computer simulations has hampered its acceptance in some end-use applications.

For these materials to be used in Finite Element Analysis (FEA) simulations the mechanical properties of the DMs need to be characterized into usable material models. DMs printable with an MJ printer has a wide variety of materials properties, ranging from flexible silicone rubber to rigid Acrylonitrile Butadiene Styrene (ABS). Therefore, to cohesively express the mechanical behavior of the DMs it is necessary to utilize non-linear material models.

The objective this research is to conduct physical testing to characterize the mechanical behavior of DMs printable with an MJ. Subsequently, to validate the effectiveness of the material models for multi-DM prints. Utilizing the newly characterized material models two use cases were investigated, with the goal of improving the performance of printed parts through simulation.

In this study, an MJ printer was used to fabricate the test specimens as well as the components used in the use case studies. The study was focused on the family of six DMs printable from the mixture of the base polymers Tango Black+ (TB+) and Vero White+ (VW+). To characterize the mechanical properties of the materials a tensile test was conducted utilizing the KS-M6518 standard as a basis. The mechanical

properties of the DMs were then fitted into four non-linear models and the results compared. The fitted models were, the Neo Hookean model, a two-parameter, three-parameter, and a five-parameter Mooney Rivlin model.

To confidently use the material models for multi-DM prints FEA simulations need to validate the accuracy to which they can predict the deformation of the samples under load. To compare the results of the computer simulations and the physical test, strain maps for both results were analyzed. Four different test specimens were printed and tested. A baseline single material samples were compared to three multi-material samples with different embedded structures. The results confirmed the validity of the material models even when used for multi-DM prints.

The recently characterized models are utilized in two use case studies which showcase the potential of DMs. The first use case was focused on printing multi-DM substrates for the use of stretchable electronics. The second use case investigated the benefits of utilizing multiple materials to create 3D conductive traces utilizing a new method, the swollen-off method. Both case studies showed the benefits of utilizing DMs as well as the applicability of the material models in predictive simulations.

1. INTRODUCTION

1.1 Motivation

Additive Manufacturing (AM) is growing trend in industrial applications as well as several research fields, however, in the area of computer simulations, the available information is still lacking. Computer simulations require information pertinent to manufacturing method and materials used, information that is either unknown or not provided by the supplier. Material properties for parts created by conventional methods such as subtractive and trans formative manufacturing are commonly known and used in computer simulations making it easy to predict the behavior of finished parts. The lack of information on the mechanical properties of parts created by AM is a major technological barrier for its adoption in end-use applications.

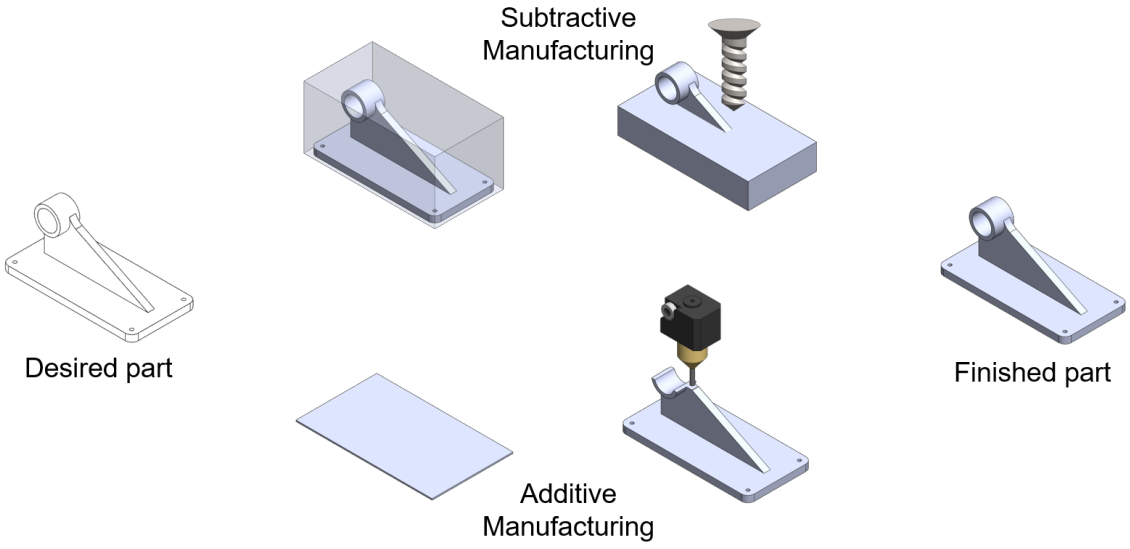

Figure 1.1. A comparison between subtractive, and additive manufacturing methods.

Current industry trends show the use of AM growing, specifically in the creation of pre-production models and iterative prototyping. This growth, however, has not translated into more end-use applications, with only a few cases of AM being used for parts that go into final applications. These end-use applications tend to be low production runs, bespoke parts or specific cases that make use of the benefits of AM. As opposed to conventional subtractive or transformative manufacturing technologies, AM can create complex free form geometries and internal hierarchical structures that would otherwise be impossible to make [1].AM has seen adoption in fields that require custom solutions not suitable for common mass manufacturing methods such as in the medical [2–5], aerospace [6, 7] and research fields, from optics [8, 9] to microfluidics [10, 11]. As the different AM technologies mature the range of printable materials grows, and it becomes possible to print reinforced composites [12–14], conductive materials [15–17], surgically implantable materials [18], and biological tissue [19, 20]. Furthermore, the ability to produce hierarchical structures at a small scales allows for novel applications such as biomimetic designs that are easily implantable [21], and novel structural metamaterials that have the capability of buckling on demand [22].

Research into new materials and the effects of complex structural arrangements has increased tremendously both from manufacturers trying to provide better value to the printers they sell and academics looking for novel applications to this technology. Functionally graded materials (FGM) produced through AM have the distinction of being an overlap of these two areas of research as they are created based on novel structural and material mixture arrangements [23]. FGMs are advanced materials that are volumetrically described by variations in composition and structure. There are naturally occurring examples of these materials such as the structures of bones which are naturally tailored to be lightweight yet sufficiently strong to withstand heavy loading [24]. To achieve these two seemingly contradictory goals the bone is structured in such a way that the external volume of the bone is composed of a dense area of compact bone and the internal areas filled with a much lighter spongy matrix of bone. Tailoring of engineered FGMs can lead to performance improve-

ments for specific applications such as thin thermal barriers [25] and durable concrete structures [26]. The tuning of properties is conducted by arranging the volumetric distribution materials in a non-homogenously filled space. AM has facilitated the creation of FGM, due to its inherent ability to produce complex structures at the micron level. AM produced FGMs have great potential in the creation of hardware and human interfaces, such as prosthesis sockets as they can produce more naturally fitting devices. Fig. 1.2 shows how gradients between materials are used to create FGMs. FGMs are made up of maxels, or voxels (volumetric units akin to a pixel in 2D) with specific material properties. Their arrangement gives the finished part its specific properties.

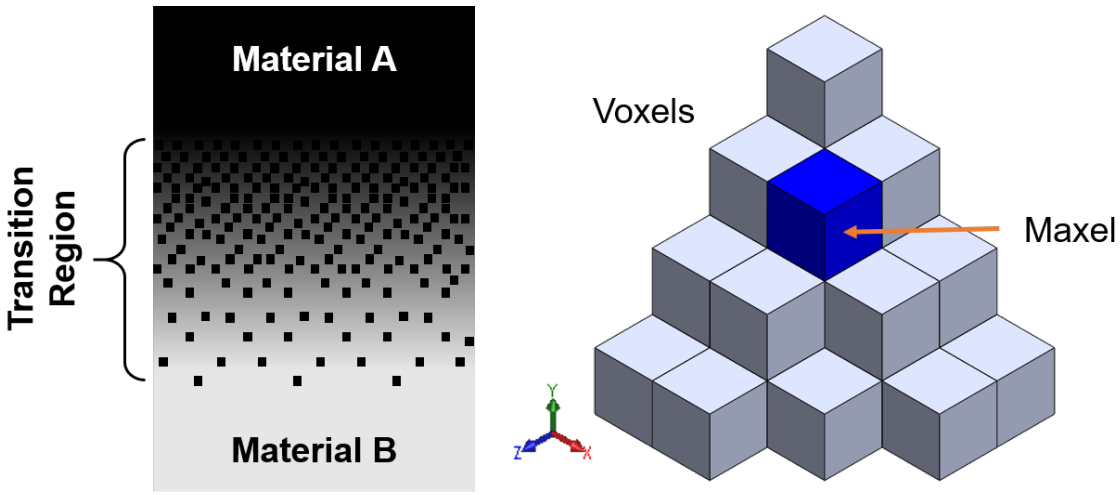

Figure 1.2. Visual representation of an FGM transitioning from one material to another

There are several areas were finely tunable FGMs would be extremely beneficial, currently, there are few methods outside of AM that can achieve this. Its of great importance to spur the adoption of AM in the design and production of parts that might benefit from the use of these materials. The motivation of this research is therefore to remove one of the biggest barriers to the adoption of AM for end-use parts, which is the lack of accurate simulation models for FGMs produced by AM.

1.2 Additive Manufacturing

AM commonly referred to, as 3D printing, is process by which parts are created by the continuous addition of material layer by layer. The method in which material is added can vary widely depending on the chosen technology. As opposed to conventional manufacturing methods, such as subtractive or transformative manufacturing, AM minimizes the amount of material wasted. Furthermore, the inherent benefit of creating a part bottom-up is that complex internal structures can be created and in some cases multi-material distributions finely tuned. The freeform manufacturing capabilities of AM make it suitable for the iterative process in which the design of the components can be readily changed without much cost, or when custom one-off parts are required. Fig. 1.3 shows a schematic of the AM process.

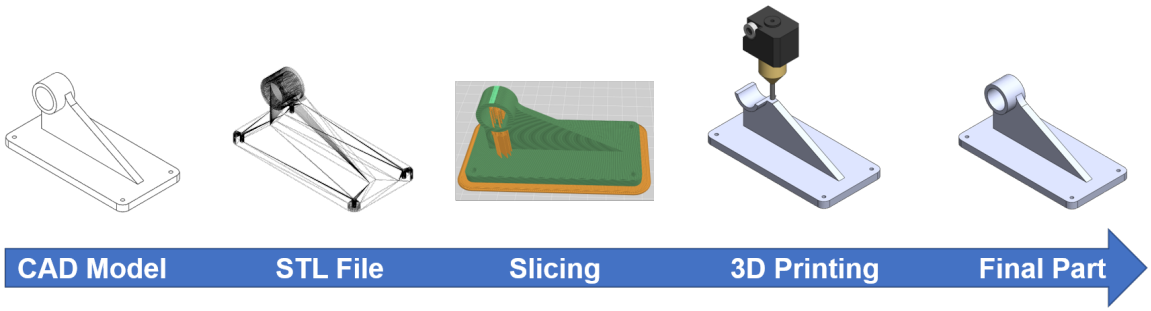

Figure 1.3. Schematic of the Additive Manufacturing process

The taxonomy of AM is divided into seven distinct manufacturing technologies [27]. The distinction between each of these is down to the method in which material is deposited onto the build volume.

Vat Photopolymerization (VP) utilizes radiation curable resins that on irradiation become solid. There are various methods of irradiation ranging from point lasers, UV light, electron beams and light projectors. These systems tend to produce some of the highest resolution, and homogenous material properties.

Powder bed fusion (PBF) processes utilize a thermal source to induce fusion between the powder particles contained in the build tray. Plastics, ceramics, and metals are all printable with this method as long as the proper fusion mechanism is used. Parts produced by PBF have comparable material properties as conventional polymers, metals, and ceramics.

Binder Jetting (BJ), similarly to PBF, BJ works by solidifying powder found in the build tray. Instead of utilizing a thermal source BJ utilizes a binder agent to solidify the powder, these agents can contain different colors or become sacrificial allowing for infiltration process to make denser parts.

Material Jetting (MJ) utilizing similar nozzle printing techniques found in conventional 2D inkjet printers with the obvious distinction of being a layer by layer additive method that creates 3-dimensional objects. The body of this research focuses on this AM method and therefore will be thoroughly explained later.

Direct Energy Deposition (DED) works by melting material as it is being deposited similarly to the wire welding process. DED tends to utilize metal powder to build objects, the added benefit of these systems is that they can be built in such a fashion that they can create objects larger than the printer itself.

Material Extrusion (ME) systems are the most popular due to their simplicity and how inexpensive they are to build and sustain. ME systems work by heating a material above its glass transition phase and extruding it out of a nozzle, this material is then deposited on the print bed where it cools and solidifies, this is repeated layer by layer until a 3D object is built.

Sheet lamination (SL) is unlike any other AM method, it relies on adding a full layer of material cut into the intended shape and adhering it to the previously deposited layers. The materials and adhesion methods utilized can vary greatly, paper and adhesive systems have been commercialized, however, the most well-known system relies on metal sheets and sonic welding.

1.3 Material Jetting and the technical barrier to the adoption of digital materials

MJ works by selectively depositing droplets of uncured resin unto previously deposited layers and then curing them with the use of a UV lamp [28, 29]. MJ printers at a minimum consist of two sets of material jetting heads each containing hundreds of nozzles, one for support material and one for build material. These nozzles utilize piezoelectric actuators to selectively eject uncured resin onto the build platform. Fig. 1.4 shows an example of the working principle in MJ printing.

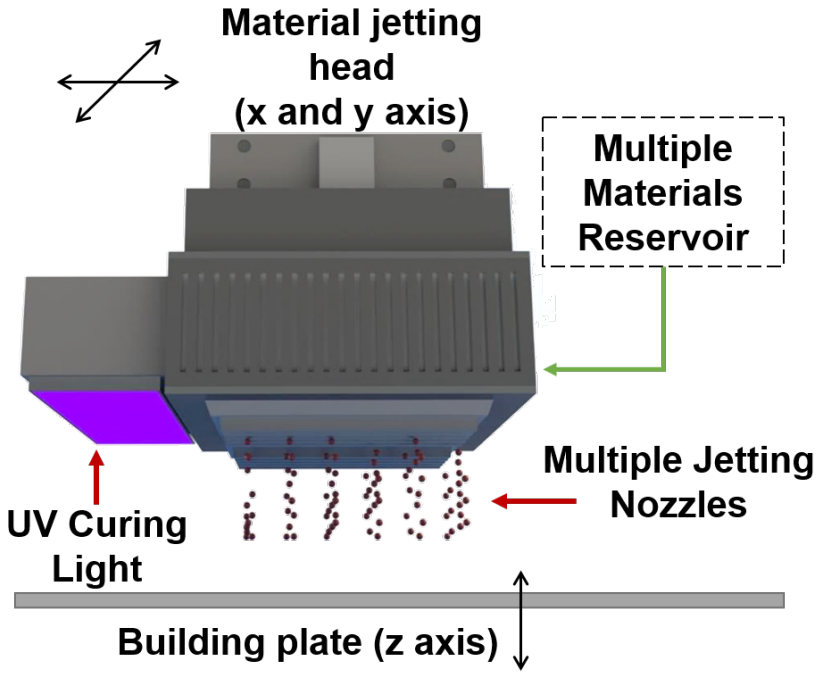

Figure 1.4. Schematic of the printing process for Material Jetting

By adding multiple jetting heads, the printer is able to create composite materials by combining different resins prior to the photopolymerization phase. By adjusting the mixture ratio between the base materials, different mechanical properties can be achieved. These new composites, or Digital Materials (DM), can increase the amount materials properties printable in a given MJ printer. One of the most common families

of DMs are derived by mixing TB+ and VW+, these DMs can be tailored to have material properties that range from silicon rubber to those of ABS. DMs have several uses, they are the only way of producing over-molded parts in AM, they can be used to print photorealistic parts and can also be used as a way of physically mimicking any given material that falls within the material range.

The DM printing capabilities of MJ allow for micro-scale tuning of the material properties of a part, which in turn makes it suitable for manufacturing Functionally Graded Materials (FGM). These types of graded materials can be tailored to specific use cases, therefore, improving their overall performance. Engineered FGMs had previously focused on the creation of these materials through the usage of metal alloys or foam materials which limits their use in some applications, such as hardware-user interfaces, and small devices with complex structures.

In recent years, the usable portfolio of materials capable of being 3D printed has expanded. New materials available range from advanced composites, FDA approved materials and an extended gamut of photo-realistic color dyes. This has led to more end-use parts being made with AM. Despite this growth in material availability, there are applications where the lack of information on the material properties required to run simulation testing impede the usage of AM, while physical testing would be possible the increased time and cost would be counterproductive to the usage of AM. The velocity at which new materials are released has so far outpaced the amount of information available on those same materials. Research has been conducted in characterizing the mechanical properties of different AM technologies such as powder bed fusion, material extrusion , and vat photo-polymerization. This has facilitated the use of simulation software to predict the behavior of parts produced with these technologies; consequently, these technologies have seen greater adoption in the industry.

Research focused on AM printing methods can be grouped into three different phases. Printer parameter studies, material characterization and novel applications. The bulk of the research in each one of the phases usually occurs sequentially, however it is not uncommon to see the effects of new parameters studied as they become available.

The first phase, usually deals with studying the effects of print settings and parameters on the material properties of printed parts (usually tensile strength). These parameters are unique for each AM technology, but some common ones are print orientation, printing speed, and part aging. This occurs first as it is necessary to zero in on the optimal printing parameters.

The second phase, focuses on the characterization of other the material properties. In this phase testing standards are utilized to fully describe the properties of parts printed with a given technology.The mechanical, thermal, dielectric and optical properties are some of the most widely researched.This phase allows for the creation of material models that allow for computer simulations to be conducted. The third phase deals with novel approaches to utilizing the specific AM process. These applications exploit the benefits of a given process to improve the performance on a specific use case.

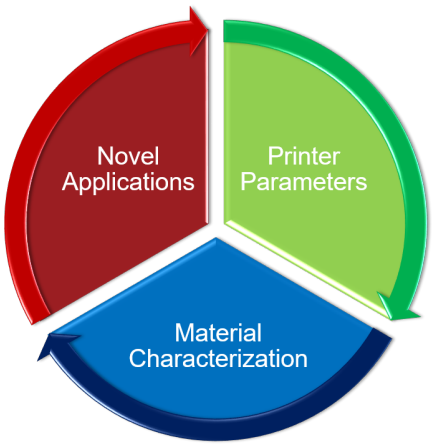

Figure 1.5. Additive Manufacturing research phases

At this point in time most of the research conducted on the MJ process has been focused on the effects of printing parameters on the final mechanical properties of the printed parts. Moreover, the research has centered on the base materials and no thorough body of research exists for DMs. Although this sort of research has yielded a lot of information on the optimal orientations for printing parts, it hasnt made it any easier to conduct computer simulations for MJ printed materials.

Examples of the studies conducted in the first phase of research deal with the print factors that influence the material properties of the finished parts. Initially low dimensional accuracy lead to the study of scaling factors set in the printing software [30], something which has now been solved in new versions of the printing software. The effects of part orientation and spacing have been the focus of several studies [31–33]. Jochen Muller provides a helpful summary of some of the factors that can influence the material properties of MJ [34], which are;

- X-Y position on the build tray
- Orientation of the part (in reference to the 3 axis of the part)
- Part spacing (when printing multiple parts)
- Material expiration date
- Warm-up time of the machine
- Cleanliness of the nozzles
- Storage time (time between print and testing)
- Storage conditions

The characterization phase is of great importance as it allows for the creation of mathematical models that describe the material properties of the printed parts. These models are necessary requirements for conducting computer simulations. However, this is by far the most laborious phase as each model describing a material property requires a specific test, and this test needs to be conducted for each material desired. Some of examples of the properties that have been studied so far are the Thermal [35], dielectric [36], and surface properties [37] for some MJ materials. Additionally, other mechanical properties like the fatigue [38], tensile [39] and relaxation modulus [40] have been researched. Despite all of this research there is not a complete characterization of the mechanical properties that would allow for mechanical simulations to be conducted using all the DMs available.

In the third phase there has been a growing interest in utilizing tunable material distributions to enhance the performance of printed parts. Novel approaches to this have lead to notable improvements in the design of tunable lap joints [41] and bespoke prosthesis sockets [42,43].Other research areas such as topology optimization [44] and soft robotics [45,46] are leveraging this technology to create devices that were previously not manufacturable. Additionally, researchers are utilizing MJ and biomimicry to improve the performance [47] or tune the mechanical response [48] of printed parts to their specific requirements.

In summary, the biggest obstacle stopping MJ from seeing greater adoption is the inability to conduct accurate simulations. Currently, the mechanical information provided by the manufacturer woefully inadequate to conduct any meaningful simulation work. For MJ to be utilized in end-use applications material models the allow for predictive simulation are of great importance.

1.4 Objective

MJ is one of the most advanced AM technologies currently in use, with materials displaying isotropic properties, low post-processing times, fast turnaround and the ability of printing multi-material parts with ease. Despite all the benefits its adoption has paled in comparison of other technologies such as material extrusion and powder bed fusion.

The goal of this research is to characterize the mechanical properties and validate the models required for utilizing DMs in finite element analysis. By comparing different material models and model simplifications the research aims to present the optimal solution for modeling these materials in computer simulations, with the intent of accelerating the adoption of these novel materials into more fields and applications.

By confirming the validity of the models through comparison of simulations and physical tests this research can also aim into present novel case studies were MJ printed DMs improve the performance of different components and systems. Particularly, this research aims to show improvements in the field of stretchable electronics by utilizing 3D tailored substrates to reduce stress concentrations at the interface between rigid components and the elastic substrates. Additionally, a second case study focuses on the benefits of multi-material prints in tandem with computational designed structures to create 3D conductive traces through electroplating and the swollen-off process.

1.5 Approach

This thesis is organized into six chapters following the overall flow of the research. The first chapter is an introduction to the research topic with a focus on the state of AM, and more precisely Digital Materials. A literary review on the subject is presented, culminating in a summary of the technical barriers preventing wide adoption of these materials.

Chapter 2 focuses on the characterization of the DMs, with information on the testing standard, printer, and test specimens. Chapter 3 presents information on the material models utilized in this study as well as the fitting procedures conducted. Chapter 4 presents a validation of the newly found models by comparing simulation results to those of physical testing. Strain maps generated in FEA simulation are compared to those generated in the physical test by using a video extensometer.

Having confirmed the accuracy of the models during multi-material simulations two use cases are studied in Chapter 5. In these case studies, the benefits of utilizing DMs have also been explored as well as the advantages of running preliminary simulations during the development process. Finally, Chapter 6 summarizes the results of this research and presents recommendations relevant to future research on this topic.

2. PHYSICAL TESTING

2.1 Physical tests

The goal of the physical tests conducted in this study is to create material models that satisfy the input requirements for predictive numerical simulations in conventional FEA software packages. The first phase of the characterization process shown in Fig. 2.1, the tensile testing procedure, is explained and the results summarized.

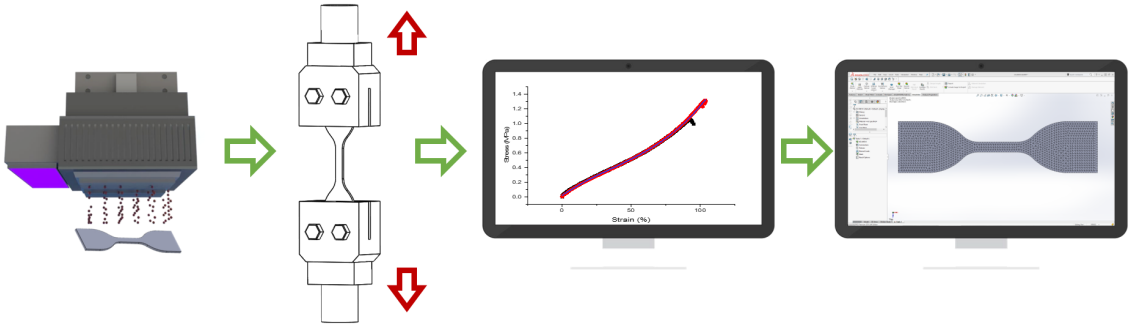

Figure 2.1. Graphical summary of the material characterization conducted in this study

2.2 Considerations and limitations of the characterization procedure

There are several considerations that must be considered when conducting characterization tests on hyperelastic materials, these observations are applicable to a certain degree to most elastomers.

1. The stress-strain response for the first time an elastomer is strained will be unique and wont be repeated on further loading events.

2. The stress-strain response for the elastomer will stabilize after several cycles of loading.

3. The stress-strain response will change if a new maximum strain is experienced, the response will again stabilize after repeated cycles at this new maximum.

4. There is a small amount of permanent deformation after every strain cycle. The material will no longer return to zero strain at zero stress.

5. The compliance of the strain measuring tools (if in contact with the sample) might affect the results.

2.2.1 Considerations for FEA models

Conversely, conventional FEA packages are unable to fully account for all of these material considerations. Therefore, the tests must be chosen in a way that is most representative of the end-use that the simulations are trying to replicate. If repetitive loading at a certain strain is required, the tensile test should replicate these conditions. Some of the limitations that need to be considered are:

1. The material models do not distinguish between the first and the nth straining event, therefore the stress-strain response will be the same regardless of how many strain events the part experiences.

2. The material model is unchanged regardless of the maximum strains experienced by the part.

3. The models are unable to account for permanent deformation, therefore treating the material as perfectly elastic.

2.3 Experimental details

2.3.1 Materials

The specimens used in this test were designed based on the Korean Standard M6518 for vulcanized rubber (Fig. 2.2), an equivalent to the ASTM D638 tensile test standard most widely known in the USA. The samples were designed utilizing a conventional computer-aided design (CAD) software SolidWorks (Dassault Systems). A Connex 500 (Stratasys) MJ printer was utilized to print all the samples, utilizing the base materials VW+ and TB+. Six different combinations of the base materials were investigated; DM40, DM50, DM60, DM70, DM85, and DM95. The naming convention is based on the equivalent Shore A hardness of each material. Therefore, DM40 is a Digital Material with a Shore A hardness of 40.

Stratasys the manufacturer of the Connex 500 provides basic information on the properties of the materials. However, the information is woefully inadequate for conducting any meaningful simulation work. Table 2.1 provides all the information given by the manufacturer in regard to the printable materials.

Table 2.1. Material properties given by Stratasys

	Strain (%)	Stress (MPa)
Tango Black+	170% - 220%	0.8 - 1.5
DM40	110% - 130%	1.3 - 1.8
DM50	95% - 110%	1.9 - 3
DM60	75% - 85%	2.5 - 4
DM70	65% - 80%	3.5 - 5
DM85	55% - 65%	5 - 7
DM95	35% - 45%	8.5 - 10
Vero White+	10% - 25%	50 - 65

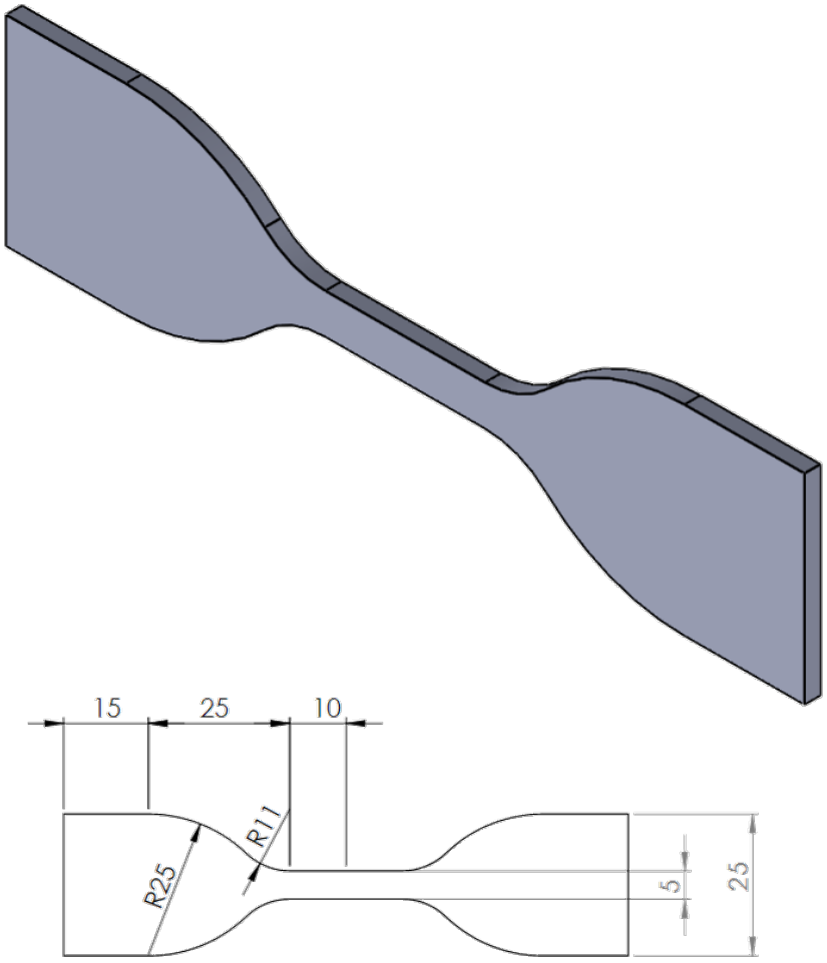

Figure 2.2. Schematic of the Korean Standard test sample

2.3.2 Printing process

After designing the test specimen in CAD, the file was exported in a standard tessellation file (STL) format usable in conventional AM slicer software. The slicer software, Object Studio (Stratasys), is utilized to create the print path for the machine as well as generating any support required. After the required information is sent to the machine, the print begins depositing support material onto the build plate. Then individual nozzles controlled by piezoelectric actuators begin depositing droplets of material resin. Depending on the required DM different ratios of TB+ and VW+ get deposited and mixed on the build plate, after every layer a high-powered UV light

irradiates the printed part solidifying the uncured resin. This process is repeated layer by layer until the full part is printed, at which point the part is removed from the build plate and the support is cleaned off.

The Connex 500 has a limited amount of printing modes and settings available for the users to choose from. The first is printing mode, this controls the layer height and therefore the speed and resolution of the printed part. When only utilizing the base materials users can select either a fast print option with a layer height of 30-microns or a high-resolution option with 16-micron layer height. The DM printing mode is used for default when printing composites, in this mode the layer height is set at 30-microns. Secondly, the user can select from two finishing options, glossy or matte. When printing with the matte option the printed part is encased in support material giving the whole part a matte finished, whereas when using the glossy option support material is only deposited in the required areas. Finally, users can select from 3 support settings lite, standard and heavy.

The printing settings used for this study are:

1. DM printing mode.
2. Matte finish.
3. Standard support.

2.3.3 Tensile test

In this study, we focused on one of the most used characterization tests, the uniaxial tensile test. This is test provides sufficient information on the relationship between the base material and the DMs created by their mixture to run FEA simulations. The tensile test was conducted as a single pull-to-break test, with no cyclical loading used for the material models. Although the Mullins effect is important in the most elastic DMs, however, its effects become negligible at the rigid end of the DM catalog and therefore it was decided to only test at single pull. For highly elastic

elastomers stress-strain curves can be strain rate dependent, something not observed in the more rigid DMs. To minimize its effect in the lower end of the DM range the test was conducted at a slow speed (50mm/min) approaching a quasi-static state. Fig. 2.3 shows a schematic of the testing procedure.

The testing was conducted with an Instrom 5567 universal testing machine (UTM). Samples were loaded onto the machine, with both sides securely gripped (Fig. 2.4). A small amount preload is added to neglect the effects of the material bulging during the gripping phase. Strain readings are measured with a contact extensometer that is clamped onto the gauge length of the test sample, while a load cell attached to one of the grips measures the load. The test is conducted at a strain rate of 50mm/min and is concluded when the sample breaks and the load cell registers a drop. The testing machine automatically calculates the strain, stretch, and stress for each material.

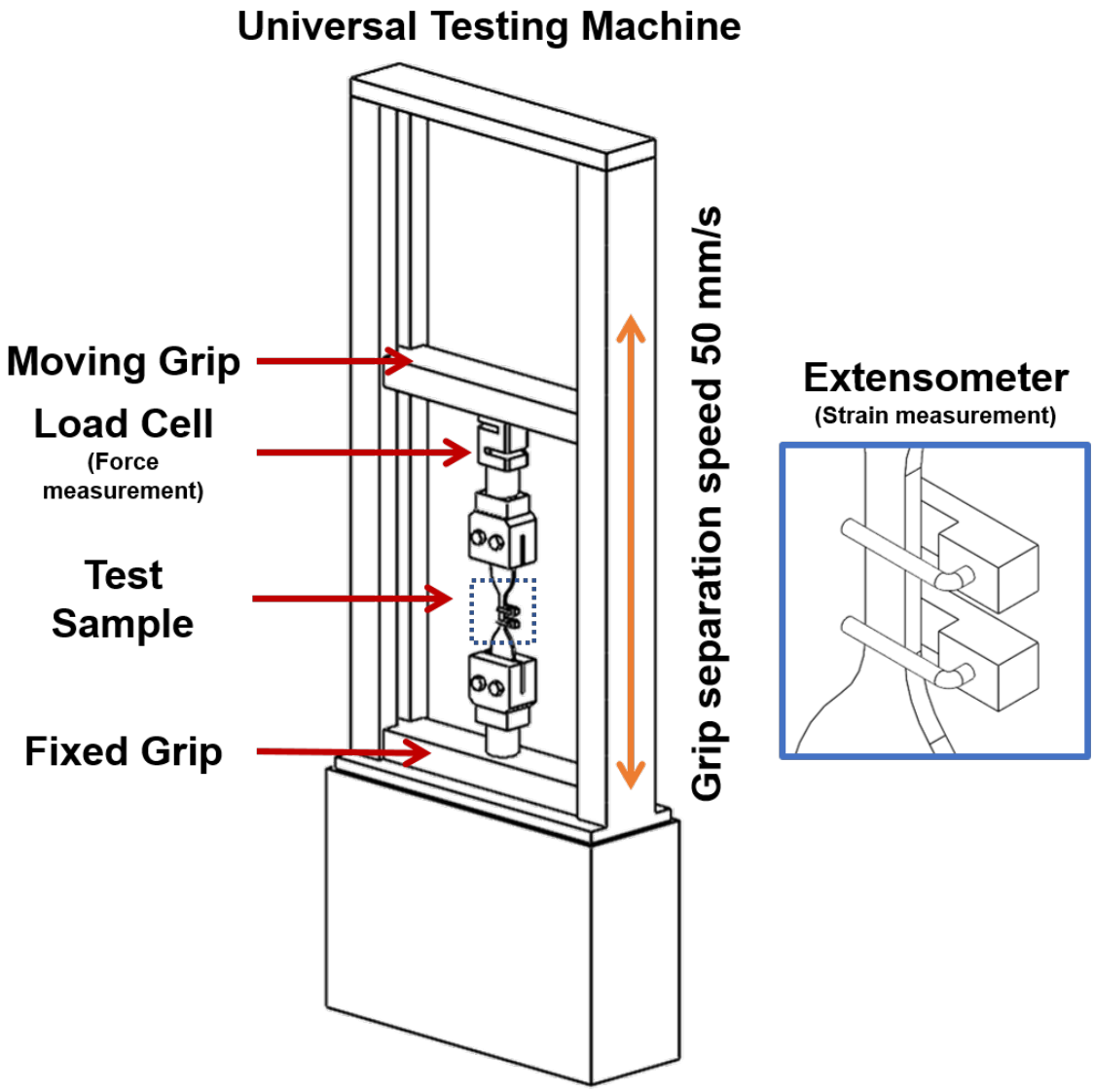

Figure 2.3. Schematic of the test

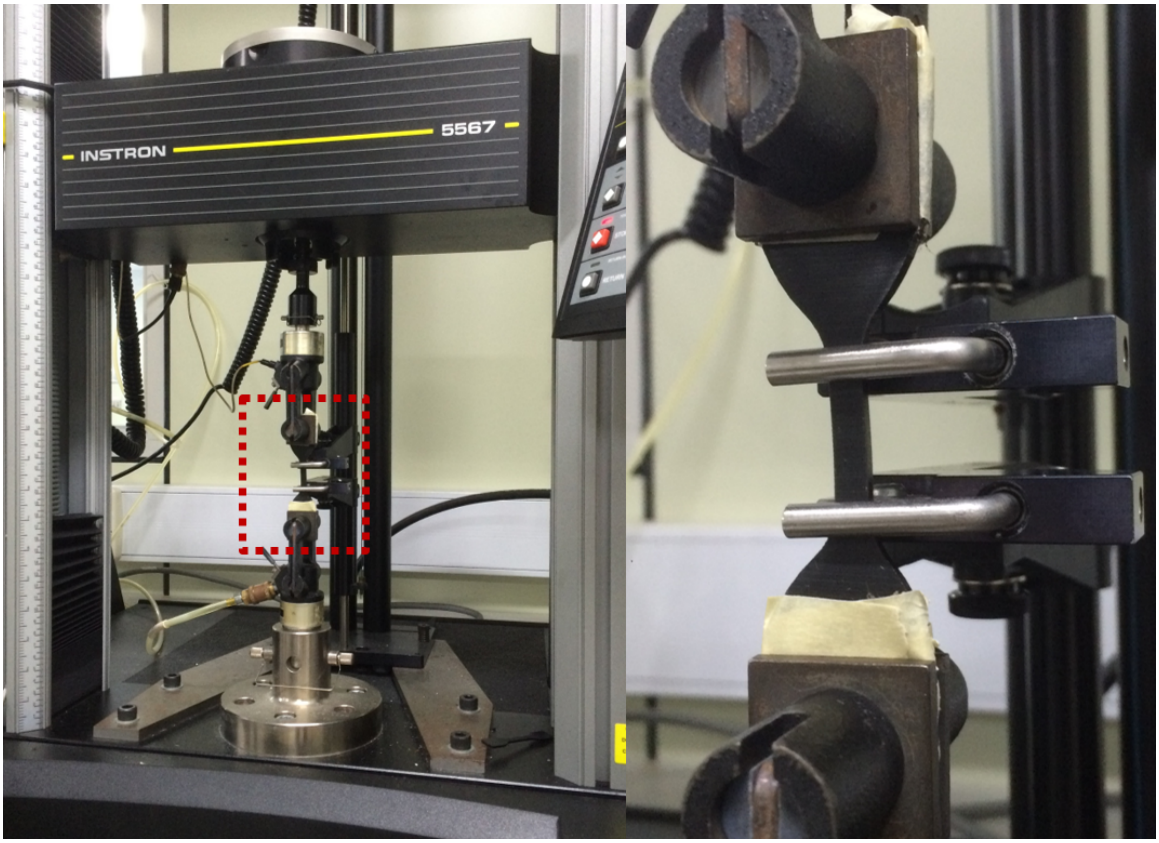

Figure 2.4. Test setup

2.4 Results and discussion

The test results are shown in Fig. 2.5, for all the DMs, tested and the base material TB+. VW+ was displayed separately in Fig. 2.6 as to not skew the range of Fig. 2.5. VW+ is the strongest of the materials tested, with a tensile strength above 30 MPa, like that of ABS. Conversely, TB+ was the most elastic material tested, with a maximum strain above 120% albeit at a much lower tensile strength (under .6 MPa). The staggering of the material properties due to the different ratios of base materials in the mixture is clearly visible, with DM40 having a low tensile strength less than 1 MPa and high elongation above 100% strain closely resembling TB+. At the opposite end of the range, DM95 exhibited a much higher tensile strength above 5.75 MPa more akin to the characteristics of VW+. The tensile strength of DM95 is still only a fraction of the tensile strength of VW+, showing that the DM range is skewed closer to the properties of TB+. Table 2.2 summarizes the results of the tensile test.

Table 2.2. Maximum stress and strain values for the tested materials

	Strain (%)	Stress (MPa)
Tango Black+	126%	0.58
DM40	110%	0.89
DM50	103%	1.03
DM60	85%	1.56
DM70	77%	2.16
DM85	74%	3.13
DM95	68%	5.91
Vero White+	30%	33

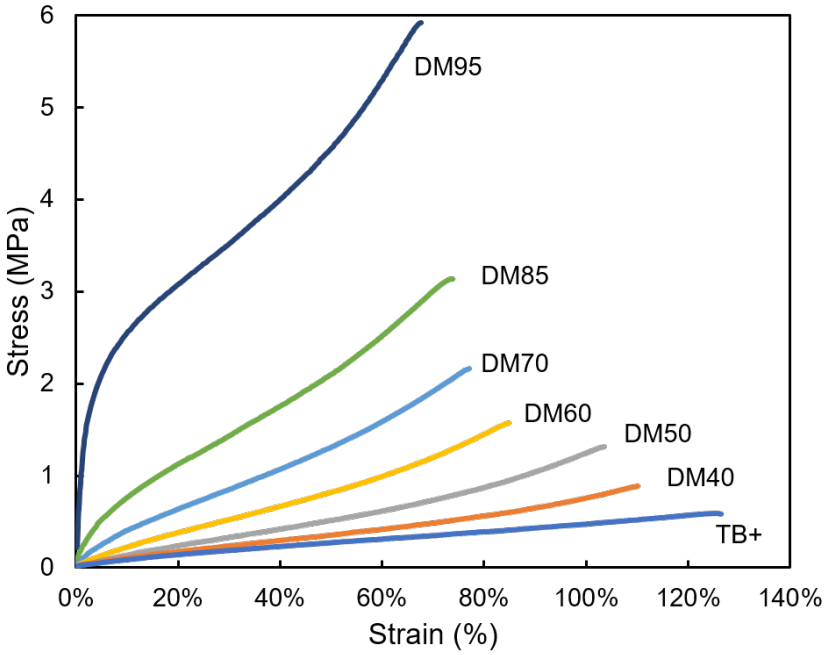

Figure 2.5. Stress-strain curve for DMs and TB+

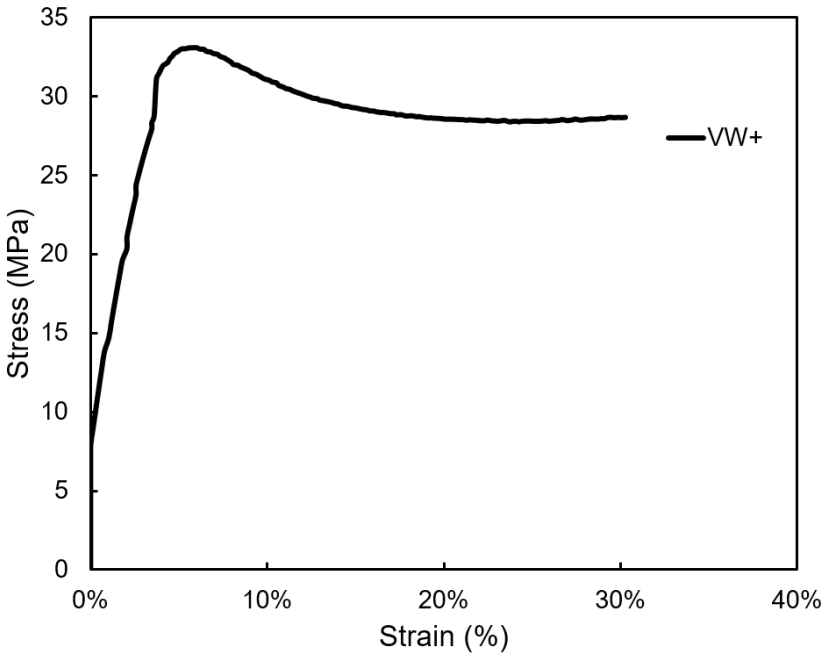

Figure 2.6. Stress-strain curve for VW+

Microstructure analysis of the fracture surface was conducted with a Scanning Electron Microscope (SEM). Images were taken at 60x, 100x, 200x, 500x, and 1,000x magnification clearly shows the difference between the two base materials. TB+ shows a smooth surface with horizontal lines caused by the layer deposition process. These lines correspond to the individual layers. VW+ displays a very different fracture surface, with several cracks corresponding to a more brittle fracture when compared to TB+. The horizontal stripping caused by the printing process is still visible, although not as clearly as in the TB+ samples. Fig. 2.7 shows SEM images at 100x magnification for TB+ and VW+.

The DMs display a varying amount of roughness on their surface, caused by the different ratios of VW+ present in the mixture. For example, DM40 shares most of the surface characteristics of TB+ with an almost perfectly smooth fracture. However, as the ratio of VW+ in the DM mixture increases the surface becomes rougher as seen in DM85 and DM95. This further proves that the DM range shares more similarities in their composition with TB+ than with VW+. Fig. 2.8 shows SEM images at 100x magnification for DMs.

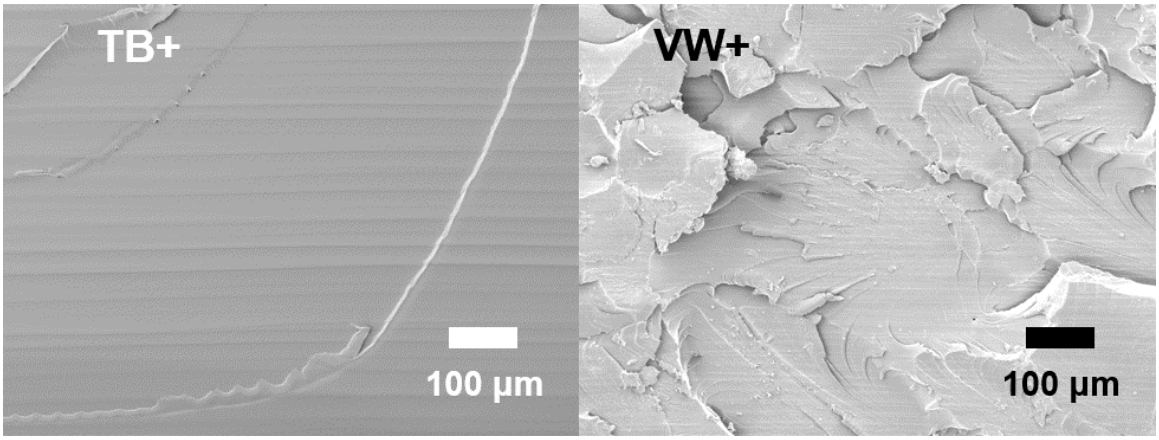

Figure 2.7. SEM at 100x magnification for VW+ and TB+

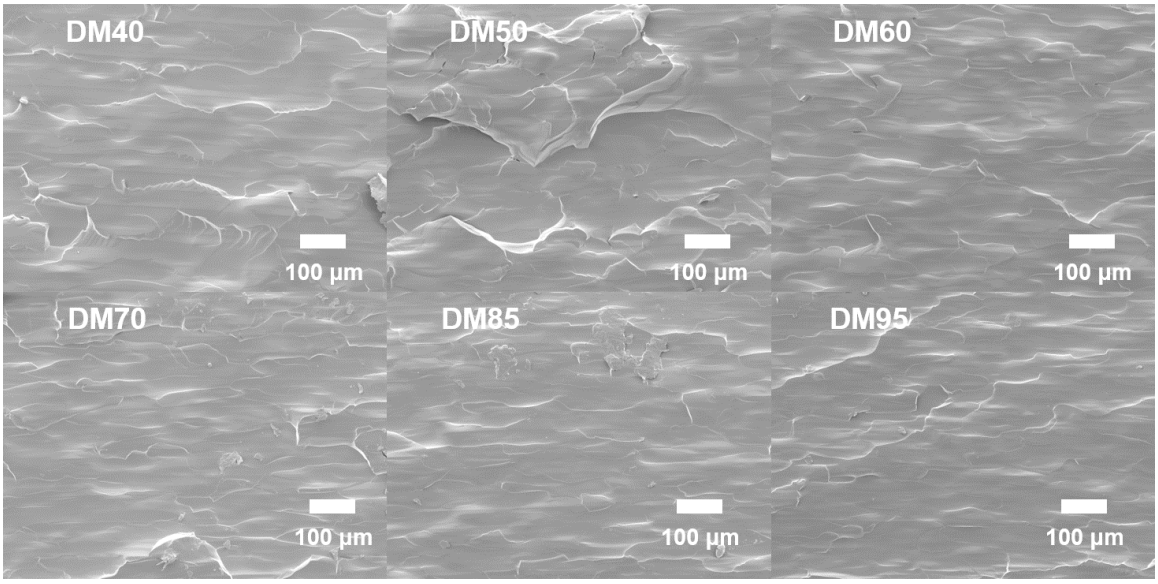

Figure 2.8. SEM at a 100x magnification of DMs

2.5 Summary

The work presented in this section summarizes the testing of parts printed using MJ AM. The baseline materials TB+ and VW+, as well as 6 different DMs, were subjected to a uniaxial tension test to record their strain-stress characteristics. The resulting data will be used in the next section to conduct curve fittings into four different hyperelastic material models. Additionally, SEM analysis provided insight into the effects of base material mixing on the fracture characteristics of the DMs.

3. MATERIAL MODEL FITTING

3.1 Nonlinear Material Models

The relationship between stress and strain for any given material is unique and provides information on the mechanical properties of the material. This relationship can be plotted by analyzing the deformation (strain) experienced at a given loading (stress) condition. On linear materials, the stress-strain curve can be described by its slope, also known as its elastic modulus. However, for nonlinear hyperelastic materials this relationship is not easily described by a single slope, and therefore a more complex equation is required to fully express the behavior of the material under load. Hyperelasticity provides a way for modeling the stress-strain relationship of materials that do not conform to conventional linear elastic models. Melvin Mooney [49] and Ronald Rivlin [50, 51], Mooney-Rivlin and Neo-Hookean models.

3.2 Explanation of Models

The focus of this study is in the polynomial hyperelastic model, also called the generalized Rivlin model [52]. This material model expresses the strain energy density function as a linear combination of strain invariants of the left Cauchy-Green deformation tensor and constants. Special cases of the polynomial model can yield both mechanistic and phenomenological models. Depending on the value of N different models can be derived from this general formula, different values are shown table 3.1.

$$W = \sum_{i+j=1}^{N} c_{ij}(\overline{I_1} - 3)^i(\overline{I_2} - 3)^j + \sum_{m=1}^{M} D_m(J-1)^{2m} \tag{3.1}$$

The strain invariants I can also be expressed in terms of the three principal stretches λ_1, λ_2, and λ_3 as shown in equations (3.2),(3.3), and (3.4). Meanwhile

Table 3.1. Values used for the different forms of the polynomial model

	N	c01	c10	c11	c20	c02
Neo-Hookean	1	0	Fitted	-	-	-
Mooney Rivlin 2	1	Fitted	Fitted	-	-	-
Mooney Rivlin 3	2	Fitted	Fitted	Fitted	0	0
Mooney Rivlin 5	2	Fitted	Fitted	Fitted	Fitted	Fitted

the stretch is related to the final length l_i and the initial length L_i according to equation (3.5).

$$I_1 = \lambda_1^2 + \lambda_2^2 + \lambda_3^2 \tag{3.2}$$

$$I_2 = \lambda_1^2\lambda_2^2 + \lambda_2^2\lambda_3^2 + \lambda_3^2\lambda_1^2 \tag{3.3}$$

$$I_3 = \lambda_1^2\lambda_2^2\lambda_3^2 = J^2 \tag{3.4}$$

$$\lambda_i = \frac{l_i}{L_i} \tag{3.5}$$

For incompressible materials, the third strain invariant yields.

$$I_3 = \lambda_1^2\lambda_2^2\lambda_3^2 = 1 \tag{3.6}$$

$$J = \sqrt{I_3} = \lambda_1\lambda_2\lambda_3 = 1 \tag{3.7}$$

Which in turn makes the second part of the equation negligible.

$$W = \sum_{i+j=1}^{N} c_{ij}(\overline{I_1} - 3)^i(\overline{I_2} - 3)^j \tag{3.8}$$

In the case of simple tension, two of the three principal stretches are equal when dealing with incompressible materials. The stretch along the axis of tension λ_1 can be expressed as λ.

$$\lambda_1 = \lambda \tag{3.9}$$

$$\lambda_2 = \lambda_3 \tag{3.10}$$

Taking this into account and utilizing equation (3.6) the stretches can be expressed in terms of a single stretch parallel to the axis of tension.

$$\lambda_2 = \lambda_3 = \frac{1}{\sqrt{\lambda}} \tag{3.11}$$

Utilizing these new expressions for the stretches the equations for the invariants can be rewritten.

$$I_1 = \lambda^2 + \frac{2}{\lambda} \tag{3.12}$$

$$I_2 = 2\lambda + \frac{1}{\lambda^2} \tag{3.13}$$

The relationship between engineering stress and stretch for incompressible materials under tension was published by Rivlin and is used to derive the equations for the given material models in terms of stress. This is necessary as the data acquired from the UTM is expressed in terms of engineering stress.

$$\sigma_{eng} = 2(\lambda - \frac{1}{\lambda^2})(\frac{\delta W}{\delta I_1} + \frac{1}{\lambda}\frac{\delta W}{\delta I_2}) \tag{3.14}$$

Where:

σ_{eng}: Engineering stress

W: Strain energy

λ: Stretch parallel to σ_{eng}

I_1,I_2: Strain invariants

3.2.1 Neo-Hookean

The Neo-Hookean hyperelastic material model used for predicting non-linear stress-strain responses for elastic materials. The curve of the NH model is initially linear but tapers off at a given point, this useful when modeling polymers. Plastics and rubbers will initially stretch as the polymer chains move relative to each other until they have reached the maximum point which the covalent bonds will allow, at this point, the elastic modulus will increase rapidly. A drawback of this model is its inability to model the increase in modulus at higher strains which makes it inadequate for modeling materials beyond 20% [53]. This model is suitable for approximations when data is insufficient.

The NH model can be derived from the polynomial hyperelastic model by utilizing the constants shown in table 3.1.

$$W = \frac{\mu}{2}(\overline{I_1} - 3) \tag{3.15}$$

The only parameter in the NH model is expressed in terms of the shear modulus.

$$c_{10} = \frac{\mu}{2} \tag{3.16}$$

3.2.2 Mooney Rivlin

The Mooney-Rivlin 2-parameter model is a widely used phenomenological material model, however, it is only one of the several cases derived from the generalized Rivlin hyperelastic material model. Other widely used versions of the model are the 3-parameter, the 5-parameter, and the 9-parameter Mooney Rivlin models. This can be obtained by utilizing the constants summarized in table 3.1. All MR models are based on the strain energy density function expressed in terms of a linear combination of the two invariants of the left Cauchy-Green deformation tensor. Depending on the required shape of the curve different number of parameters can be used, a higher number of parameters tend to offer a closer fit [54]. However, a higher number of

parameters tend to make computational simulations very computationally demanding. In this study 3 different cases of the MR model were used, the 2-parameter, 3-parameter, and 5-parameter models, their strain energy density formulas are these:

$$W = c_{10}(\overline{I_1} - 3) + c_{01}(\overline{I_2} - 3) \tag{3.17}$$

$$W = c_{10}(\overline{I_1} - 3) + c_{01}(\overline{I_2} - 3) + c_{11}(\overline{I_1} - 3)(\overline{I_2} - 3) \tag{3.18}$$

$$W = c_{10}(\overline{I_1} - 3) + c_{01}(\overline{I_2} - 3) + c_{20}(\overline{I_1} - 3)^2 + c_{11}(\overline{I_1} - 3)(\overline{I_2} - 3) + c_{02}(\overline{I_2} - 3)^2 \tag{3.19}$$

3.3 Model Derivation

3.3.1 Neo-Hookean

Starting from the strain energy density function and utilizing the relationship between engineering stress the derivation for a more usable function was conducted.

$$W = \frac{\mu}{2}(\overline{I_1} - 3) \tag{3.20}$$

Recalling the relationship between strain energy density function and engineering stress in in equation (3.14) we take the partial derivatives with respect to the 2 invariants we get:

$$\frac{\delta W}{\delta I_1} = \frac{\mu}{2} \tag{3.21}$$

$$\frac{\delta W}{\delta I_2} = 0 \tag{3.22}$$

Utilizing these values in the equation for engineering stress (3.14) we get:

$$\sigma_{eng} = 2(\lambda - \frac{1}{\lambda^2})(\frac{\mu}{2} + \frac{1}{\lambda}(0)) \tag{3.23}$$

After simplifying the resulting equation is now in terms of engineering stress and stretches, making it more suitable for fitting procedures utilizing data from a UTM.

$$\sigma_{eng} = 2(\lambda - \frac{1}{\lambda^2})(\frac{\mu}{2}) \tag{3.24}$$

3.3.2 Mooney Rivlin 2 parameters

Starting from the strain energy density function and utilizing the relationship between engineering stress the derivation for a more usable function was conducted.

$$W = c_{10}(\overline{I_1} - 3) + c_{01}(\overline{I_1} - 3) \tag{3.25}$$

Recalling the relationship between strain energy density function and engineering stress in in equation (3.14) we take the partial derivatives with respect to the 2 invariants we get:

$$\frac{\delta W}{\delta I_1} = c_{10} \tag{3.26}$$

$$\frac{\delta W}{\delta I_2} = c_{01} \tag{3.27}$$

Substituting these values into the equation (3.14) now in terms of engineering stress and stretches, making it more suitable for fitting procedures utilizing data from a UTM.

$$\sigma_{eng} = 2(\lambda - \frac{1}{\lambda^2})(c_{10} + \frac{1}{\lambda}c_{01}) \tag{3.28}$$

3.3.3 Mooney Rivlin 3 parameters

Similarly to the previous derivation we utilize the strain energy formula for MR3 and conduct the partial derivatives in respect to strain energy.

$$W = c_{10}(\overline{I_1} - 3) + c_{01}(\overline{I_2} - 3) + c_{11}(\overline{I_1} - 3)(\overline{I_2} - 3) \tag{3.29}$$

The results from the partial derivatives give:

$$\frac{\delta W}{\delta I_1} = c_{10} + c_{11}\overline{I_2} - 3c_{11} \tag{3.30}$$

$$\frac{\delta W}{\delta I_2} = c_{10} + c_{11}\overline{I_1} - 3c_{11} \tag{3.31}$$

Utilizing these values in equation (3.14):

$$\sigma_{eng} = 2(\lambda - \frac{1}{\lambda^2})(c_{10} + c_{11}\overline{I_2} - 3c_{11} + \frac{1}{\lambda}(c_{10} + c_{11}\overline{I_1} - 3c_{11})) \tag{3.32}$$

Rearranging the formula:

$$\sigma_{eng} = 2(\lambda - \frac{1}{\lambda^2})(c_{10} + c_{11}\overline{I_2} - 3c_{11} + \frac{1}{\lambda}c_{10} + \frac{1}{\lambda}c_{11}\overline{I_1} - \frac{1}{\lambda}3c_{11}) \tag{3.33}$$

Grouping the constants together:

$$\sigma_{eng} = 2(\lambda - \frac{1}{\lambda^2})(c_{10} + \frac{1}{\lambda}c_{10} + c_{11}(\overline{I_2} - 3 + \frac{\overline{I_1}}{\lambda} - \frac{3}{\lambda})) \tag{3.34}$$

Utilizing equations (3.12) and (3.13) and substituting in the equation above:

$$\sigma_{eng} = 2(\lambda - \frac{1}{\lambda^2})(c_{10} + \frac{1}{\lambda}c_{10} + c_{11}((2\lambda + \frac{1}{\lambda^2}) - 3 + \frac{(\lambda^2 + \frac{2}{\lambda})}{\lambda} - \frac{3}{\lambda})) \tag{3.35}$$

$$\sigma_{eng} = 2(\lambda - \frac{1}{\lambda^2})(c_{10} + \frac{1}{\lambda}c_{10} + c_{11}(3\lambda + \frac{3}{\lambda^2} - 3 + \frac{3}{\lambda})) \tag{3.36}$$

By simplifying the equation above the MR3 model can be expressed in terms applicable to the data gathered by the UTM.

$$\sigma_{eng} = 2(\lambda - \frac{1}{\lambda^2})(c_{10} + \frac{1}{\lambda}c_{10} + 3c_{11}(\lambda - 1 + \frac{1}{\lambda} + \frac{1}{\lambda^2})) \tag{3.37}$$

3.3.4 Mooney Rivlin 5 parameters

Utilizing the MR5 strain energy equation below we will derive an equation in terms of engineering stress and stretches similarly to the process done for the other models.

$$W = c_{10}(\overline{I_1} - 3) + c_{01}(\overline{I_2} - 3) + c_{20}(\overline{I_1} - 3)^2 + c_{11}(\overline{I_1} - 3)(\overline{I_2} - 3) + c_{02}(\overline{I_2} - 3)^2 \quad (3.38)$$

Recalling the equation (3.14) we take the partial derivatives of the equation above in respect to the two strain invariants resulting in the two equations below:

$$\frac{\delta W}{\delta I_1} = c_{10} + 2c_{20}\overline{I_1} - 6c_{20} + c_{11}\overline{I_2} - 3c_{11} \quad (3.39)$$

$$\frac{\delta W}{\delta I_2} = c_{10} + 2c_{02}\overline{I_2} - 6c_{02} + c_{11}\overline{I_1} - 3c_{11} \quad (3.40)$$

Substituting these values into equation (3.14) we get:

$$\sigma_{eng} = 2(\lambda - \frac{1}{\lambda^2})((c_{10} + 2c_{20}\overline{I_1} - 6c_{20} + c_{11}\overline{I_2} - 3c_{11}) + \frac{1}{\lambda}(c_{10} + 2c_{02}\overline{I_2} - 6c_{02} + c_{11}\overline{I_1} - 3c_{11})) \quad (3.41)$$

Rearranging the terms and grouping by constants:

$$\sigma_{eng} = 2(\lambda - \frac{1}{\lambda^2})(c_{10} + 2c_{20}\overline{I_1} - 6c_{20} + c_{11}\overline{I_2} - 3c_{11} + \frac{1}{\lambda}c_{10} + \frac{2\overline{I_2}}{\lambda}c_{02} - \frac{6}{\lambda}c_{02} + \frac{\overline{I_1}}{\lambda}c_{11} - \frac{3}{\lambda}c_{11}) \quad (3.42)$$

$$\sigma_{eng} = 2(\lambda - \frac{1}{\lambda^2})(c_{10} + \frac{1}{\lambda}c_{10} + 2c_{20}(\overline{I_1} - 3) + \frac{2}{\lambda}c_{02}(\overline{I_2} - 3) + c_{11}(\overline{I_2} - 3 + \frac{\overline{I_1}}{\lambda} - \frac{3}{\lambda})) \quad (3.43)$$

Utilizing equations (3.12) and (3.13) and substituting in the equation above:

$$\begin{aligned}\sigma_{eng} = 2(\lambda - \frac{1}{\lambda^2})(c_{10} + \frac{1}{\lambda}c_{10} + 2c_{20}((\lambda^2 + \frac{2}{\lambda}) - 3) + \frac{2}{\lambda}c_{02}((2\lambda + \frac{1}{\lambda^2}) - 3) + \\ c_{11}((2\lambda + \frac{1}{\lambda^2}) - 3 + \frac{(\lambda^2 + \frac{2}{\lambda})}{\lambda} - \frac{3}{\lambda}))\end{aligned} \quad (3.44)$$

Simplifying and rearranging the equation makes it possible to relate the MR5 model to the data gathered from the tensile test which is terms of engineering stress and stretches.

$$\sigma_{eng} = 2(\lambda - \frac{1}{\lambda^2})(c_{10} + \frac{1}{\lambda}c_{10} + 2c_{20}(\lambda^2 + \frac{2}{\lambda} - 3) + \frac{2}{\lambda}c_{02}(2\lambda + \frac{1}{\lambda^2} - 3) + 3c_{11}(\lambda - 1 - \frac{1}{\lambda} + \frac{1}{\lambda^2})) \tag{3.45}$$

3.4 Model Fitting Results

Utilizing the included capabilities of ANSYS Workbench a regression analysis utilizing the least squares method was conducted to fit the test data into the four different models. The resulting parameters for the material models are summarized in tables 3.2-3.5 below. Additionally the Least Squares Error (L.S.E) associated to each fitting procedure is tabulated along with the constants.

Table 3.2. Model constants for Neo-Hookean

MPa	TB+	DM40	DM50	DM60	DM70	DM85	DM95
μ	0.27381	0.37261	0.52596	0.81594	1.3132	2.1689	4.9548
L.S.E.	15.76	19.36	14.86	10.96	11.92	18.84	48.62

Table 3.3. Model constants for Mooney Rivlin 2

MPa	TB+	DM40	DM50	DM60	DM70	DM85	DM95
C10	0.11038	0.19407	0.34978	0.43052	0.47794	0.32347	-2.1776
C01	0.04228	-0.01166	-0.12353	-0.03125	0.24418	1.0545	6.5737
L.S.E.	14	19.25	12.24	10.87	10.95	13.71	26.08

Table 3.4. Model constants for Mooney Rivlin 3

MPa	TB+	DM40	DM50	DM60	DM70	DM85	DM95
C10	-0.111	-0.29731	-0.28273	-0.69712	-1.74054	-4.286	-22.23456
C01	0.30504	0.56013	0.59844	1.24088	2.74176	6.275	29.55866
C11	0.0419	0.10601	0.14925	0.30099	0.61966	1.2761	5.46962
L.S.E.	7.98	7.82	2.84	4.05	3.53	4.9	10.95

Table 3.5. Model constants for Mooney Rivlin 5

MPa	TB+	DM40	DM50	DM60	DM70	DM85	DM95
C10	-1.06969	-1.98857	-1.2888	-3.90061	-8.33538	-20.37675	-124.26453
C01	1.33218	2.35641	1.65428	4.60156	9.66096	23.21059	137.45785
C20	0.31292	1.00274	0.98533	4.04227	8.89633	20.55581	132.37894
C11	-1.22364	-3.58483	-3.26595	-13.12383	-28.585	-66.33612	-424.3725
C02	1.63091	4.06546	3.3841	12.56673	26.93327	62.78131	394.82863
L.S.E.	5.28	4.9	2.25	2.7	1.74	2.11	3.08

As part of the fitting procedure, ANSYS calculates the value for the residual error associated with each material. These values were plotted in Fig. 3.1, and give an initial comparison of the accuracy of the models. Material models with more constants (NH has one, MR2 has 3 and MR 5 has 5) also have more inflection points in their stress-strain curve. The NH model displays a single curvature (Fig. 3.7) while the MR5 models show multiple curvatures (Fig. 3.10). This is of importance with the most rigid materials as they see a higher stiffening effect at larger elongations, which is observable in the stress-strain curves of DM70, DM85 and DM95 at strains higher than 50 %. Therefore, the models with the higher number of constants display a lower residual error, as they can fit the curves better at higher elongations.

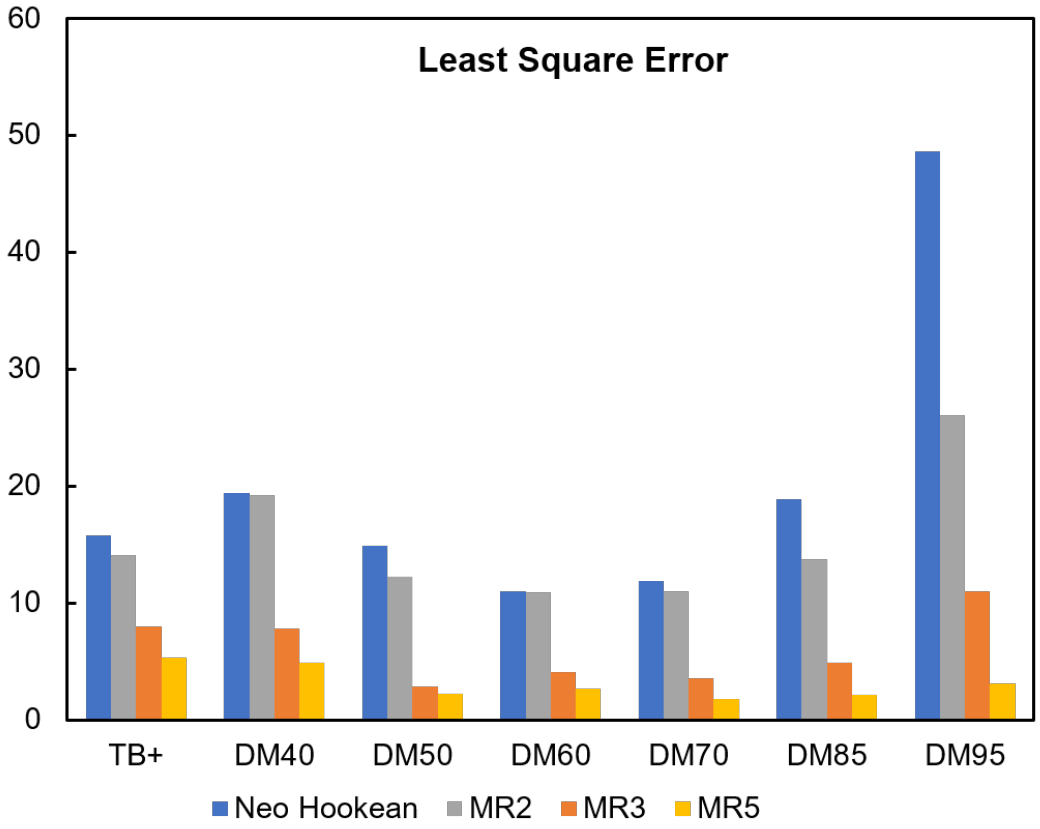

Figure 3.1. Least Square Error associated with the ANSYS fitting

3.4.1 Neo-Hookean

As shown in Fig. 3.1 the residual error of the NH model for DM95 is the highest among the other materials. The curve in Fig. 3.7 shows that NH does not accurately represent DM95, conversely, the NH models for the TB+ fits accurately up to its full elongation. The NH models for DM40 and DM50 fits well up to 80% strain. While the models for DM60, DM70 and DM85 are accurate up to 60% strain.

The NH does not account for any strain stiffening effects, therefore at higher elongation, the model under-predicts the actual stress values for materials like DM60, DM70, and DM85. The NH model is suitable for all DMs except DM95 when a mechanistic model is desired and simulated strains will be less than 20%.

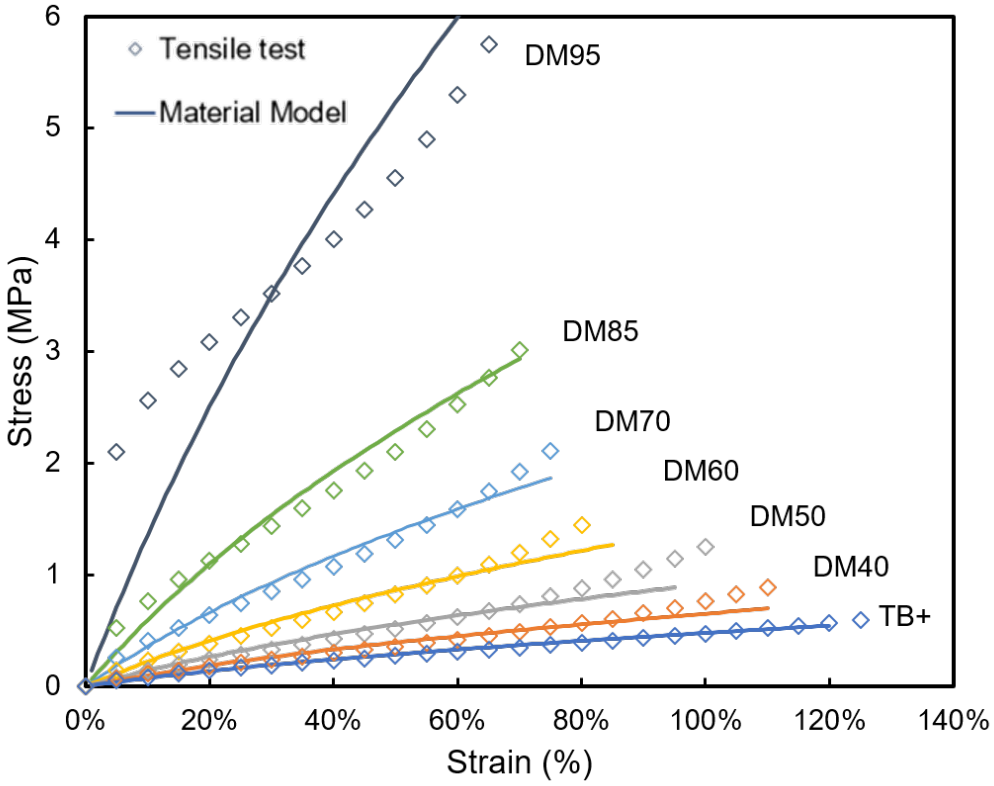

Figure 3.2. Stress-strain curves generated from the fitting procedure of the NH model

3.4.2 Mooney Rivlin 2 parameters

The MR2 model (Fig. 3.8) lacks the ability to model the stiffening effects observed in the DMs at higher elongations. However, its still suitable for modeling all the materials for longer strains than the NH model. Additionally, the curve for DM95 has a steeper initial slope that fits the material suitably at strains lower than 25%. As seen in Fig. 3.1 the residual error is substantially lower for DM95 and overall lower for all other materials. This is one of the most widely used models and is available in most FEA packages as standard making it a suitable option for preliminary simulations. The MR2 model is a good option when a phenomenological model is acceptable and computational power is limited.

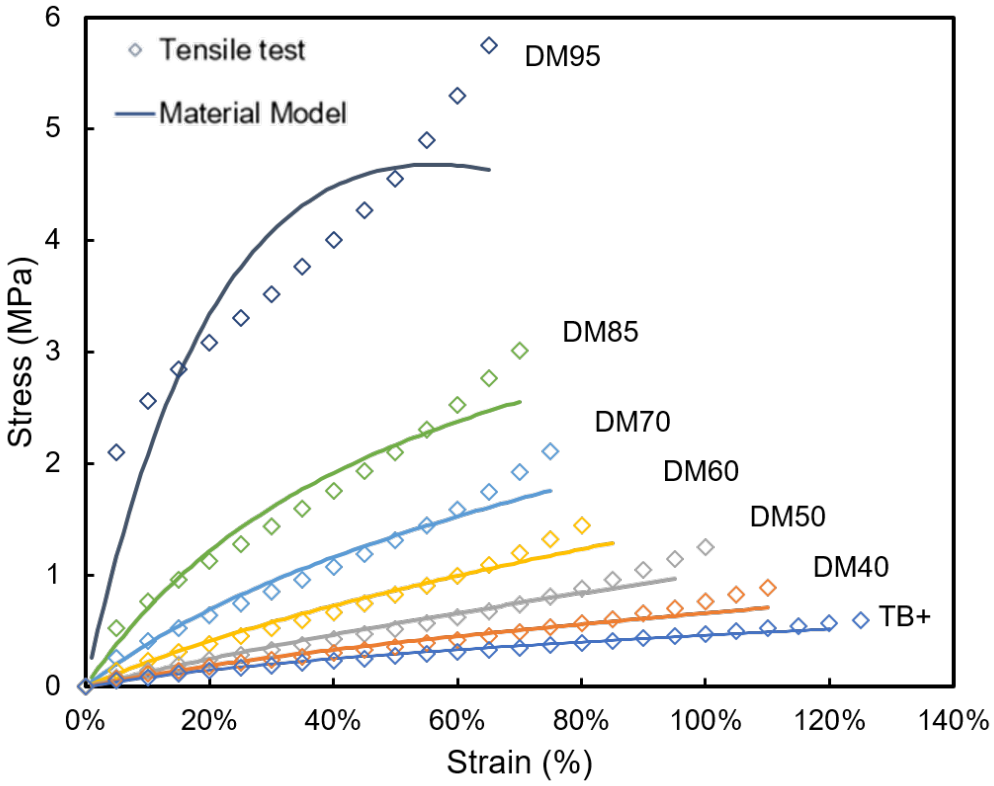

Figure 3.3. Stress-strain curves generated from the fitting procedure of the MR2 model

3.4.3 Mooney Rivlin 3 parameters

The MR3 models accurately fit all the materials as seen in Fig. 3.9, moreover as seen from Fig. 3.1 the residual error for this model is markedly smaller than that of the MR2 and NH models. However, this comes at the expense of much higher computational demands during numerical simulations and adds the risk that the simulate might not converge on a result. This model is particularly suited for modeling the two strongest DMs, DM95 and DM85 at higher strains. When there are no computation limits, or the simulations require strains beyond 30% this the best fitting model.

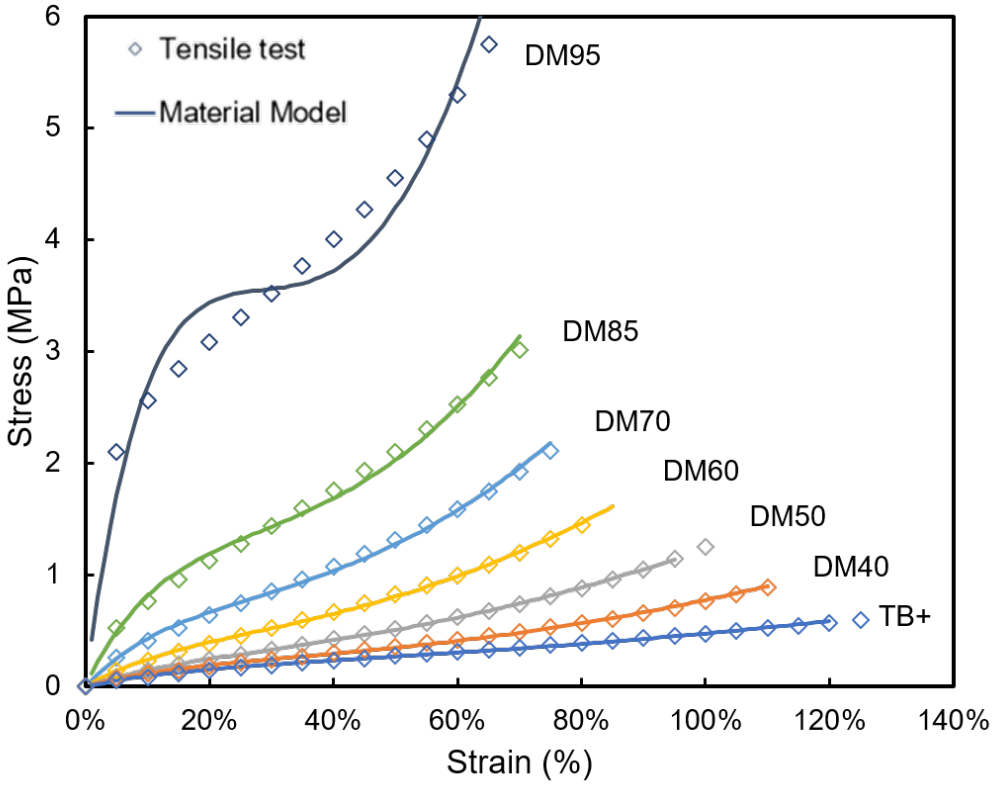

Figure 3.4. Stress-strain curves generated from the fitting procedure of the MR3 model

3.4.4 Mooney Rivlin 5 parameters

As per Fig. 3.1 the MR5 model has the smallest residual error, and the stress-strain curves accurately fit all the materials (Fig. 3.10). However, the higher computational demands suffer from diminishing returns, as they are not markedly better than the results from the MR3 model. Similarly, to the MR3model, the MR5 is suited for modeling the two strongest DMs, DM95 and DM85 at their full elongation.

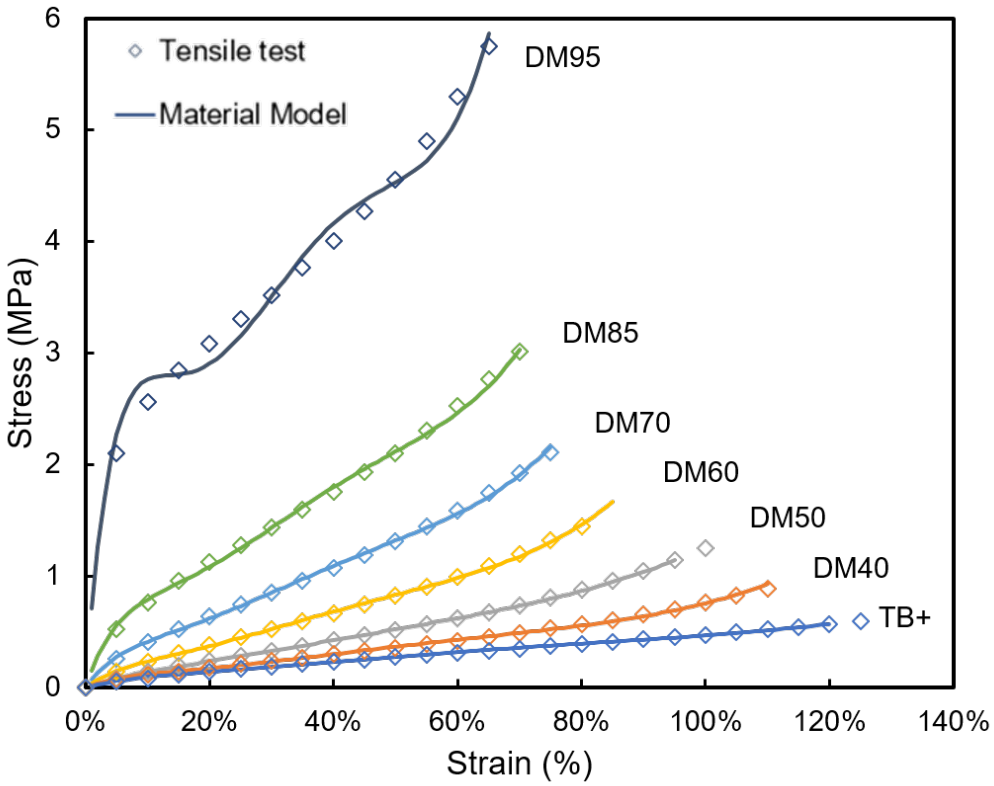

Figure 3.5. Stress-strain curves generated from the fitting procedure of the MR5 model

3.5 Results for Model fitting at 30% strain

Similarly to the previous fitting procedure ANSYS Workbench was utilized for the regression analysis. The material were fitted utilizing the tensile test data up to 30% strain. The resulting parameters for the material models are summarized in tables 3.6-3.9 below. The Least Squares Error (L.S.E) associated with the regression analysis are tabulated along with the model constants.

Table 3.6. Model constants for Neo-Hookean fitted up to 30% strain

MPa	TB+	DM40	DM50	DM60	DM70	DM85	DM95
μ	0.30622	0.38572	0.50473	0.81634	1.37520	2.43680	6.66260
L.S.E	11.89	12.91	4.96	7.54	9.51	14.47	32.02

Table 3.7. Model constants for Mooney Rivlin 2 fitted up to 30% strain

MPa	TB+	DM40	DM50	DM60	DM70	DM85	DM95
C10	-0.19382	-0.27101	-0.08034	-0.30090	-0.93179	-2.69040	-15.56600
C01	0.40728	0.54493	0.38725	0.82836	1.90110	4.62520	22.71500
L.S.E	6.7928	7.4058	3.0348	4.3974	3.8951	5.1527	10.99

Table 3.8. Model constants for Mooney Rivlin 3 fitted up to 30% strain

MPa	TB+	DM40	DM50	DM60	DM70	DM85	DM95
C10	-1.2219	-1.812	-1.0103	-2.5392	-5.2574	-12.727	-71.695
C01	1.4985	2.1821	1.3694	3.1986	6.4872	15.308	82.934
C11	0.58549	0.87299	0.55087	1.3001	2.4847	5.5833	29.338
L.S.E	4.87	4.8071	2.3082	2.9599	2.0599	2.573	4.475

Table 3.9. Model constants for Mooney Rivlin 5 fitted up to 30% strain

MPa	TB+	DM40	DM50	DM60	DM70	DM85	DM95
C10	-8.4416	-11.047	-6.9709	-16.317	-25.268	-58.572	-341.03
C01	8.9008	11.656	7.4648	17.308	26.983	62.34	360.19
C20	117	141.48	112.26	235.36	323.49	670.91	3235.1
C11	-298.54	-362.21	-284.29	-599.17	-826.18	-1722.3	-8393.2
C02	196.57	239.75	185.27	393.38	545.59	1146	5670.8
L.S.E	2.6399	2.5074	1.528	1.5063	0.94248	1.1185	0.78242

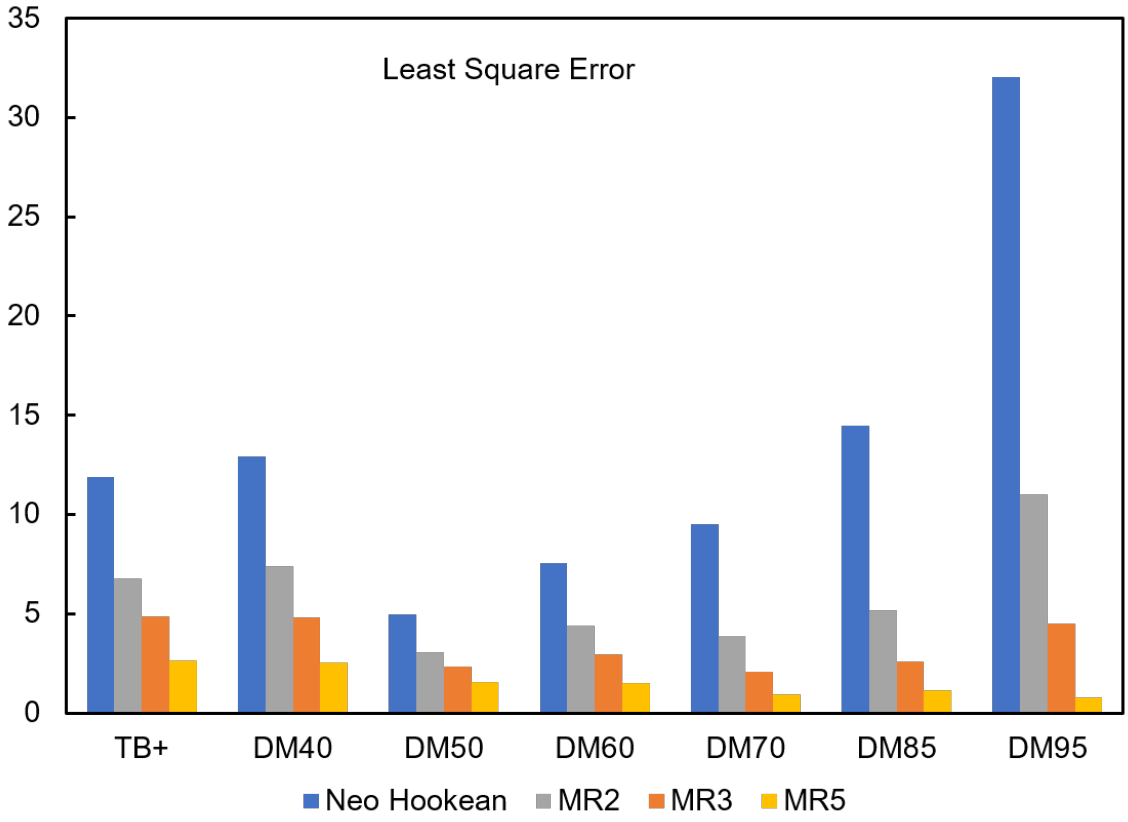

Figure 3.6. Least Square Error associated with the ANSYS fitting up to 30% strain

3.5.1 Stress Strain curves for the 30% strain fitting

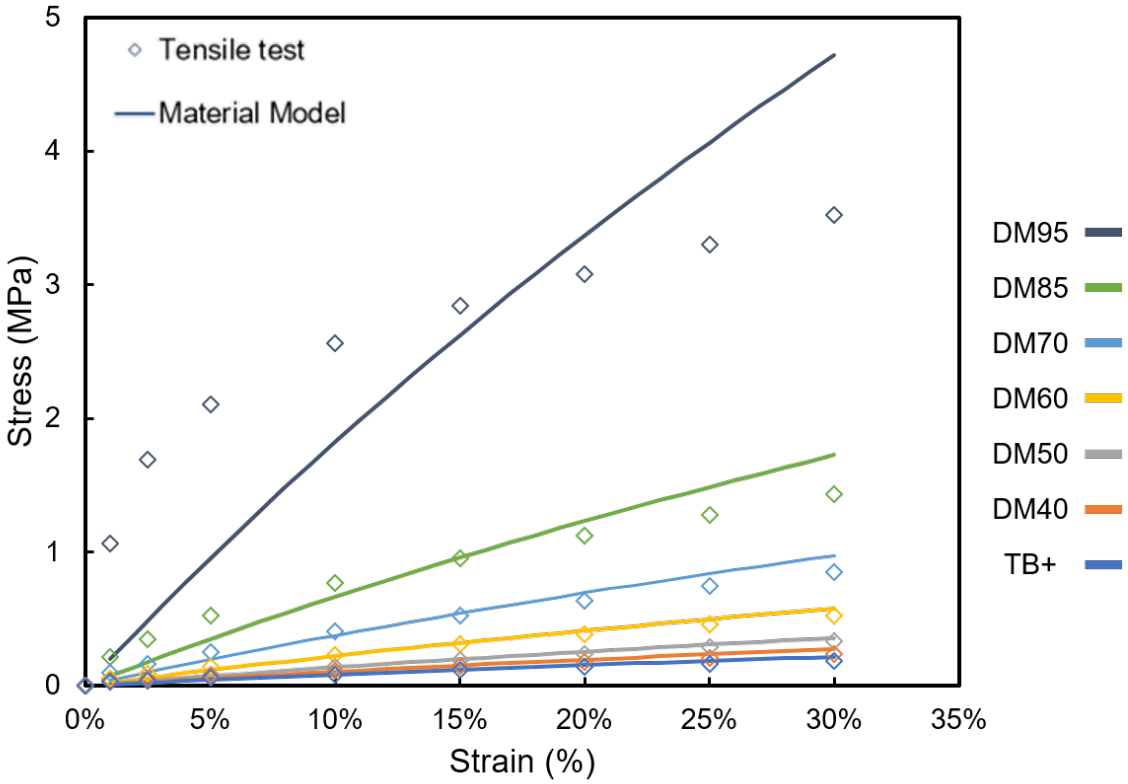

Figure 3.7. Stress-strain curves generated from the fitting procedure of the NH model up to 30% strain

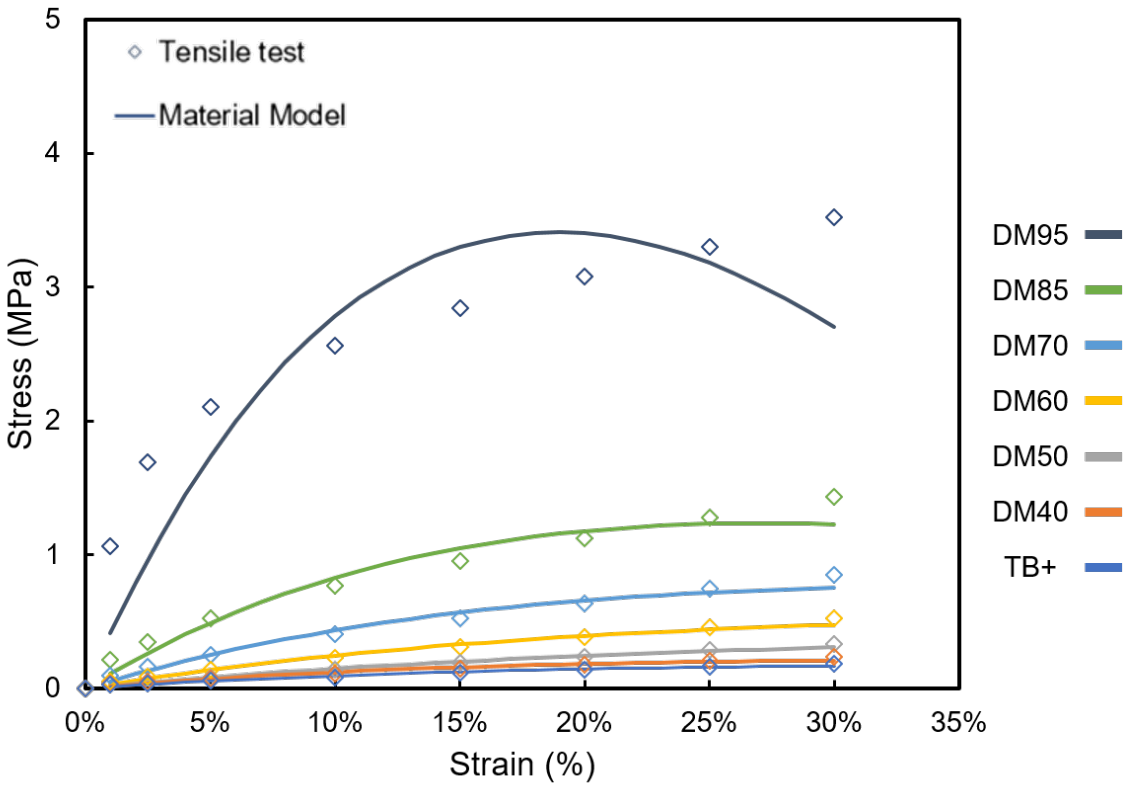

Figure 3.8. Stress-strain curves generated from the fitting procedure of the MR2 model up to 30% strain

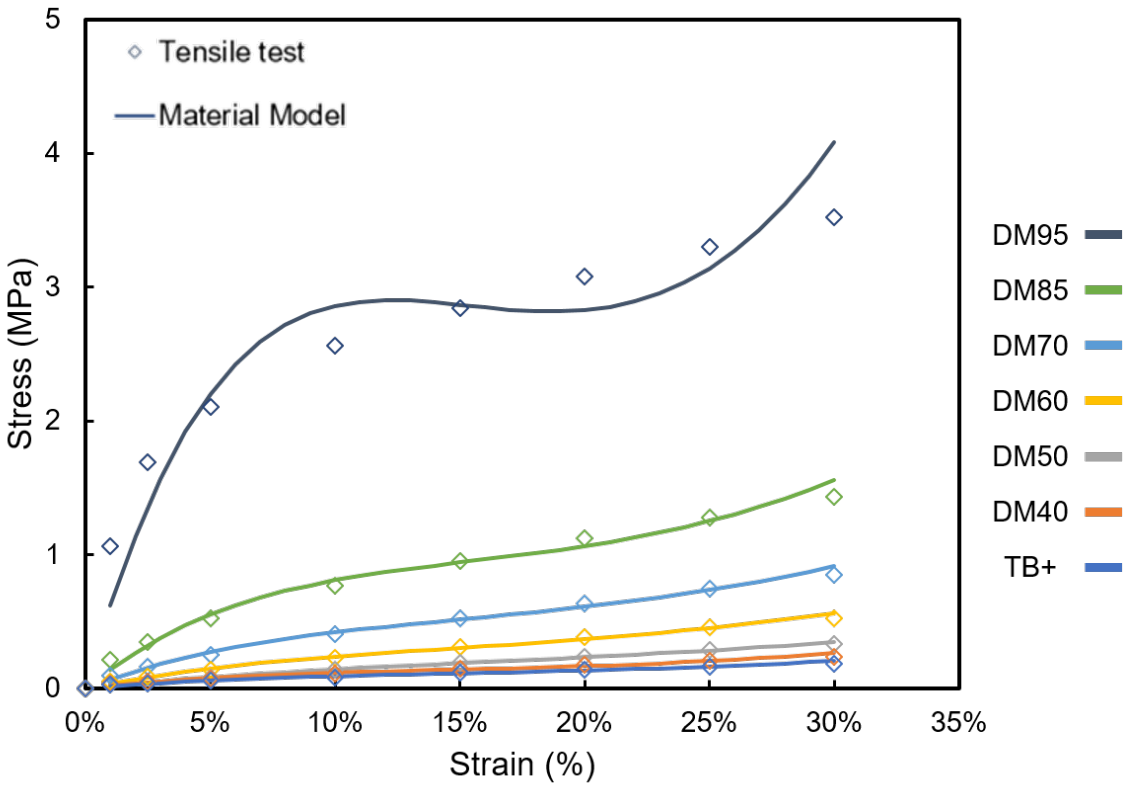

Figure 3.9. Stress-strain curves generated from the fitting procedure of the MR3 model up to 30% strain

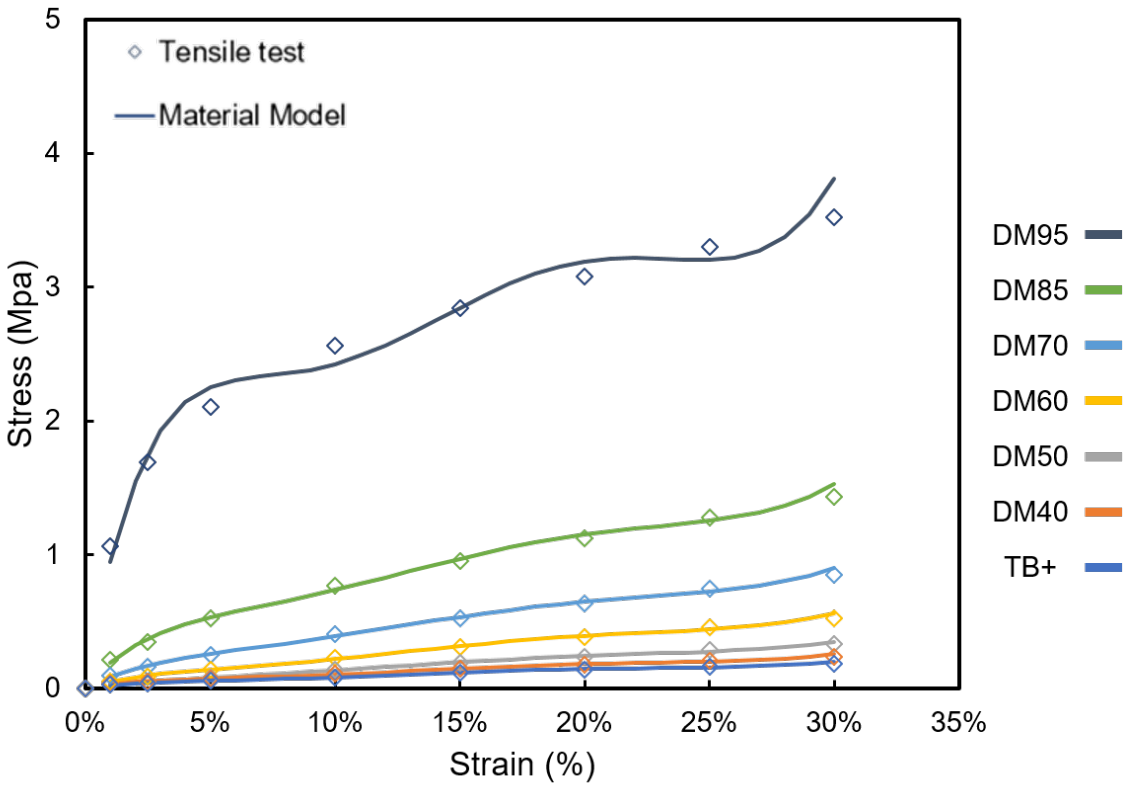

Figure 3.10. Stress-strain curves generated from the fitting procedure of the MR5 model up to 30% strain

3.6 Shore A Hardness model simplification

Hardness testing of elastic materials tends to be a very easy and simple way of characterizing a material and can provide some initial insight into the behavior of a material during loading. While strain vs stress characterization provides the required information to fully model a material it is much more complex and sometimes not a viable option. Therefore, for initial applications, empirical formulas are sometimes used to calculate the modulus of elasticity from given hardness values. Knowing the hardness of a material makes it possible to come with an initial modulus of elasticity that can be used for preliminary simulations at small strains.

These approximations tend to yield better information than the secant modulus values that are commonly reported on manufacturers data sheets. These values tend to be good approximations for elongations lower than 20%, which the same point at which the NH model starts becoming unreliable. In the case of DMs, the approximations can provide a starting point for users trying to select a given material for their desired application. Furthermore, if Stratasys releases new materials, or allows for more tunability of the material mixtures, the hardness formulas can provide information on the probable material characteristics of the new DMs without having to conduct extensive testing.

In this study, three formulas (Eqs. (3.46) to (3.48)) were utilized and compared, following similar studies conducted by Dow Corning [55] and other researchers [56]. Gent initially postulated a formula (Eq. (3.46)) that relates the Shore A hardness to Youngs modulus [57], this formula tends to work best for hardness values between 40 and 80. Shortcomings from Gents formula at lower hardness values were rectified with another equation based on the error formula (Eq. (3.47)) from a British standard 903 for testing vulcanized rubber which tends to fit a wider range of hardness values [56]. Finally, another equation (Eq. (3.48)) was postulated to provide a different approach to using the hardness values [58].

These equations relate the modulus of elasticity E to the Shore A hardness S, and can be used as approximations when no other data is available.

$$E = \frac{(.0981)(56 + 7.62336 * S)}{(.137505)(254 - 2.54 * S)} \tag{3.46}$$

$$S = 100erf(\sqrt{E}(3.186 * 10^{-4})) \tag{3.47}$$

$$log_{10}E = .0235 * S - .06403 \tag{3.48}$$

The values for each of the calculated Young's modulus are displayed in table 3.10. When compared to the values of the secant modulus (Table 3.11) it is shown that the calculated moduli are not very accurate approximations. However, Gents equation provides a relatively good approximation for low strains, especially when compared to the secant modulus at 5%. A comparison between the calculated values and the secant modulus is shown in table 3.12.

Table 3.10. Shore-A hardness values calculated from the empirical formulas

Material	Shore A Hardness	Error Calc. MPa	Gent. Calc. MPa	Log E Calc. MPa
TB+	27	0.59	1.01	0.99
DM40	40	1.35	1.69	1.99
DM50	50	2.24	2.46	3.43
DM60	60	3.49	3.61	5.88
DM70	70	5.29	5.52	10.11
DM85	85	10.21	13.18	22.76
DM95	95	18.92	43.83	39.1

Table 3.11. Secant modulus of the materials tested

	1%	5%	10%	25%	50%	75%	100%	125%
TB+	2.9	1.12	0.86	0.664	0.55	0.496	0.474	0.474
DM40	3.78	1.46	1.12	0.844	0.714	0.705	0.761	-
DM50	3.09	1.62	1.41	1.148	1.032	1.075	1.25	-
DM60	5.6	2.78	2.29	1.828	1.642	1.756	-	-
DM70	9.5	5.12	4.07	2.98	2.626	2.807	-	-
DM85	21.2	10.48	7.66	5.104	4.206	-	-	-
DM95	107	42.08	25.59	13.212	9.114	-	-	-

Table 3.12. Percent difference between the calculated values and secant modulus

Eq. 3.46 Vs Secant Modulus

	1%	5%	10%	25%	50%	75%	100%	125%
TB+	65%	10%	17%	52%	83%	103%	113%	113%
DM40	55%	16%	51%	100%	137%	140%	122%	-
DM50	21%	52%	74%	114%	138%	129%	96%	-
DM60	36%	30%	57%	97%	120%	105%	-	-
DM70	42%	8%	36%	85%	110%	97%	-	-
DM85	38%	26%	72%	158%	213%	-	-	-
DM95	59%	4%	71%	232%	381%	-	-	-

Eq. 3.47 Vs Secant Modulus

	1%	5%	10%	25%	50%	75%	100%	125%
TB+	80%	48%	32%	12%	7%	18%	24%	24%
DM40	64%	7%	21%	60%	90%	92%	78%	-
DM50	27%	38%	59%	95%	117%	109%	79%	-
DM60	38%	26%	52%	91%	112%	99%	-	-
DM70	44%	3%	30%	78%	101%	89%	-	-
DM85	52%	3%	33%	100%	143%	-	-	-
DM95	82%	55%	26%	43%	108%	-	-	-

Eq. 3.48 Vs Secant Modulus

	1%	5%	10%	25%	50%	75%	100%	125%
TB+	66%	12%	15%	49%	79%	99%	108%	108%
DM40	47%	37%	78%	136%	179%	183%	162%	-
DM50	11%	111%	143%	198%	232%	219%	174%	-
DM60	5%	112%	157%	222%	258%	235%	-	-
DM70	6%	97%	148%	239%	285%	260%	-	-
DM85	7%	117%	197%	346%	441%	-	-	-
DM95	63%	7%	53%	196%	329%	-	-	-

3.7 Summary

In this section data from a uniaxial tension, the test was fitted into four different hyperelastic models based on the generalized Rivlin material model. The models used were the Neo-Hookean model, and the two-parameter, the three-parameter, and the five-parameter Mooney-Rivlin models. The baseline materials TB+ and VW+, as well as six different DMs, were fitted. The parameters for each one of the materials was summarized and the results made available for the use of conventional FEA packages.

In addition, three different empirical formulas for calculating Young's modulus from the shore A hardness were compared against the secant modulus at different strains. The results showed that for initial simulations the Gent equation (Eq. (3.46)) can give initial approximations at strains lower than 5% when other data is not available. If new DM formulations are released or future printer generations allow for more freedom when tuning the material ratios this equation would give preliminary approximations, without requiring any complex characterization.

4. VALIDATION OF MODELS

4.1 Material model validation

To validate the accuracy of the models FEA simulations were conducted utilizing the 4 different material models. The resulting data was compared was compared to the theoretical values of the material models as well as the original data from the tensile test. The simulations were conducted in a way that replicated the original tensile test. Subsequently, the accuracy of the models when used on multi-material samples was studied. A comparison between the strain maps generated by FEA simulations and physical tests were conducted. The results confirmed the validity of the models for multi-material simulations.

4.1.1 Test specimen

To recreate the tensile test, the same KS-M6518 test samples were utilized in the simulation. However, to speed up the simulation a 2D simplification was used. This was required due to the high computation demands of the MR3 and MR5 models.d Fig. 4.1 shows the 2D simplified sample utilized in the validation simulation.

Figure 4.1. 2D simplification of the test sample

4.1.2 Simulation parameters

As shown in Fig. 4.2 the simulation replicates the testing conditions, with the sample being held from one edge (datum A) while the other is subjected to a prescribed displacement (datum B). The strain results were measured at the center of the sample at the same location the extensometer recorded them in the tensile test. While the engineering stress was calculated by measuring the reaction force at datum B and then dividing it by the original cross-section.

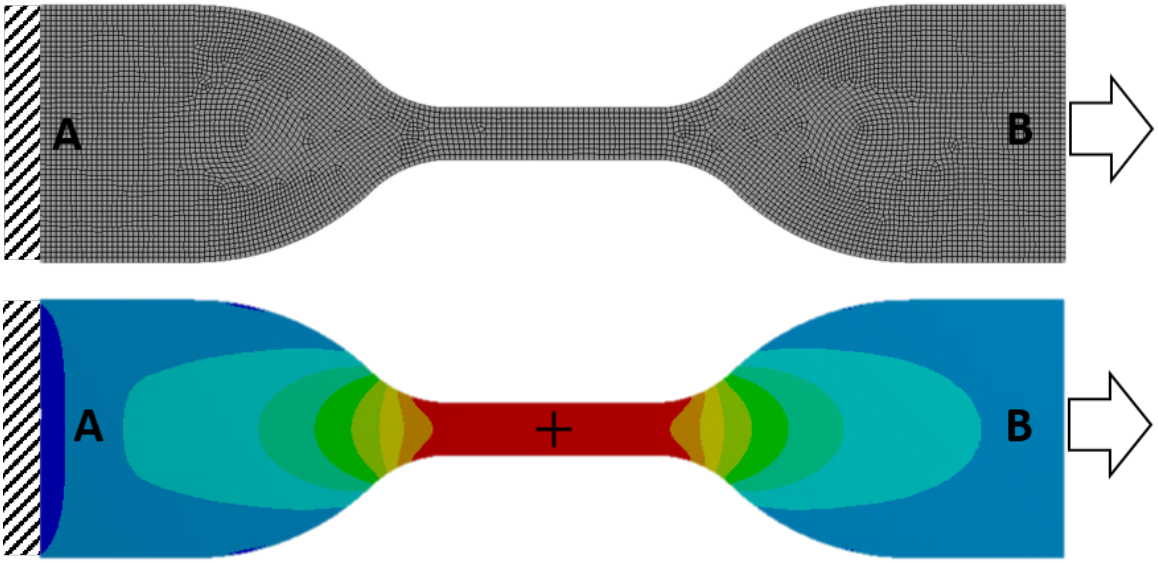

Figure 4.2. Simulation set up and results

4.1.3 Validation results

A comparison between the simulation results and the material models is shown in Fig. 4.3-4.6. As seen in the tensile test, the simulation results also display staggered stress-strain curves. DM40 the most elastic DM is at the bottom of the graph, close to TB+. While DM95 the DM with the most VW+ in its mixture is at the opposite end with the highest tensile strength. This is true for all the simulation results regardless of the material model. Moreover, the simulation results and the material models display the same curve shape. Both the NH model and the simulation results start linear and at a given point taper off. The MR2 model and simulation results display a much more pronounced stress-strain curve, this is clearly seen in the curve for DM95. Conversely the model and simulation results for the MR3 show two curvatures with an inflection point in between. Similarly, the model and simulation results for MR5 display the same multi-curvature shape.

However, at strain levels beyond 50% of the max elongation for each individual material the simulations results tend to overestimate the stress values. This is very visible on the curves for the MR3 and MR5 models, where the simulation results very markedly diverge from the material model. This is inaccuracy in the model is caused by the lack of information on the remaining stress curves needed for characterizing a material, compressive and shear. Despite this, the stress values for strains up to 40% closely follow the theoretical values for the material models and the tensile test.

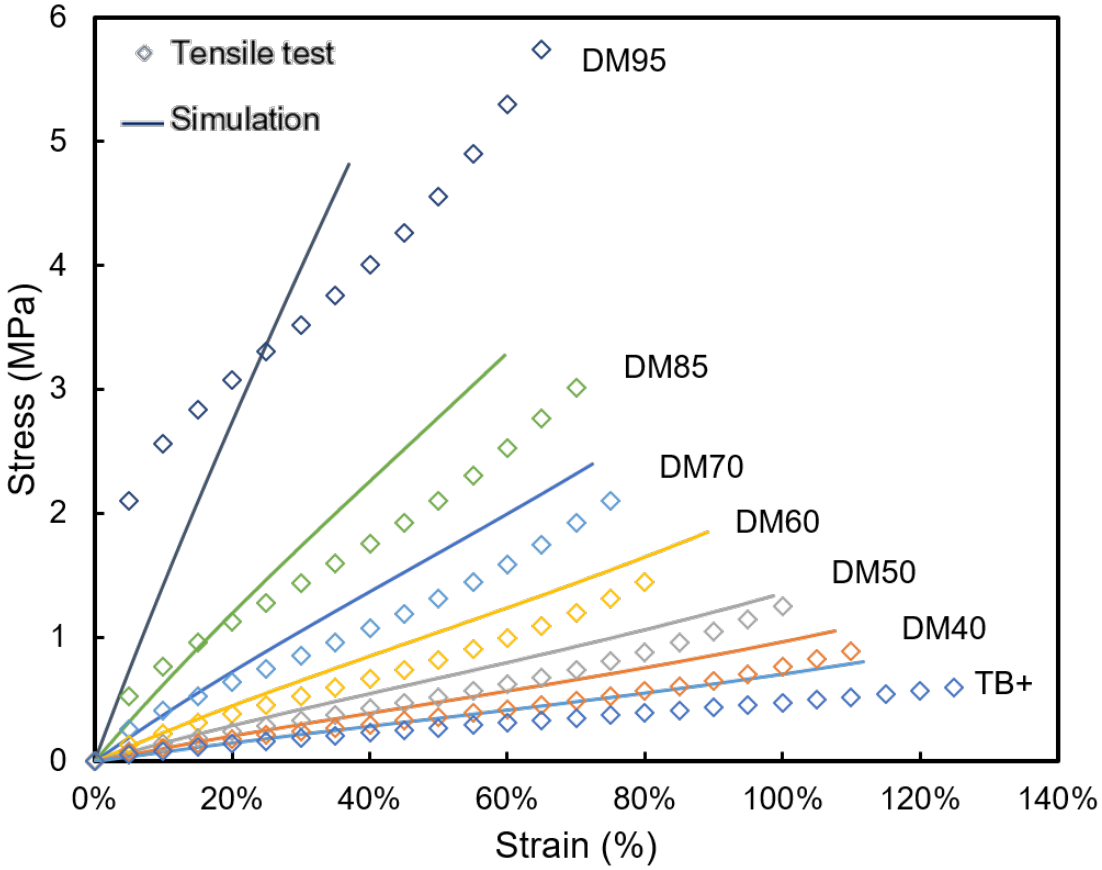

Figure 4.3. Comparison of the stress-strain curves from the tensile test and the simulation results for the NH model

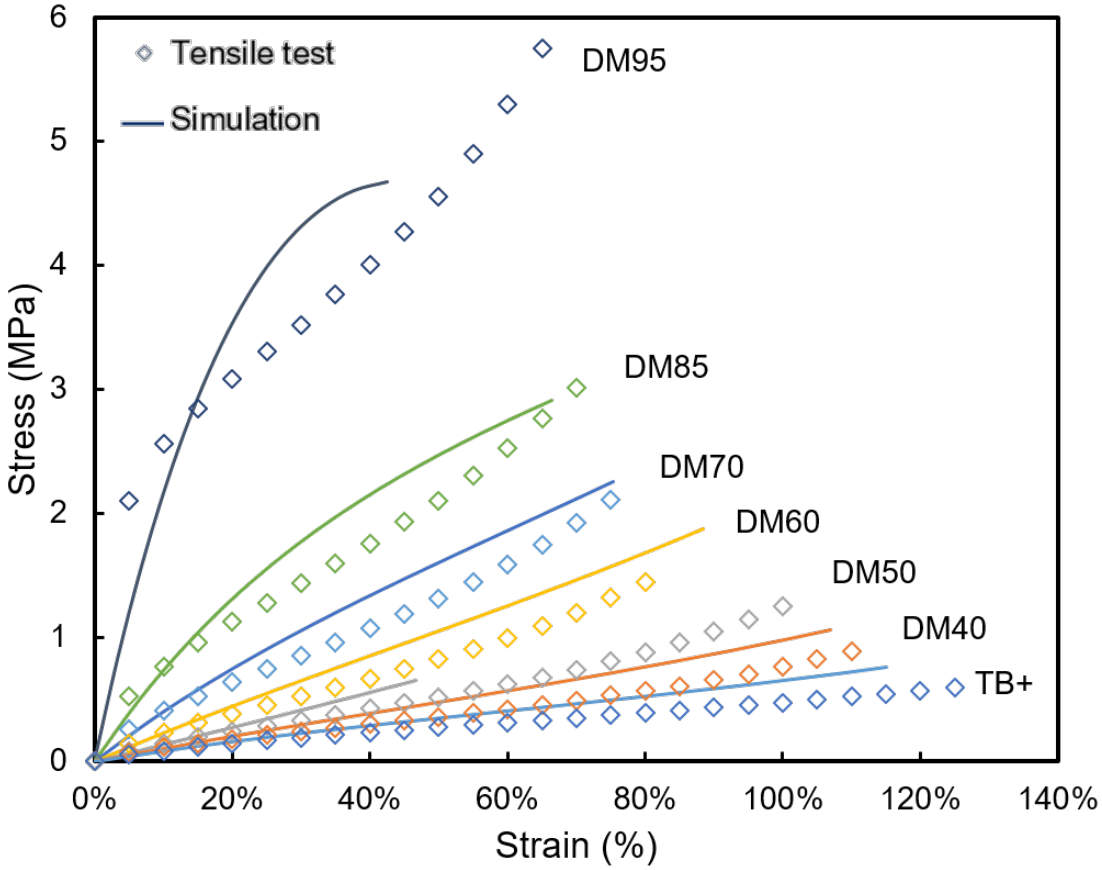

Figure 4.4. Comparison of the stress-strain curves from the tensile test and the simulation results for the MR2 model

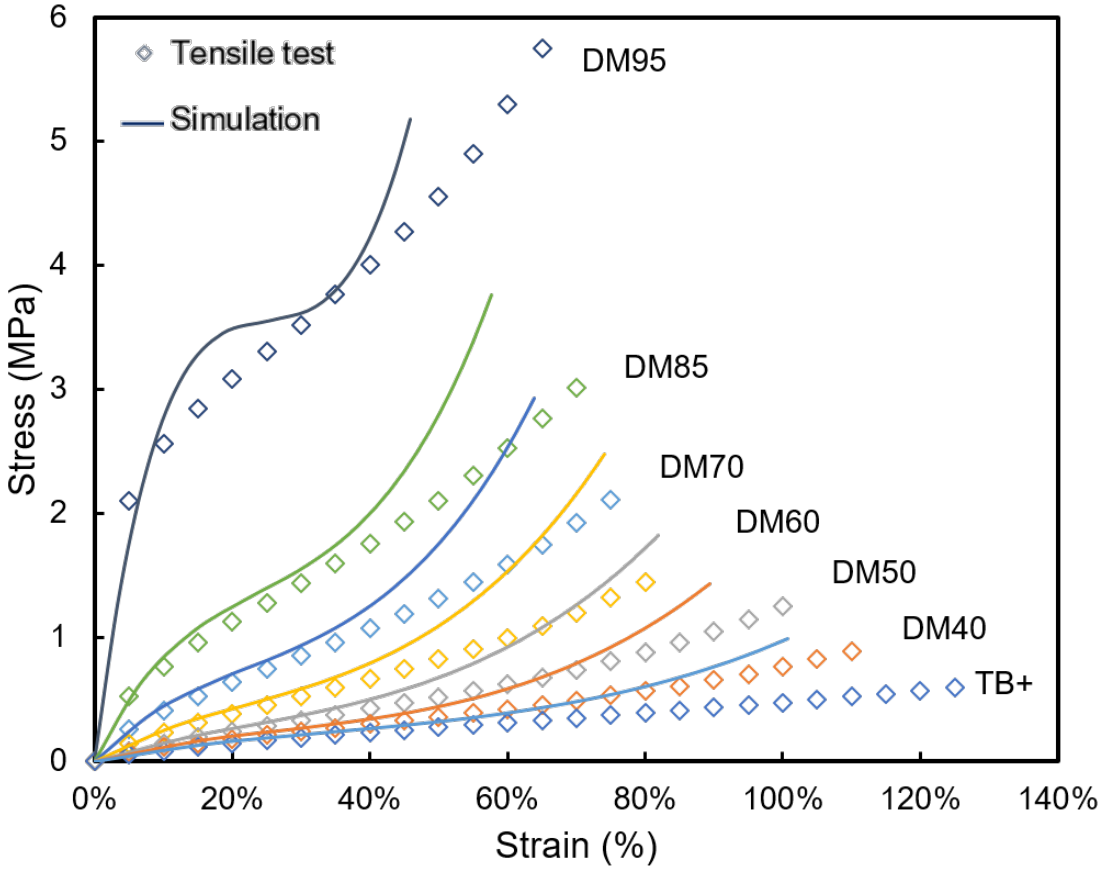

Figure 4.5. Comparison of the stress-strain curves from the tensile test and the simulation results for the MR3 model

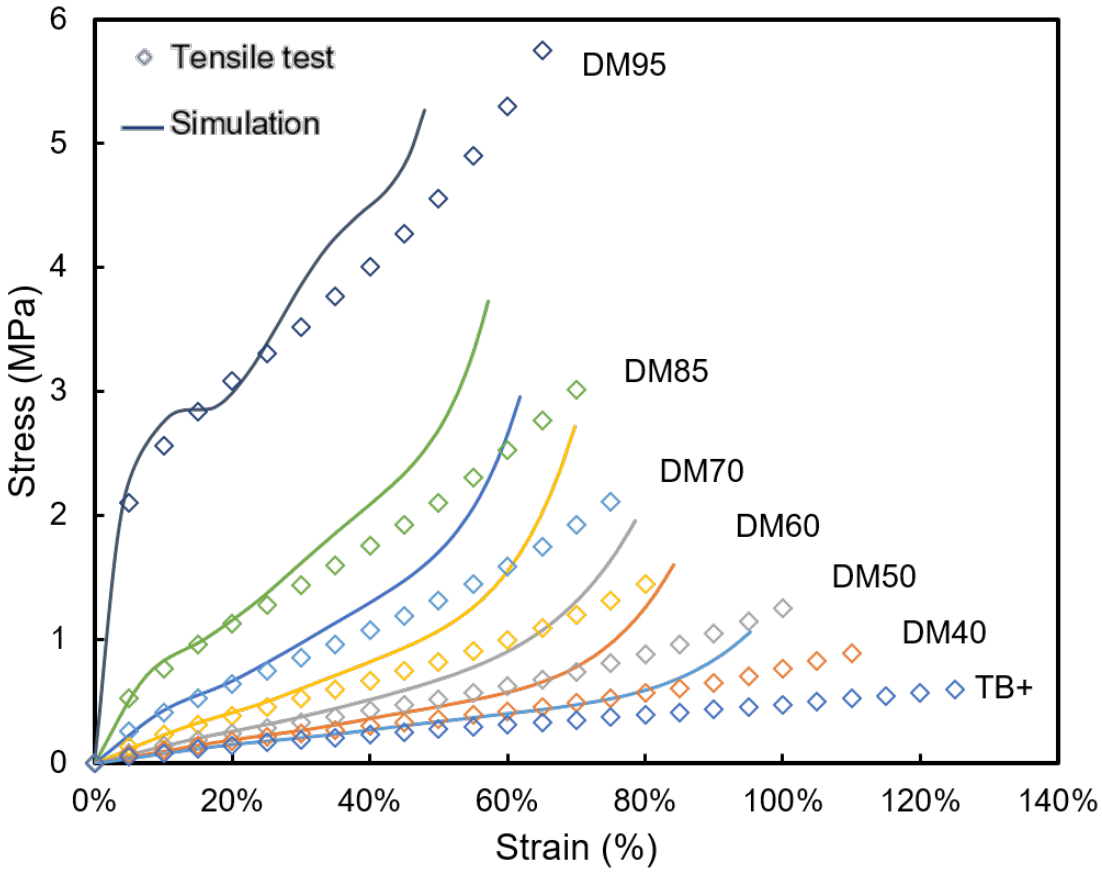

Figure 4.6. Comparison of the stress-strain curves from the tensile test and the simulation results for the MR5 model

4.2 Multi-Material validation

The goal of this section is to validate the accuracy of the material models when used in multi-material simulations. Furthermore, an SEM analysis of the interface between material regions was also conducted. This use case study will provide some insight into the considerations required when conducting simulation on multi-material samples.

To analyze the deformations experienced by multi-material prints strain maps generated from FEA simulations were compared to strain maps generated from the tensile tests. The focus of this section is on multi-material prints utilizing VW+, DM95, DM60, and TB+. By validating the accuracy of the multi-material simulations analysis of complex components made of two or more materials will be possible.

3D modeling and FEA simulations were conducted with SolidWorks 2016 (Dassault Systemes). Tensile test for the validation was performed with a 100-series modular universal test machine (UTM, Test Resources). Utilizing a video extensometer (Vic Gauge, Correlated Solutions) and an image analysis software (Vic 2D, Correlated Solutions), the strain distribution in the sample was analyzed and compared to the FEA simulation.

4.2.1 Test Specimens

To discern the effects of multi-material prints, four different configurations were tested. Fig. 4.7 shows the dimensions of tensile test specimens. Four sample design plans are summarized in Table 4.1.

- Sample 1 (S1) was printed utilizing only TB+ as a baseline.
- Sample 2 (S2) includes an embedded circular island made up of VW+.
- Sample 3 (S3) has a circular graded island, with different materials radiating from the center of the sample.

- Sample 4 (S4) has a rectangular graded island, with different materials radiating from the center of the sample.

Table 4.1. Summary of all the tested sample designs

	S1	S2	S3	S4
Island	-	yes	yes	yes
Shape	-	circle	circle	square
Gradient	-	no	yes	yes

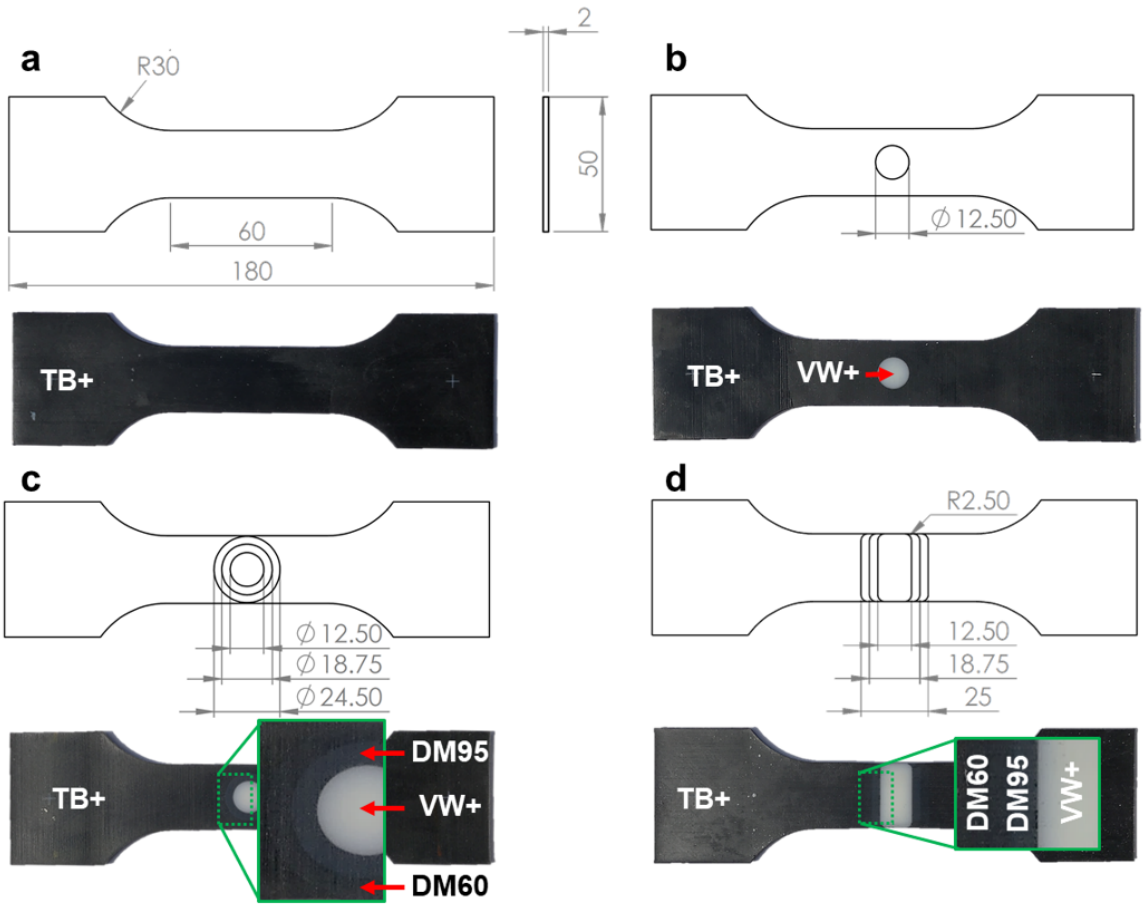

Figure 4.7. Multi-material test samples

4.2.2 FEA simulation

VW+ was modeled as a bilinear material with an initial Youngs modulus of 2.0 GPa and yield point of 10 MPa, and a second modulus of 650 MPa and yield point of 30MPa. The MR2 models of TB+, DM95, and DM60 were utilized to speed up the simulation process. The stress-strain curves are displayed in Fig.4.8 The individual models for each material were imported into the material library of the FEA simulation software (SolidWorks FEA) and assigned to the corresponding regions shown in Fig. 4.7. Non-linear studies were used in the FEA to simulate large deformations. Replicating the actual physical test conditions, the left side of the sample was fixed, while the right side was displaced up to 30 mm.

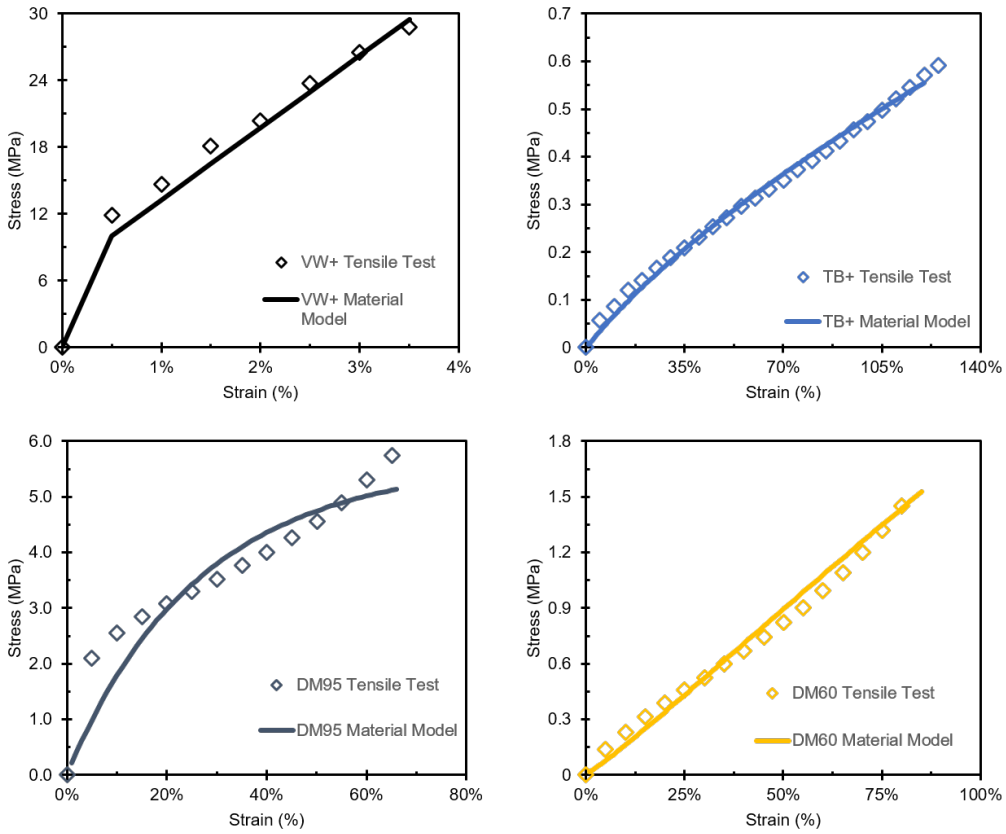

Figure 4.8. Stress-strain curve for VW+, TB+, DM95, and DM60 used in the multi-material simulation

During printing, the polymers are cross-linked by UV light after being deposited on the build plate. This allows the base materials to mix on the DM regions, and at the interface, at the interfaces, for some diffusion to occur. Therefore, the interface regions between different materials were modeled as perfectly bonded. Due to the mismatch in material properties, the transition regions were modeled with a finer mesh. Fig. 4.9 shows the center region of S2, S3, and S4, where the multi-material islands were printed.

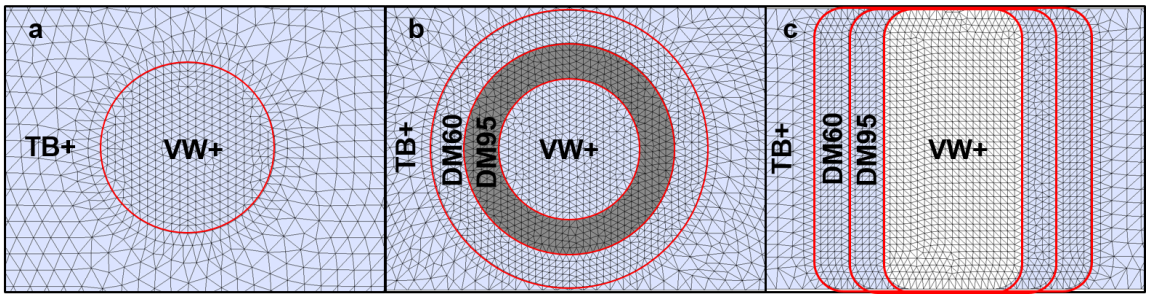

Figure 4.9. Mesh refinements and material arrangement

4.2.3 Multi-material tensile testing

The tensile tests of the printed samples were conducted with the UTM. The displacement was recorded with a video extensometer that measures the distance between markings on sample surface during deformation. The markings were generated by covering the samples with black paint and then by speckling with white spray paint to create a speckled pattern (Fig. 4.10).

The grips separate at a constant speed of 50 mm/min until the load cell recorded a sudden drop associated with the breakage of the sample or the grip reaches 30 mm of displacement (Fig. 4.11). The video extensometer continuously captures images of the sample as it deforms.

These images are then imported into the analysis software (Vic 2d, Correlated Solutions) where the gauge block (green square in Fig. 4.12) and the analysis window (red shaded rectangle in Fig. 4.12) are set. These two things control the strain mapping of the sample. The analysis window grows as the sample is stretched, this is illustrated in Fig. 4.11. For the strain map analysis of the multi-material samples, one sample was used for the comparison.

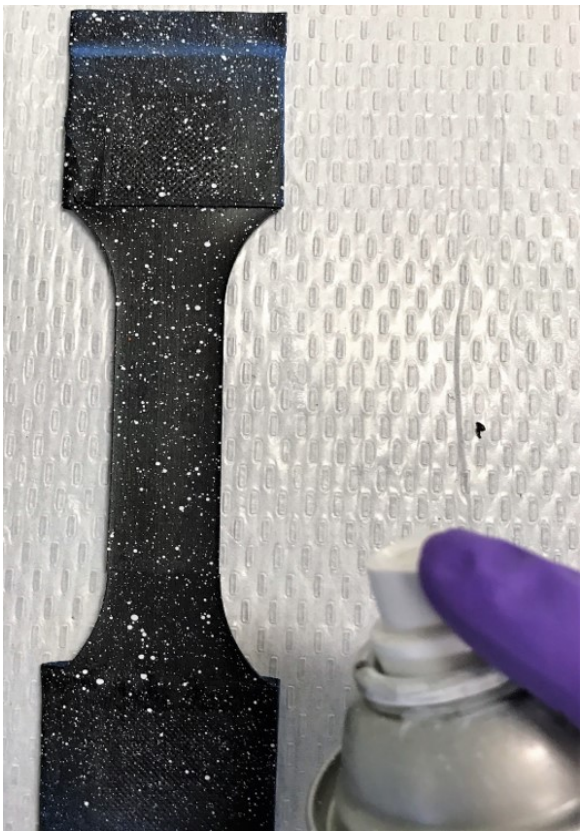

Figure 4.10. Multi-material sample preparation

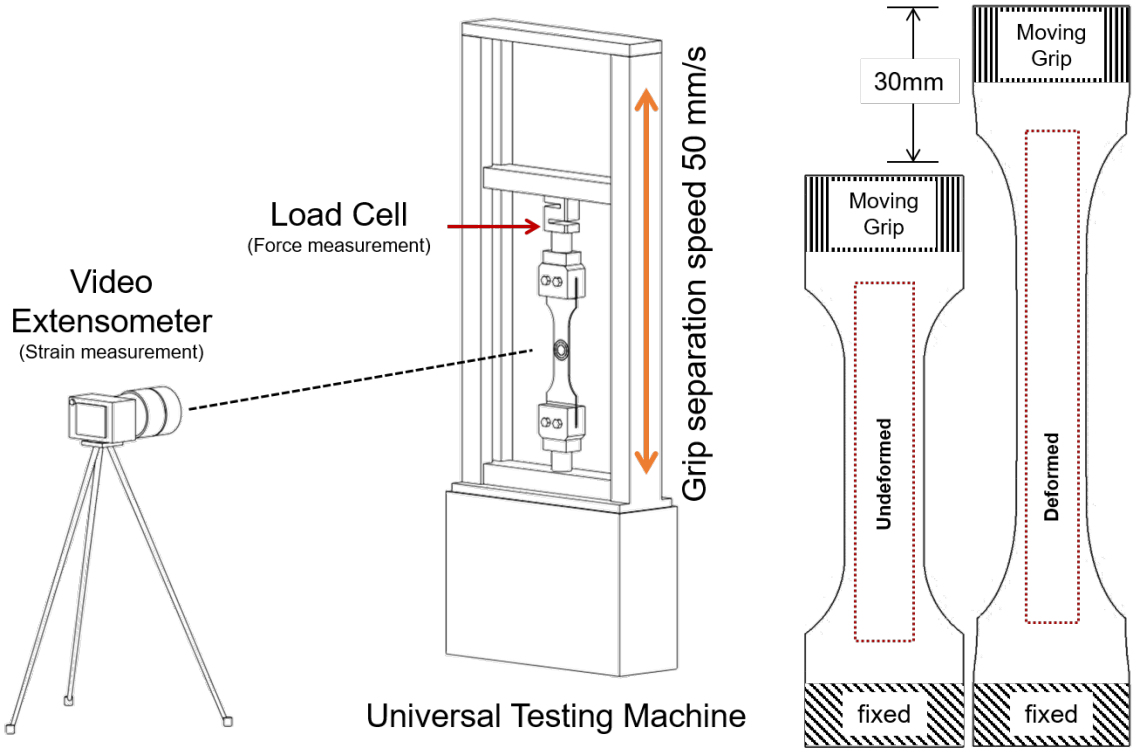

Figure 4.11. Schematic of the multi-material tensile test

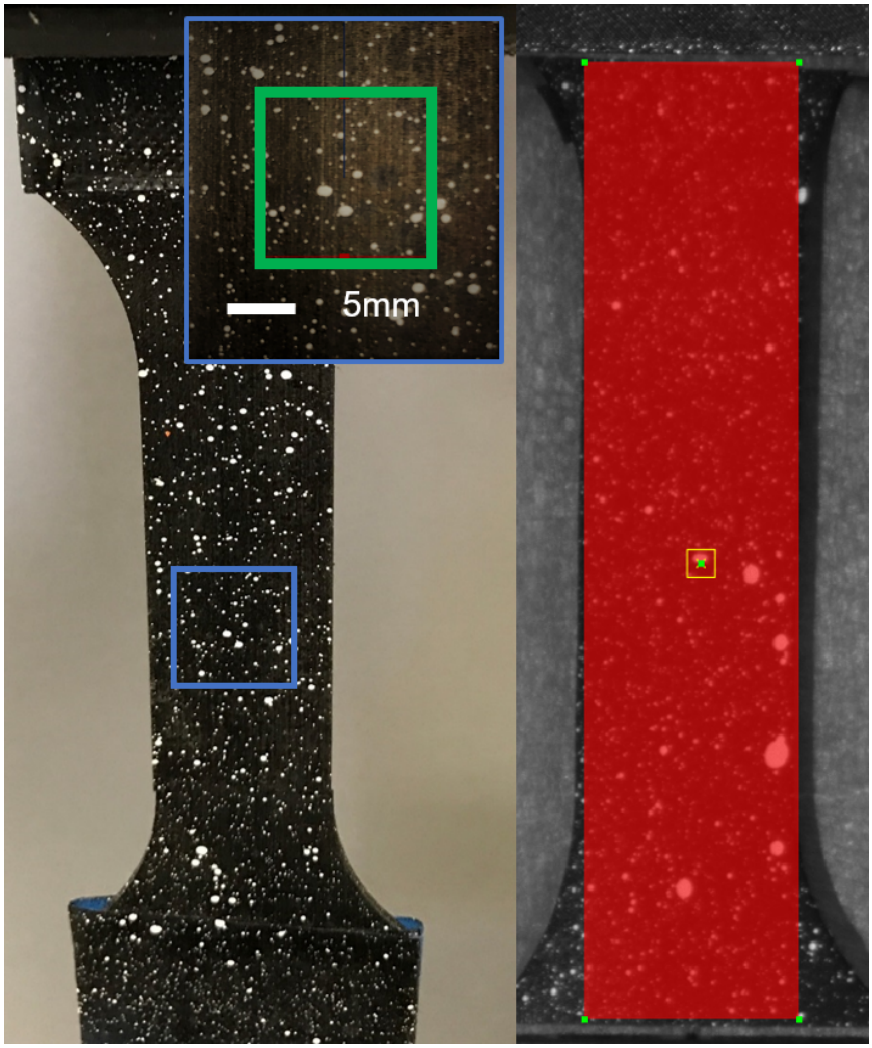

Figure 4.12. Multi-material test analysis software set-up

4.2.4 Multi-material validation results

The strain patterns of S1-S4 produced by the extensometer software at 30 mm displacement are shown in Fig. 4.13. At larger deformations, cracking of the paint on the sample surface affects the data acquisition and causes holes on the strain maps. As S1 deformed, it experienced uniform strain levels, shown by an almost uniform color throughout the gauge length. In contrast, multi-material samples (S2-S4) exhibited distinct strain patterns caused by the shape of embedded material islands. S2 and S3 display similar strain distributions as they share the same underlying shape. However, S3 which has a graded transition, displays lower strain surrounding the VW+. The strain gradient shown in S3 is also observed in S4, this gradual transition is caused by the different levels of compliance in the DMs surrounding the rigid center.

The strain patterns produced by the FEA simulation are shown in Fig. 4.14. The strain patterns for each sample were analogous to those from the tensile test (Fig. 4.13). The single material sample, S1, showed uniform strain levels throughout, while the multi-material samples displayed unique strain distributions depending on the shape of the embedded island. S1 displays a maximum strain level of 26%, shown in green throughout its gauge length. S2, the first sample with an embedded rigid island experienced lower strain levels on the TB+ regions and high strain concentration levels at the VW+ interface. Conversely, S3 the first graded island sample, showed lower levels of strain immediately surrounding the VW+ region. Each material region experiences varying degrees of strain; with VW+ showing less than 1% strain, DM95 being more compliant experienced less than 2%, DM60 had a maximum of 20% strain and TB+ the most elastic material experiences strain in the range of 20% to 40%. S4, which also has a graded transition, displays a similar pattern of strain distributions as S3, with the VW+ region experiencing no strain and each subsequent material region experiencing higher levels of strain.

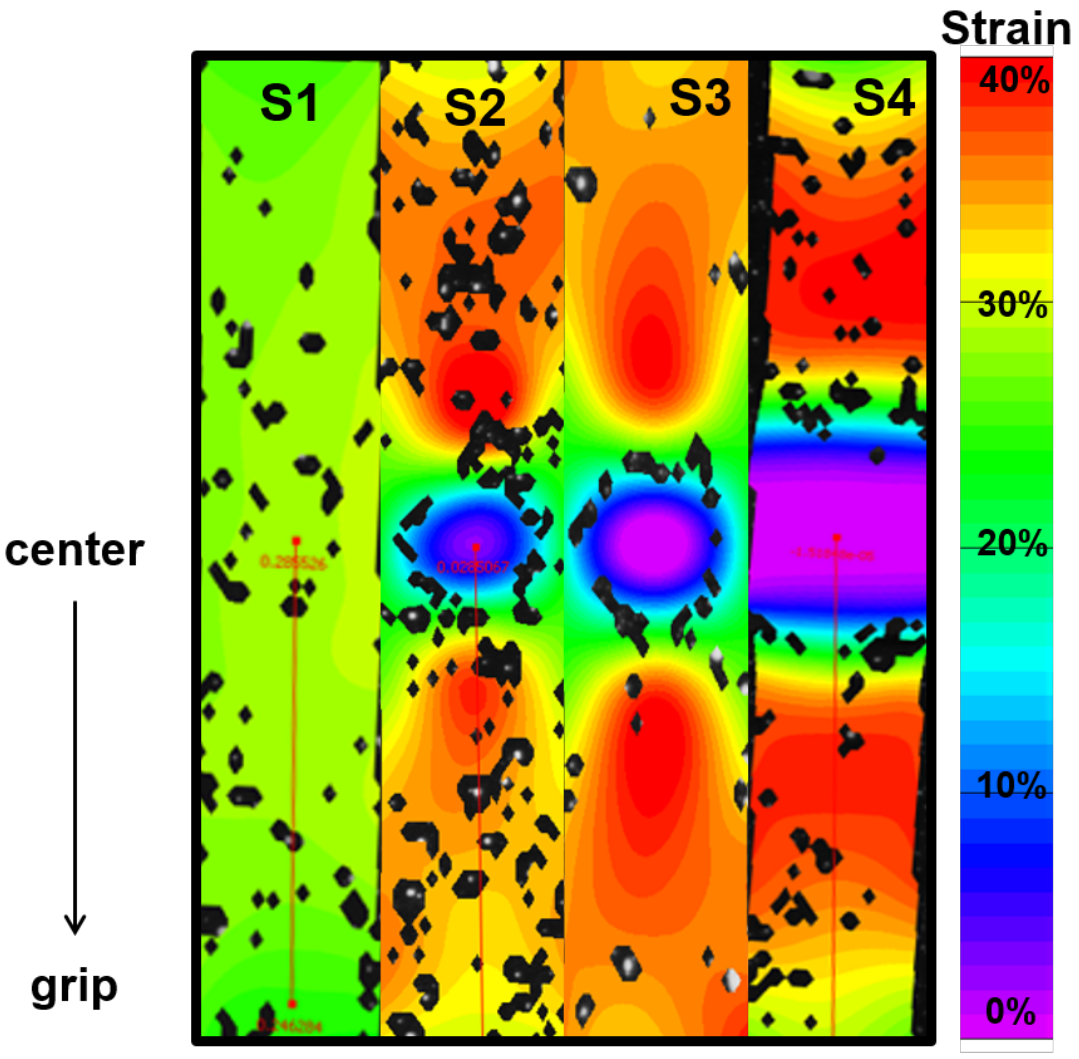

Figure 4.13. Strain map generated by the non-contacting extensometer software

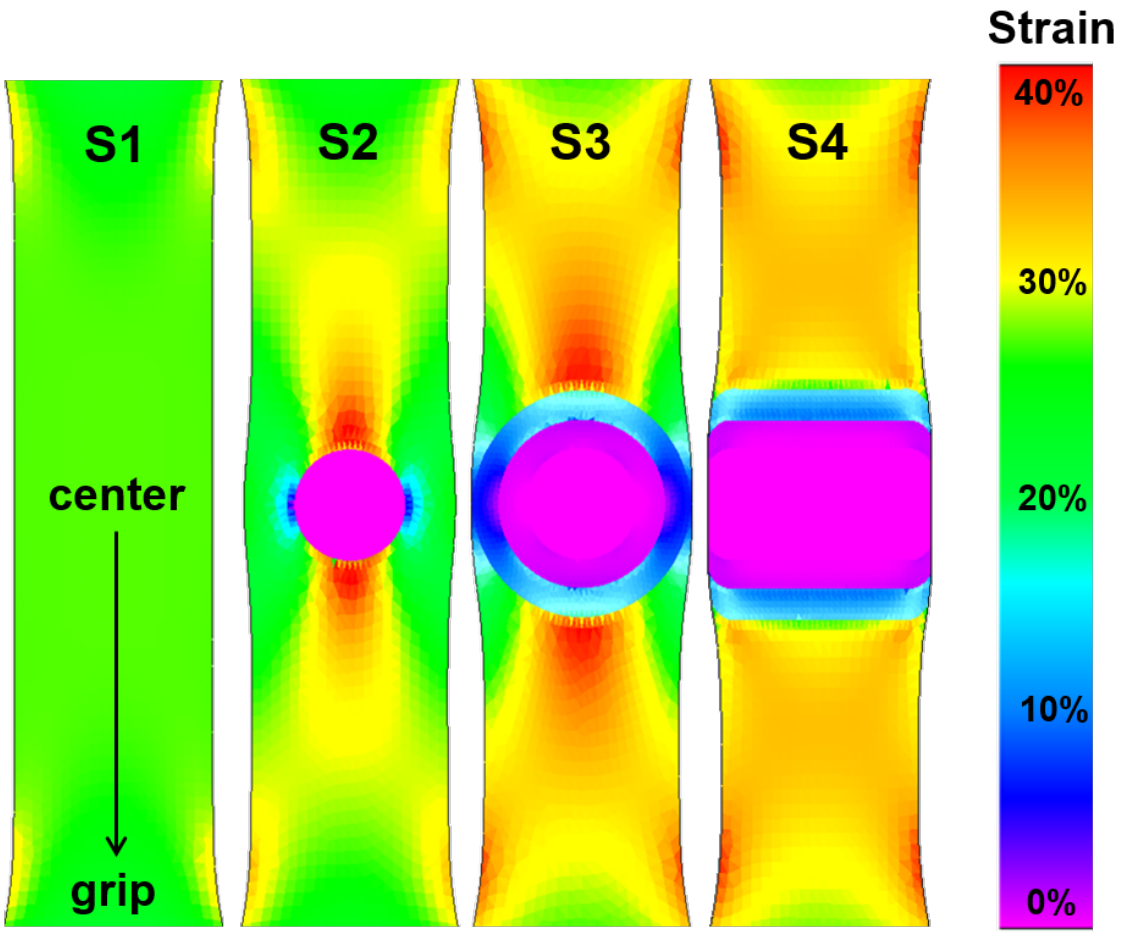

Figure 4.14. Strain map generated by the simulation results

A comparison of the strain values and locations between the simulation and the physical test for S1-S4 are shown in Fig. 4.15. The location of maximum strain in each sample occur closer to the embedded islands on the simulation results. This disagreement is associated with the geometric assumption in FEA model. The simulation model assumes perfect boundary and bonding between different materials (VW+, DMs, and TB+). However, during printing and curing phases, the inks diffuse into each other at the interface between the heterogeneous materials. This inter-ink diffusion creates an intermediate region that reduces the abrupt change in material properties and stress.

The interface region can be observed in Fig. 4.16, which shows the interface region between TB+ and VW+. Both SEM (Fig. 4.16a) and visual (Fig. 4.16b) images of the transition region show an intermediate region between the two materials. This intermediate area occurs at the junction between any two materials and is caused by mixing prior to curing. This diffusion region strengthens the bond between the different materials while also creating an unintended area with intermediate material properties.

As shown in the inset of Fig. 4.15, the break occurs at some distance from the embedded islands in the gradient materials and a close distance in the single material sample. The gradient transition reduces the amount stress that TB+ experiences at the region close to the center of the sample, shifting the stress concentration away from the center causing the break to occur in the TB+ region. In S2 the highest concentration occurs at the junction between VW+ and TB+ causing the break to occur near the interface between the two materials. As shown in other publications, the interface between materials is not inherently weaker and therefore not necessarily where the break will occur.

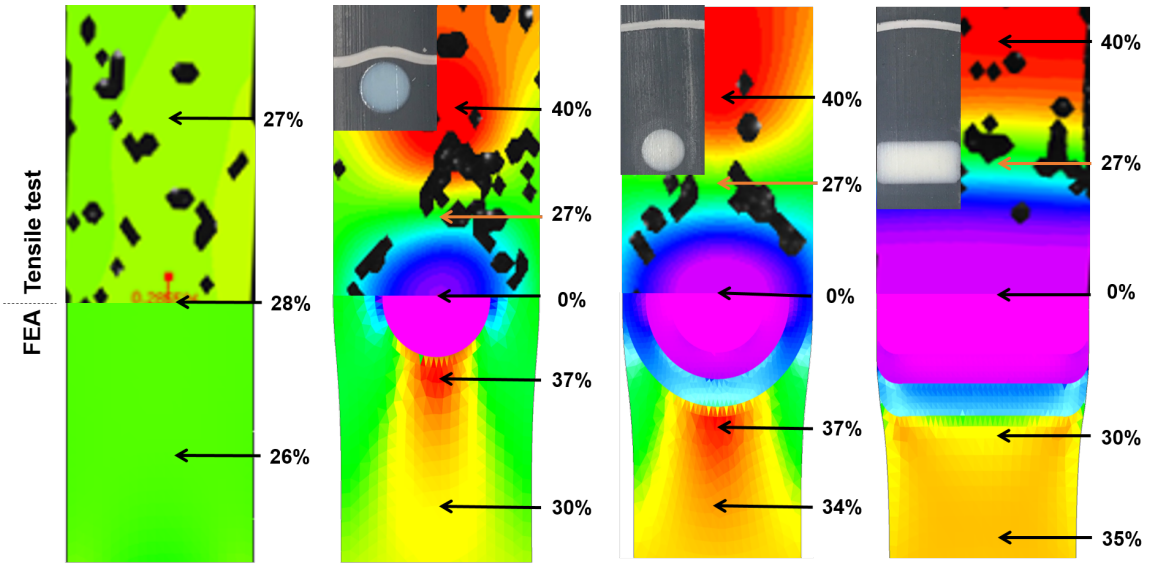

Figure 4.15. Comparison of the strain maps for all samples

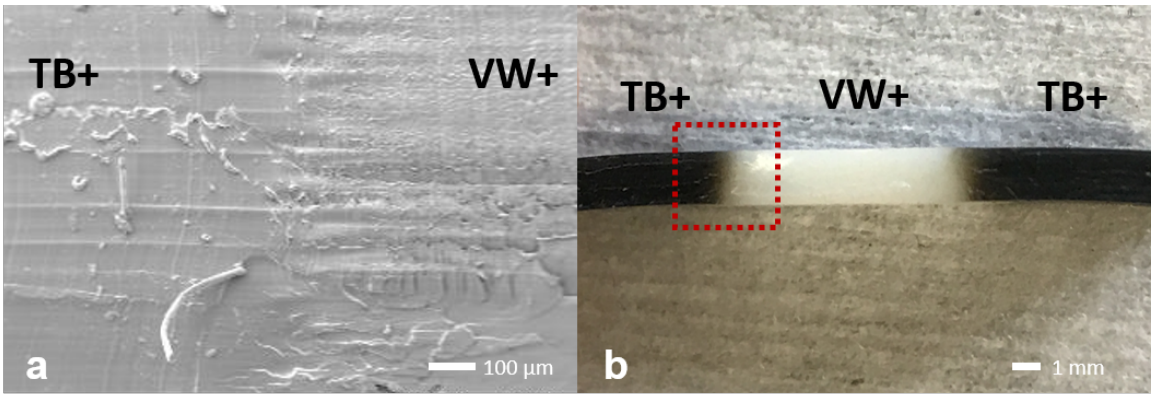

Figure 4.16. Cross-sectional analysis of the interface region between VW+ and TB+ in both (a) SEM image and (b) visual image

A strain level comparison between the simulation results and the tensile test data for S1-S4 is shown in Figs. 4.17-4.20. The probe points were selected from the center of the sample towards the edge of the analysis window (in the tensile test) or the grip boundary (in the simulation). 21 points were selected for the simulation results plotted at 3.25 mm intervals, while for the tensile test, a line was plotted from the center to the edge of the viewing window and multiple points along that line being analyzed. As shown in Figs. 4.17-4.20, both physical test and FEA results show almost identical strain curves.

S1 exhibits a slow decrease in strain as the points move away from the center to the grip (Fig. 4.17). S2 displays low levels of strain at the center of the sample and as the points transition away from the VW+ (i region) to the TB+ (iv region) the strain rapidly increases approximately to 35% and then slowly decreases (Fig. 4.18). Meanwhile the samples with the gradient transition (S3 and S4) exhibit a gradual change in strain levels as shown in Fig. 4.19 and Fig. 4.20. As mentioned before, due to model assumptions at material junctions the simulation results have a slight shift in their plot. The maximum strain is observed at a closer distance from the center in the simulation results. Additionally, the un-graded island (S2) shows a sharper increase in strain when compared to the graded island designs (S3 and S4) in both simulation (Fig. 4.21) and physical test (Fig. 4.22).

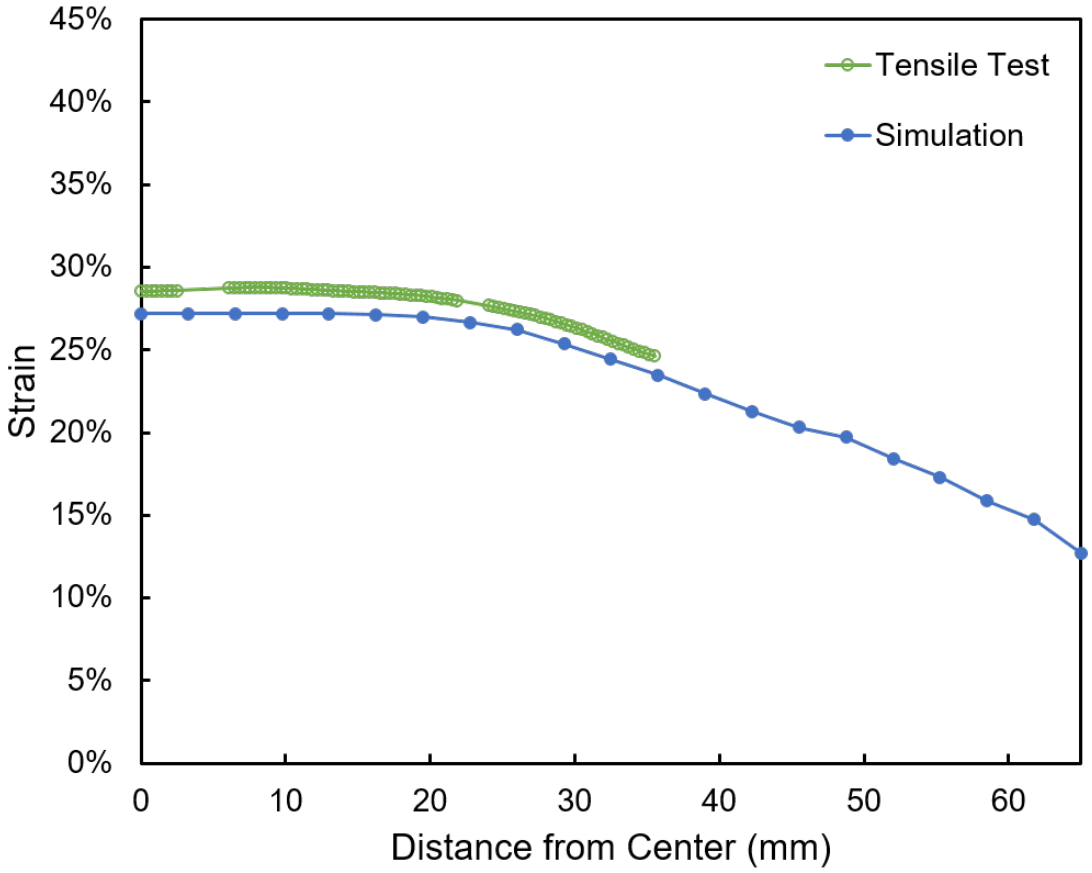

Figure 4.17. Probe analysis of strain levels between the simulation result and physical test for S1

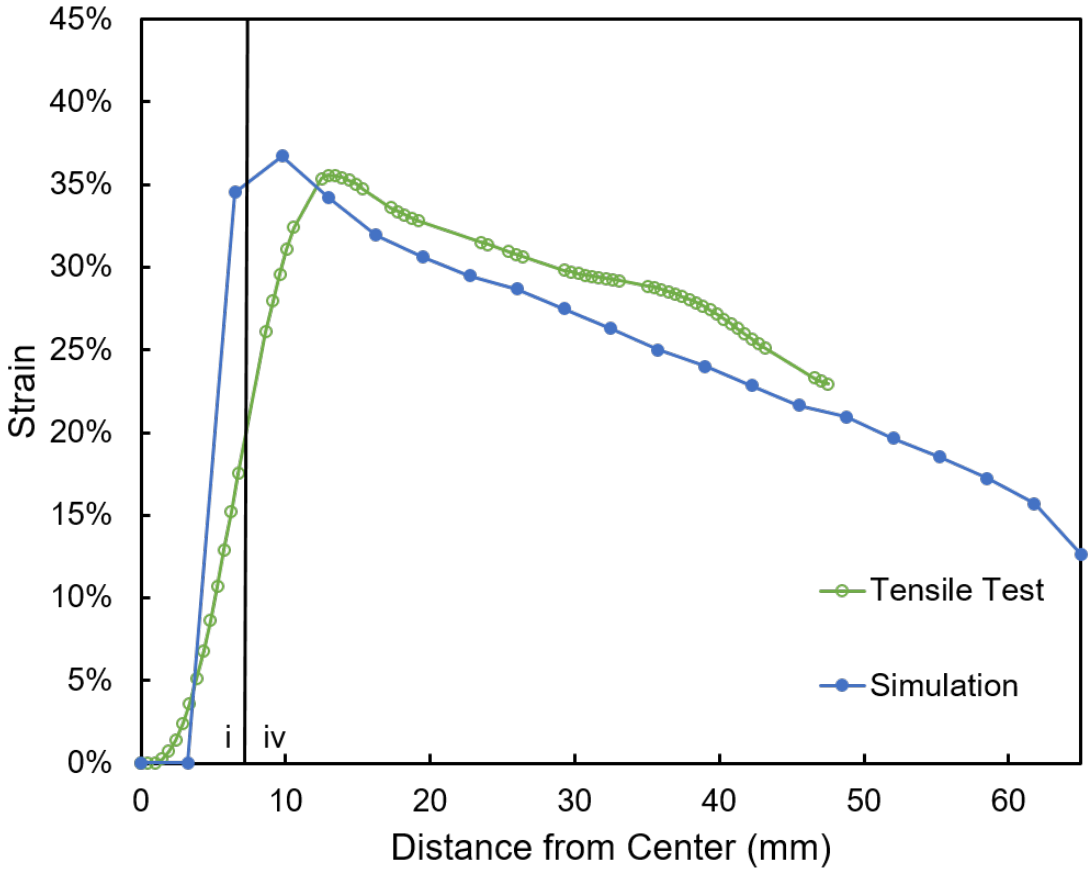

Figure 4.18. Probe analysis of strain levels between the simulation result and physical test for S2

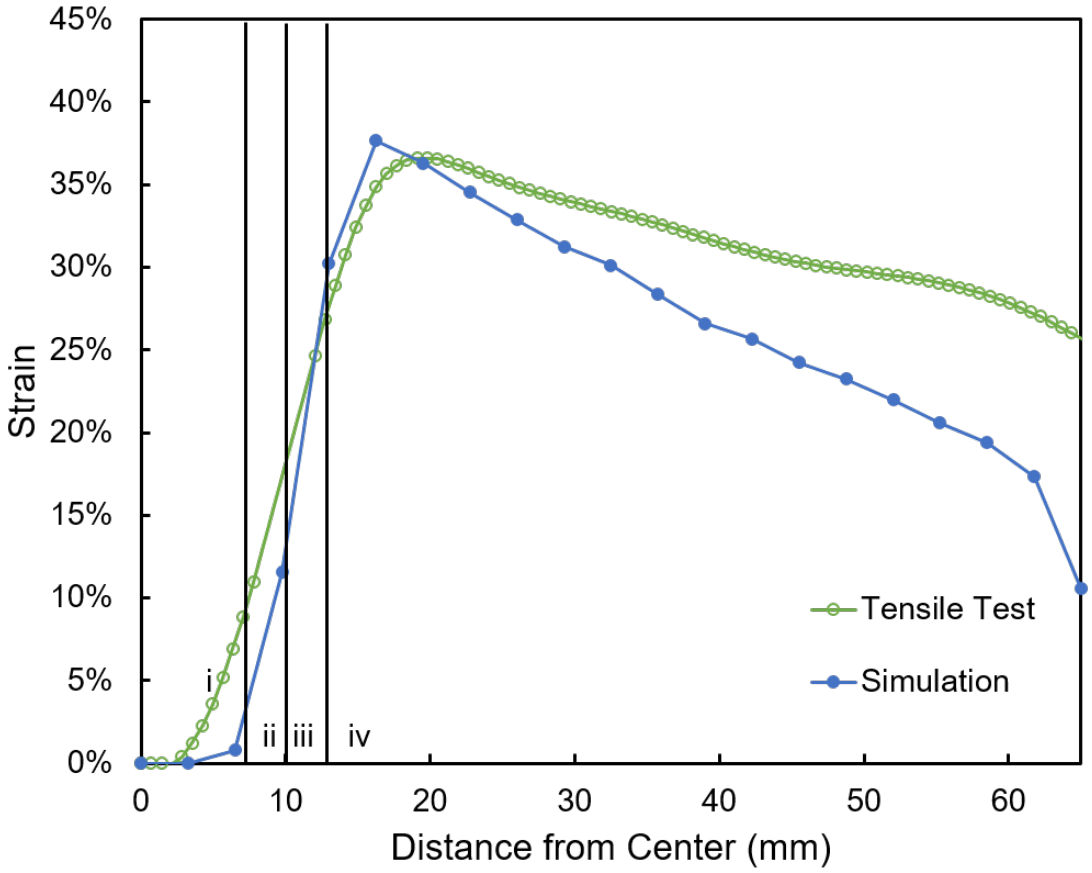

Figure 4.19. Probe analysis of strain levels between the simulation result and physical test for S3

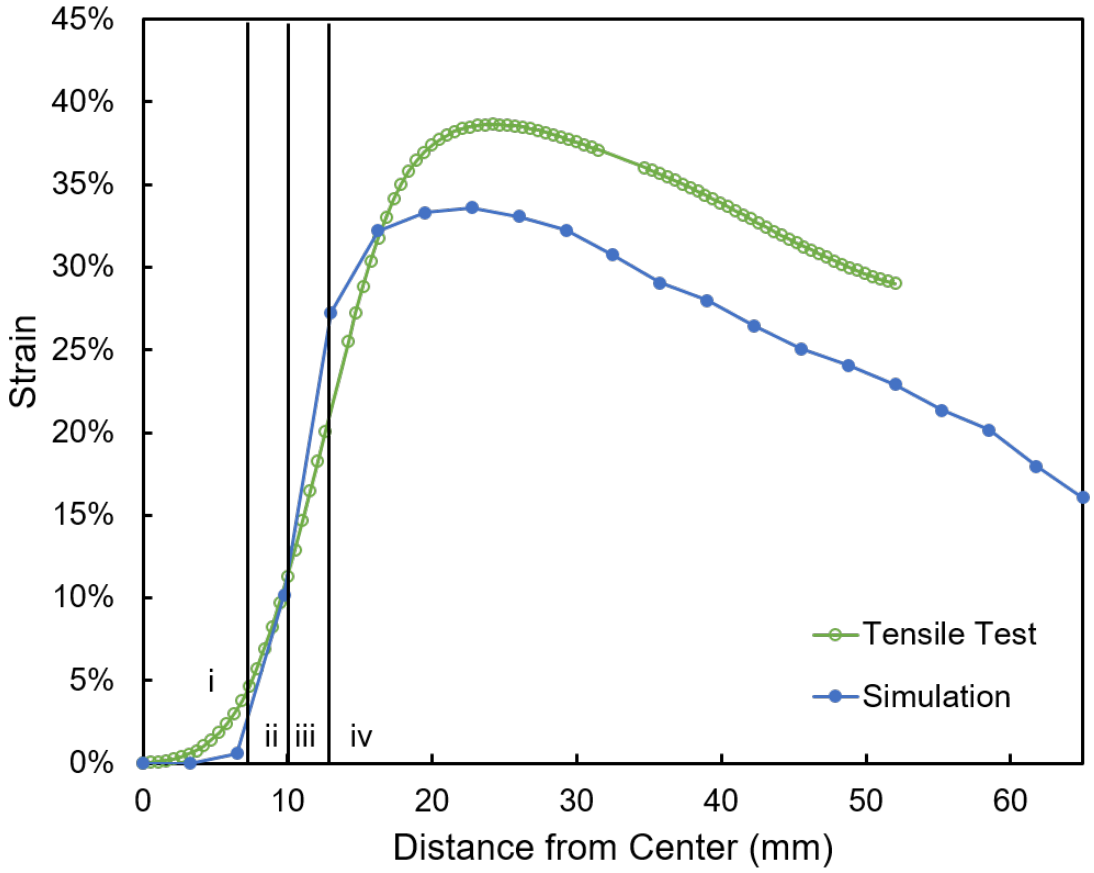

Figure 4.20. Probe analysis of strain levels between the simulation result and physical test for S4

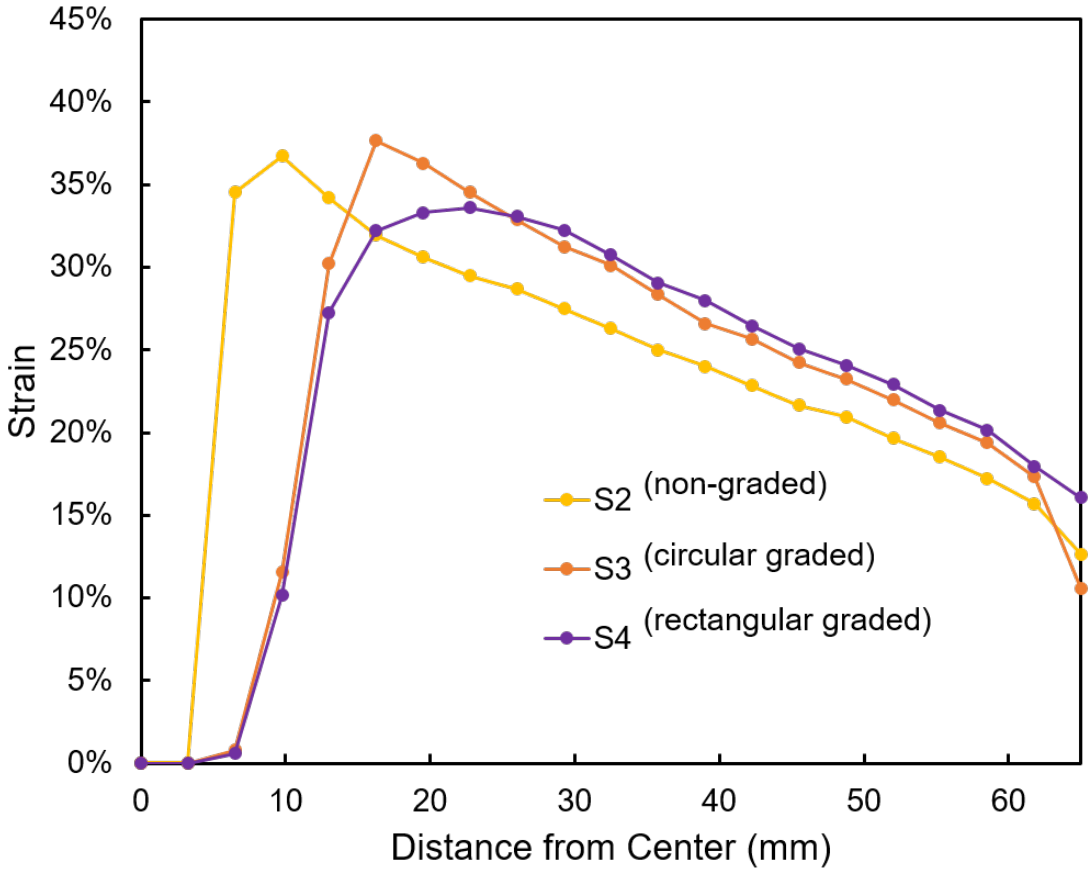

Figure 4.21. Comparison of strain levels for the simulation results of S2, S3, and S4

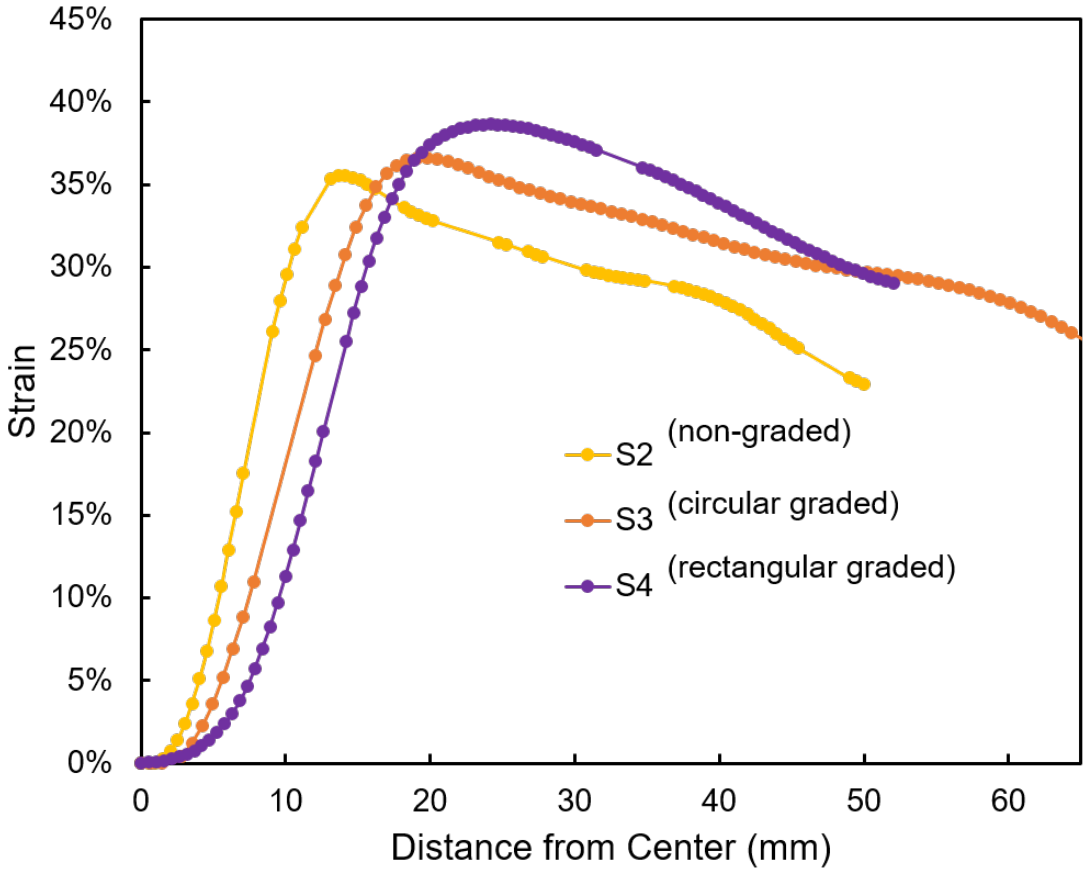

Figure 4.22. Comparison of strain levels for the tensile test results of S2, S3, and S4

4.3 Summary

In this section, the newly fitted material constants were used in an FEA simulations to validate the accuracy of the material models. The simulation results displayed the same staggered behavior as seen in the tensile tests and the material models. However, the simulation results diverged from the material model for strain values above 40%. This was attributed to the lack of information on the other stress states, shear and compression when fitting the model. The divergence was more pronounced on the MR3 and MR5 models.

While the current simulation results tend to overestimate the stress values at elongations over 40% the material constants found in this study provide a starting point in the comprehensive characterization of DMs printable with MJ.

This section has also shown that the FEA method can be utilized to predict the deformation and stress concentrations of multi-material parts printed, such as FGMs, by the MJ printer. The uniaxial tension test results matched well with the strain distributions predicted by FEA simulations based on our material models. The material models and FEA methods studied herein facilitate the design of FGMs in advanced applications with high fidelity of predictive analysis. Based on the result of this study, it is possible to create a desired strain field by locally changing the ratio of the DMs without changing the overall shape.

5. CASE STUDIES

5.1 Flexible-elastic circuits

This section presents a novel way for designing and manufacturing elastic substrates with embedded isolating regions for rigid component placement using a commercial material jetting printer (Connex 500, Stratasys). Transition regions between the rigid isolators and the elastic matrix material are printed with digital materials. In this use case, TB+ is used as the elastic matrix and VW+ for the rigid isolators. DM60 and DM95 were used as the transition materials due to their intermediate material properties.

Horseshoe interconnect pattern was stencil printed on to the substrate utilizing an elastic silver(Ag)-nanoparticle paste. A zero-ohm resistor was placed and soldered on the embedded stress isolator to mimic an off-the-shelve surface mounted device (SMD). Tensile testing was performed to evaluate reliability of the integrated stretchable electronics based on the additively manufactured elastic substrates.

5.1.1 Tensile test sample:

The samples share the same overall design (Fig. 5.1), at opposite ends, there is a rigid section to facilitate gripping, will the section in the center is printed in TB+ making it highly elastic. Close to the gripping areas embedded isolators are located allowing for the secure connection of the measurement probes. Three different samples were tested and compared, the sample designs are shown in Fig. 5.2 below. The baseline sample has no embedded isolating region, while sample two has a circular isolator made up of VW+. The final sample has a gradient isolator composed of the VW+, DM95, and DM60.

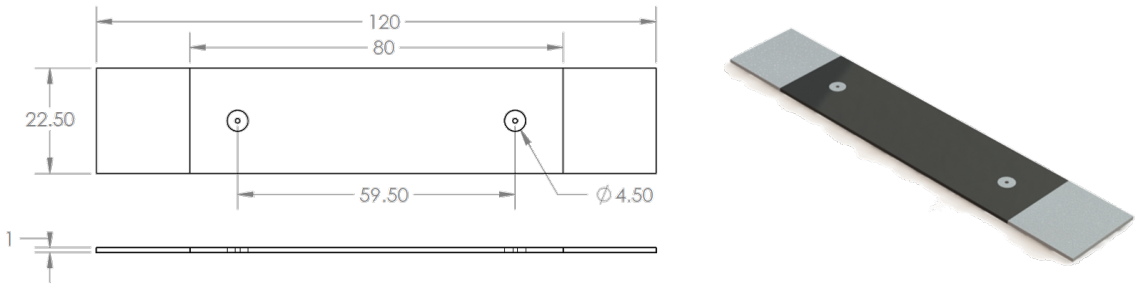

Figure 5.1. Baseline test sample dimensions

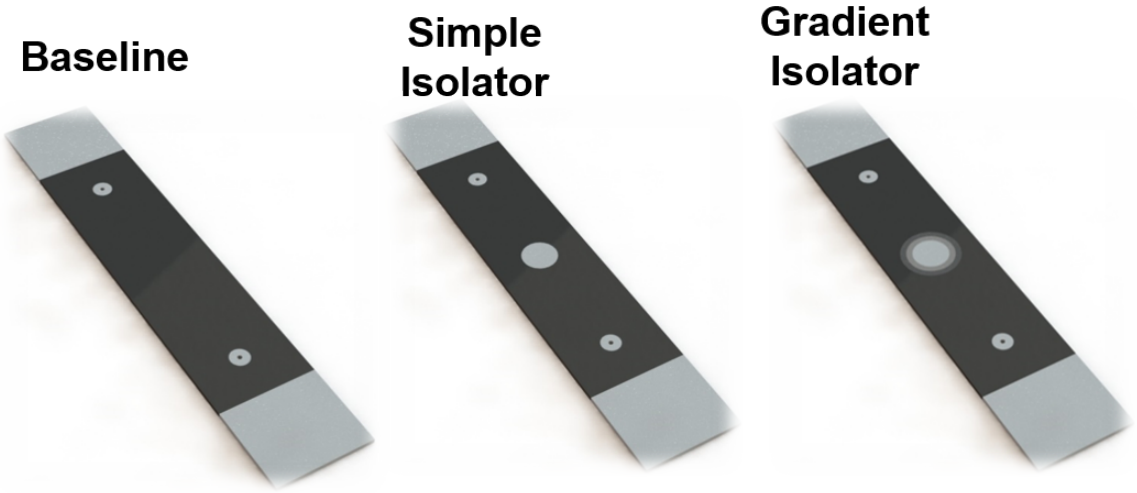

Figure 5.2. Design of all the test substrate samples

5.1.2 Circuit design:

Using conventional meander patterns, the circuit was designed as a repeating horse-shoe or S. The parameters used to describe the repeating pattern and the representing shape is shown in Fig. 5.3. A 1210 zero-ohm resistor was utilized as a shunt, mimicking a conventional SMD component. DuPonts PE 872 conductive paste was utilized to create the circuits.

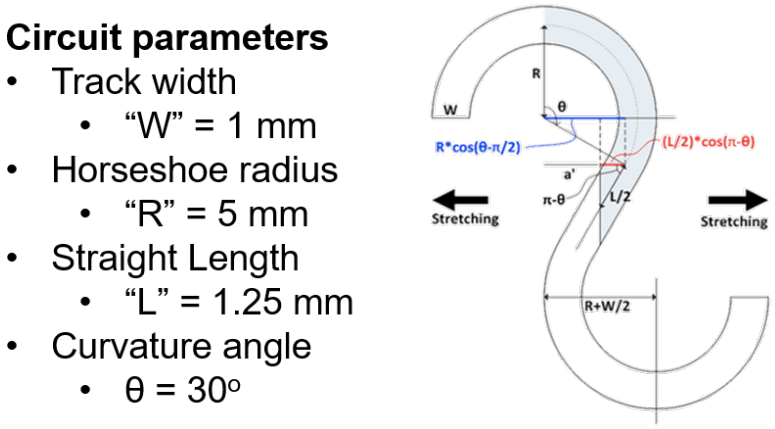

Figure 5.3. Circuit design schematic

5.1.3 Sample preparation

After printing the sample and conducting the necessary post-processing the samples were stencil printed. The circuit-printing process was conducted in three main steps, summarized in Fig. 5.4. First, the desired interconnect pattern is cut on a plot cutter. The design is then overlaid on the sample and utilizing a blade the conductive paste spread across. The sample is then cured or sintered depending on the requirements of the conductive ink used. Subsequently, cold solder is applied in the desired locations and finally the necessary components placed on the substrate.

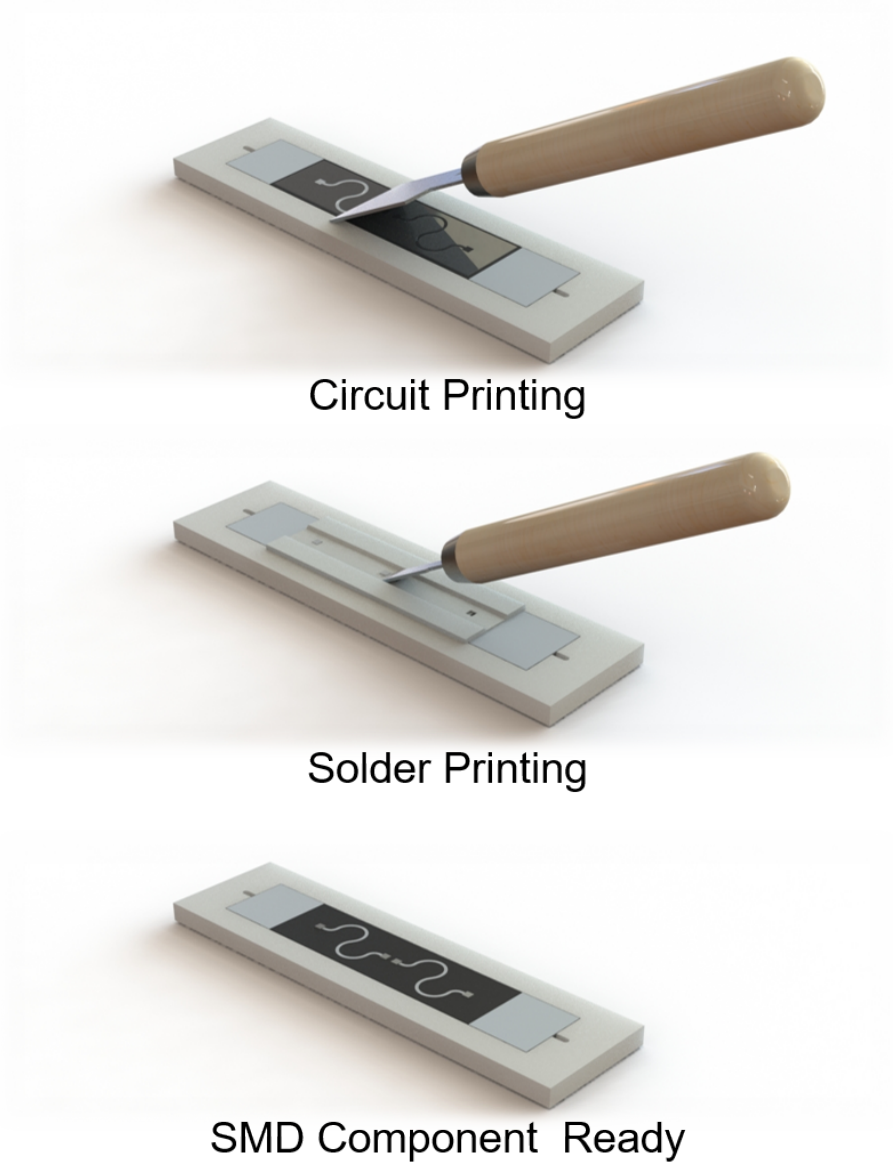

Figure 5.4. Schematic of sample preparation

5.1.4 Flexible-Elastic circuit results

Using a tensile test setup in a universal testing machine (TestResources), samples were secured with a fixed grip while the opposite grip was moved back at a constant velocity (1mm/s) until the desired elongation was reached (30% strain). While the sample is being strained, a constant voltage is being run through the circuit and the current measured, these values are then used to calculate the resistance of the sample under strain. Fig. 5.5 shows the testing setup, while Fig. 5.6 shows the three samples at full elongation (30% strain).

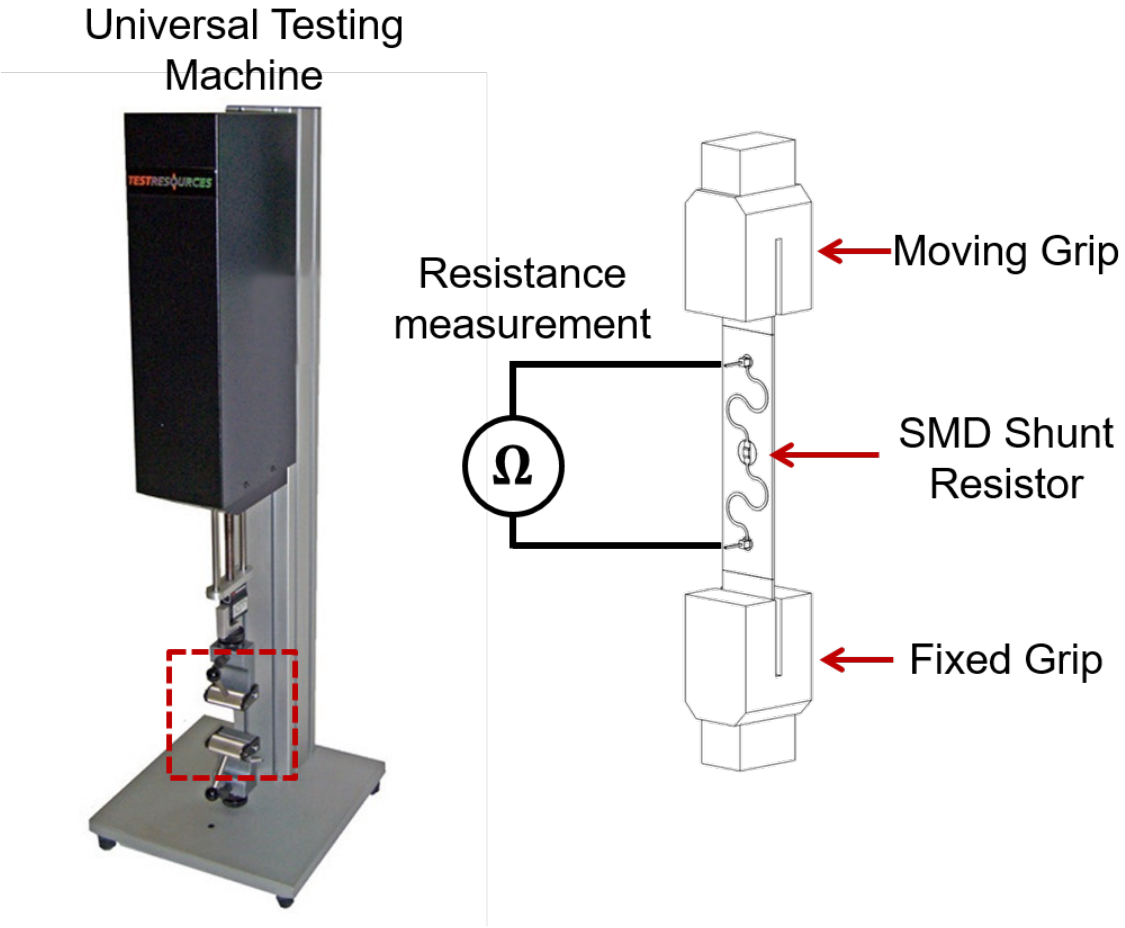

Figure 5.5. Test set up for the flexible electronic samples

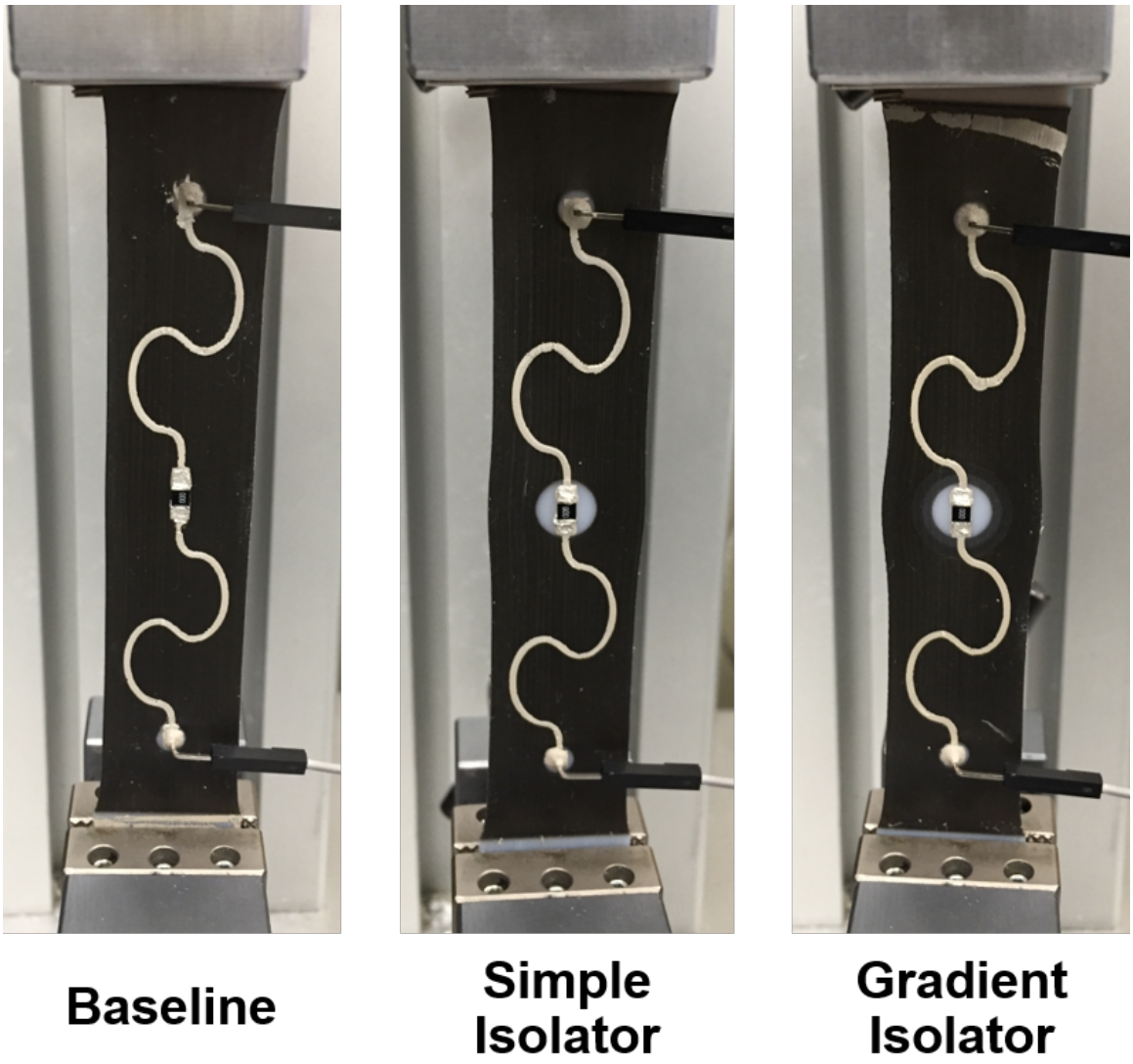

Figure 5.6. Deformed images of the test samples

In this section, its been shown that MJ is an applicable process for the creation of elastic circuits with rigid components. Furthermore, this process allows for gradient transitions to be incorporated in the design of the flexible substrate increasing the protection of the rigid components on the substrate. The data from the test was plotted for the three samples. Fig. 5.7 shows the delta resistance vs strain curves for all of the samples tested. While the baseline sample was conductive up to 10% the isolator samples were both conductive at higher strains (upward of 15% strain).

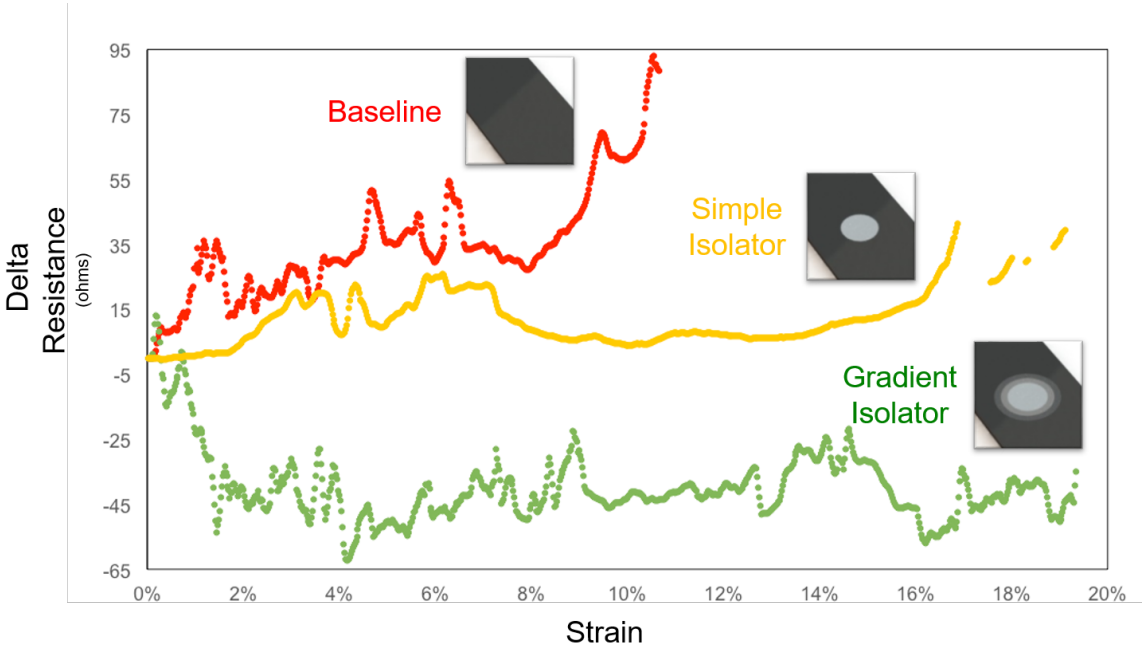

Figure 5.7. Delta resistance vs strain comparison of the tested samples

5.2 The Swollen-Off process

In this section, a novel method for fabricating 3D circuits on 3D substrates is presented. The method leverages the different hygroscopic swelling behavior of two different polymeric materials. A sample part was printed with two different polymers shaped as a cube. The surface of the part is electroless plated with nickel (Ni). Subsequently, the desired conductive pattern is achieved by selectively removing the sacrificial material of the cube. The removal of the sacrificial material is conducted utilizing the swollen off method.

The Swollen-off process takes advantage of the absorption disparity between the two printed materials. As one of the materials absorbs markedly more solvent, it experiences larger hygroscopic swelling. This, in turn, causes high-stress concentrations at the interface between the two materials. The swollen material is then easily separated from the main body of the part, resulting in the metallic patterns formed on the polymeric surface of the 3D printed cube. Therefore, this process is capable of selectively metalizing 3D surfaces and internal cavities

5.2.1 Sample design

A 3D patterned cube was designed utilizing Computer-Aided Design (CAD) software and fabricated with a multi-material 3D printer (Objet260 Connex, Stratasys Ltd.). The base substrate was composed of a rigid material Vero White+ (VW+). Areas printed with VW+ will remain after the swollen-off procedure. While the sacrificial mask pattern was printed on Tango Plus (TP) a highly elastic polymer similar to silicone rubber. The line width and thickness of the TP patterns was 500 m.

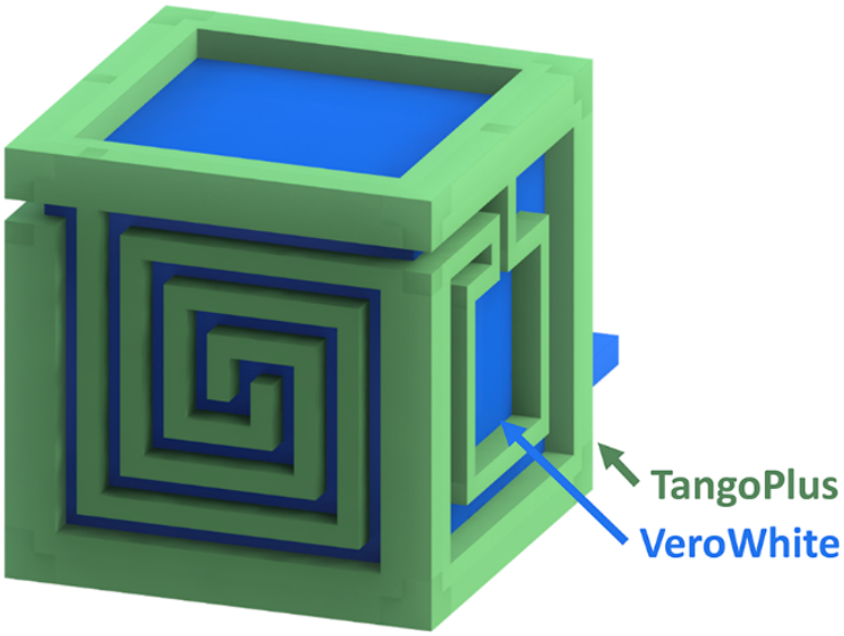

Figure 5.8. Swollen-off cube sample design

5.2.2 Sample preparation

After the post-processing of the printed part, the swollen-off process was conducted. This process consists of 2 steps, metalizing phase, adsorption and swollen off phase. The process is summarized in Fig 5.9 below.

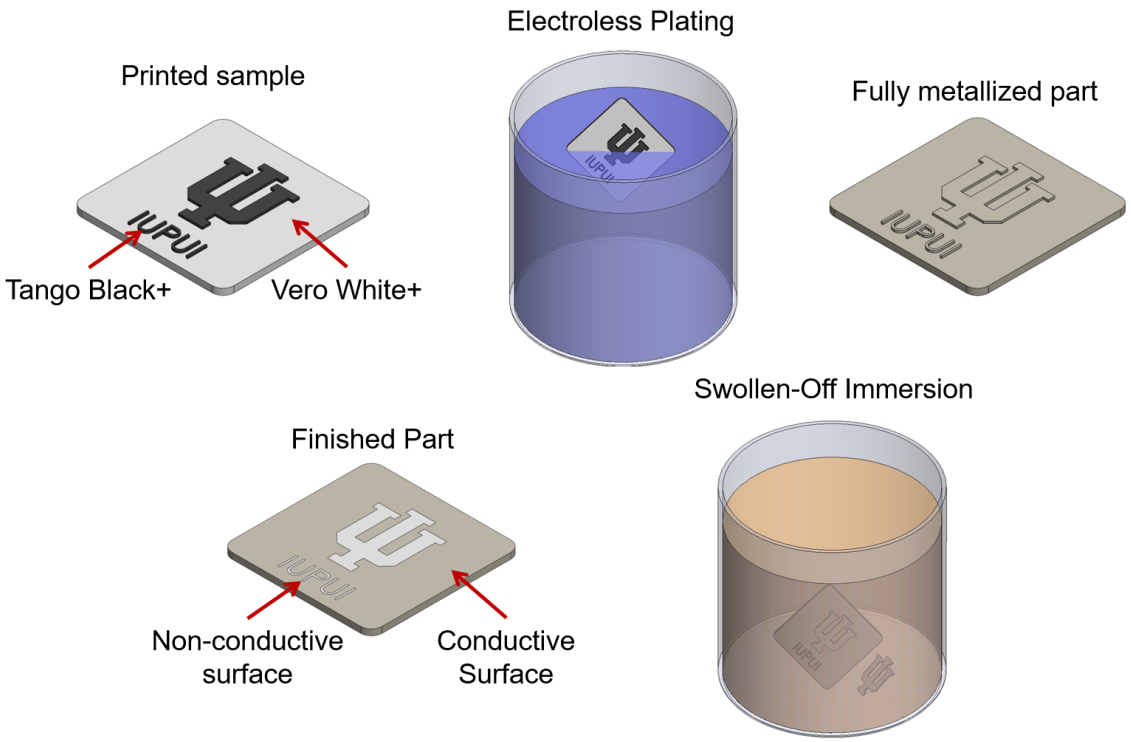

Figure 5.9. Schematic of the swollen-off process

Electroless Plating:

The surface of the printed cube is treated with an acidic etchant and dipped in a neutralizer for a minute prior to the electroless plating procedure. Subsequently, a Palladium (Pd) activator and an accelerator are employed as catalyst sites to initiate the electroless plating. Finally, electroless plating of Ni is conducted for 10 minutes with an adjusted pH of 9.

Adsorption and Swollen-off phase:

After the cube has been successfully plated the cube is immersed in ethanol for one hour. This causes the materials to absorb the ethanol, due to this adsorption the materials swell up. However, since the VW+ adsorbs markedly less than TP and therefore expands much less, the interface regions for the two materials are subjected to high concentrations of stress. The cube is then treated with ultrasonic bath to rinse off the ethanol and promote the separation of TP from the cube.

5.2.3 Swollen-off process results

The focus of this use case was to present a novel method for electroless plating on 3D printed structures. The Swollen-off, an evolution of the lift-off process commonly used in the micro-fabrication process. The Swollen-off process demonstrated in this section provides a simple way of producing electrical devices on complex 3D surfaces. This process was used to create conductive circuits 500 m wide made of nickel (Ni) on the surfaces of the 3D printed cube.

Fig. 5.10a shows the 3D printed cube composed of the TP patterns embossed on the surface of the VW cube. The successfully plated part is shown in Fig. 5.10B. TP layer is swollen-off after the immersion of the cube in ethanol for one hour (Fig. 5.10C). The VW areas covered with TP were left exposed after swollen-off process resulting in selectively patterned Ni trace. The Ni plating remains on the surface of the cube as shown in Fig. 5.10D.

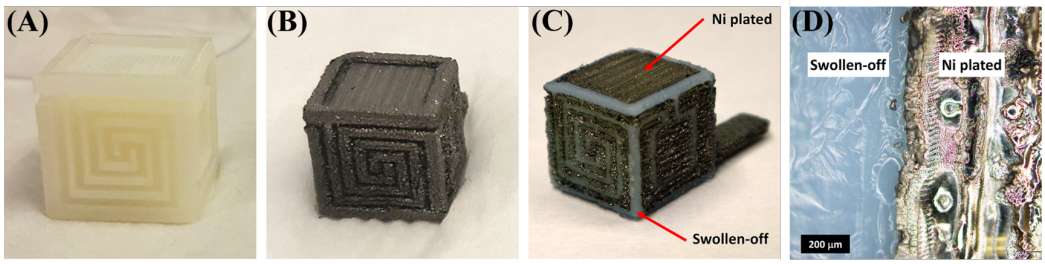

Figure 5.10. Results of the swollen-off process

6. SUMMARY, CONCLUSION AND RECOMMENDATIONS

6.1 Summary

The work involved in this study present the an analytical, experimental and numerical foundation for the use of multi-material parts printed with Material Jetting (MJ). Characterization of the mechanical properties and model fitting was successfully conducted for two of the most used base materials, Tango Black+ (TB+) and Vero White+ (VW+) and the composites printable from their mixture, DM40, DM50, DM60, DM70, DM85 and DM95.

6.1.1 Physical testing:

The initial step for the characterization of the MJ materials was physical testing. Standardized testing procedures as per the Korean standard (KS-M6518) were utilized to gather data on the stress-strain curves for all the materials. Section two details the entirety of the process as well as a summary of the mechanical properties of the materials. Additionally, Scanning Electron Microscopy (SEM) was utilized to study the fracture surfaces of all the test samples. The resulting images showed that the fracture surface for the two base materials is markedly different. Furthermore, it was shown that both the fracture surface and material properties of the DMs are more like those of TB+ than those of VW+.

6.1.2 Material models:

The resulting data gathered in section two was utilized in section three to fit the curves of all the tested samples into four different polynomial hyperelastic material models. The four different forms of the generalized Rivlin model used were:

The Neo-Hookean model (NH), the two-parameter Mooney Rivlin model (MR2), the three-parameter Mooney Rivlin model (MR3), and the five parameter Mooney Rivlin model (MR5). The constants for the material models as well as the derivation of the material models are summarized in section three. Additionally, empirical formulas for approximating the modulus of elasticity from Shore A hardness were also investigated. In the event that Stratasys releases new materials or allows for more customization on the DM mixtures, these empirical formulas provide an inexpensive and simple method for obtaining some information on the mechanical properties of the new materials.

6.1.3 Validation of the models:

In order to prove the accuracy of the newly fitted models, Finite Element Analysis (FEA) simulations were conducted replicating the physical test conditions. The comparison results are summarized in section four. Both MR3 and MR5 models were accurate up to 40% and able to model all the DMs, however at the cost of higher computational requirements and the increased risk of the simulation not converging. Meanwhile, MR2 model was able to accurately model the materials up to 25% strain. The NH model was capable of simulating all but DM95 up to 20% strain. One of the biggest advantages of printing DMs is the ability to tailor specific regions of a part with different material properties. Therefore, the accuracy of the simulations for multi-material parts was then validated. Four different multi-material samples were designed and printed. Subsequently, FEA simulations and physical tests were conducted and the resulting strain maps compared. The results showed that the models can accurately predict the deformation patterns of multi-material samples undergoing tensile strain.

6.1.4 Case studies

In section five, two case studies were used as examples of how MJ can improve the performance of several applications. In the first example, MJ was utilized to create customizable flexible elastic Printed Circuit Boards (PCBs) with rigid isolating regions that enable the use of rigid off-the-shelve surface mounted devices (SMDs). The second use case presented in this section was a novel process for creating 3 dimensional (3D) circuits. The Swollen-off process takes advantage of the absorption disparity between the two printed materials. The sacrificial material experiences larger hygroscopic swelling which in turn, causes high-stress concentrations at the interface between the two materials. Prior to the immersion of the part in the ethanol solution causing it to swell up, the part is electroless plated. Therefore, after the removal of the sacrificial material, the remaining object has a selectively patterned conductive surface.

6.2 Conclusion

Based on the work conducted in this study several conclusions can be made:

1. Initial characterization of the material properties of DMs printed with MJ can be achieved by conducting tensile tests utilizing engineering standards.

2. Different hyperelastic material models can be fitted with this data with significantly different levels of accuracy.

3. The Neo-Hookean model is applicable for simulations of small elongations for all but the most rigid material (DM95).

4. The Mooney-Rivlin two-parameter model can be used when a phenomenological model is acceptable and low strains will be simulated since this model fails to account for any stiffening effects.

5. The Mooney-Rivlin three and five parameter models accurately model the material properties of the DMs tested, and account for the stiffening effects.

6. The Mooney-Rivlin three and five parameter models are more computationally intensive and risk having convergence issues in certain applications.

7. The material models presented here can be utilized to simulate multi-material parts printed with MJ.

8. Novel substrates for flexible and elastic circuits can be easily designed utilizing these materials, additional stress relief regions can be included to facilitate the use of rigid off-the-shelf SMD components.

9. The difference in hygroscopic swelling can be leveraged to selectively separate materials co-printed with MJ, this, in turn, can be utilized to create conductive circuits in 3D as shown in the swollen-off process.

6.3 Recommendations

The material models fitted in this study provide multiple options for simulating DMs printed by MJ. The simulations conducted on both single and multi-material objects prove the validity of these models for both uses. Furthermore, the two use-cases presented in this work show novel ways to leverage this technology. Following are some suggestions for further research on this topic:

Complete characterization of other stress states: A method for improving the accuracy of the models presented in this study is by testing and characterizing the mechanical response to other stress states such as compression and shear. Advanced FEA software packages allow for the fitting of the material models from multiple stress-strain curves generated from different tests.

Study of the interface regions between different materials: In this study, it was shown that there is a small region in the junction between two distinct materials where some unintended mixing occurs. This creates a small interface region

with intermediate material properties, the extent of this mixing hasnt been fully characterized. Morphological analysis of this region through different means such as nano-indentation measurements and SEM analysis should be conducted to provide more insight into modeling of this region.

Characterization of other material properties: In the swollen-off case study it was shown the distinct hygroscopic swelling properties of the two materials could be leveraged to separate co-printed materials. This area of study should be expanded to all the other materials presented in this publication. Additionally, the thermal and dielectric properties of the DMs should be characterized and made available for wide use.

Focus on novel uses for these materials: The ability choose the material properties within a part at a micron scale allows for several benefits when creating new devices with this technology. Wearable devices would benefit from more organic interfaces between rigid components and the skin of the user, examples range from medical sensors, prosthetic devices, and virtual reality headsets to mention some.

REFERENCES

REFERENCES

[1] Jun Wu, Niels Aage, Ruediger Westermann, and Ole Sigmund. Infill optimization for additive manufacturing–approaching bone-like porous structures. *IEEE Transactions on Visualization and Computer Graphics*, page 1, 2017.

[2] C Lee Ventola. Medical applications for 3d printing: current and projected uses. *Pharmacy and Therapeutics*, 39(10):704, 2014.

[3] Wicher J Van Der Meer, Arjan Vissink, Yuan Ling Ng, and Kishor Gulabivala. 3d computer aided treatment planning in endodontics. *Journal of dentistry*, 45:67–72, 2016.

[4] David Anssari Moin, Wiebe Derksen, JP Verweij, Richard van Merkesteyn, and Daniel Wismeijer. A novel approach for computer-assisted template-guided autotransplantation of teeth with custom 3d designed/printed surgical tooling. an ex vivo proof of concept. *Journal of Oral and Maxillofacial Surgery*, 74(5):895–902, 2016.

[5] Jorge Zuniga, Dimitrios Katsavelis, Jean Peck, John Stollberg, Marc Petrykowski, Adam Carson, and Cristina Fernandez. Cyborg beast: a low-cost 3d-printed prosthetic hand for children with upper-limb differences. *BMC research notes*, 8(1):10, 2015.

[6] Brett Lyons. Additive manufacturing in aerospace: Examples and research outlook. *The Bridge*, 44(3), 2014.

[7] Jason J Dunn, David N Hutchison, Aaron M Kemmer, Adam Z Ellsworth, Michael Snyder, Willam B White, and Brad R Blair. 3d printing in space: enabling new markets and accelerating the growth of orbital infrastructure. *Proc. Space Manufacturing 14: Critical Technologies for Space Settlement. Space Studies Institute, 29–31 October 2010, Mountain View, CA*, 2010.

[8] Karl Willis, Eric Brockmeyer, Scott Hudson, and Ivan Poupyrev. Printed optics: 3d printing of embedded optical elements for interactive devices. In *Proceedings of the 25th annual ACM symposium on User interface software and technology*, pages 589–598. ACM, 2012.

[9] SF Busch, M Weidenbach, M Fey, F Schäfer, T Probst, and M Koch. Optical properties of 3d printable plastics in the thz regime and their application for 3d printed thz optics. *Journal of Infrared, Millimeter, and Terahertz Waves*, 35(12):993–997, 2014.

[10] Anthony K Au, Wilson Huynh, Lisa F Horowitz, and Albert Folch. 3d-printed microfluidics. *Angewandte Chemie International Edition*, 55(12):3862–3881, 2016.

[11] Philip J Kitson, Mali H Rosnes, Victor Sans, Vincenza Dragone, and Leroy Cronin. Configurable 3d-printed millifluidic and microfluidic lab on a chipreactionware devices. *Lab on a Chip*, 12(18):3267–3271, 2012.

[12] Halil L Tekinalp, Vlastimil Kunc, Gregorio M Velez-Garcia, Chad E Duty, Lonnie J Love, Amit K Naskar, Craig A Blue, and Soydan Ozcan. Highly oriented carbon fiber–polymer composites via additive manufacturing. *Composites Science and Technology*, 105:144–150, 2014.

[13] Fuda Ning, Weilong Cong, Jingjing Qiu, Junhua Wei, and Shiren Wang. Additive manufacturing of carbon fiber reinforced thermoplastic composites using fused deposition modeling. *Composites Part B: Engineering*, 80:369–378, 2015.

[14] Ryan Hahnlen and Marcelo J Dapino. Niti–al interface strength in ultrasonic additive manufacturing composites. *Composites Part B: Engineering*, 59:101–108, 2014.

[15] Collin Ladd, Ju-Hee So, John Muth, and Michael D Dickey. 3d printing of free standing liquid metal microstructures. *Advanced Materials*, 25(36):5081–5085, 2013.

[16] Simon J Leigh, Robert J Bradley, Christopher P Purssell, Duncan R Billson, and David A Hutchins. A simple, low-cost conductive composite material for 3d printing of electronic sensors. *PloS one*, 7(11):e49365, 2012.

[17] Hsien-Hsueh Lee, Kan-Sen Chou, and Kuo-Cheng Huang. Inkjet printing of nanosized silver colloids. *Nanotechnology*, 16(10):2436, 2005.

[18] André Luiz Jardini, Maria Aparecida Larosa, Rubens Maciel Filho, Cecília Amélia de Carvalho Zavaglia, Luis Fernando Bernardes, Carlos Salles Lambert, Davi Reis Calderoni, and Paulo Kharmandayan. Cranial reconstruction: 3d biomodel and custom-built implant created using additive manufacturing. *Journal of Cranio-Maxillofacial Surgery*, 42(8):1877–1884, 2014.

[19] Vladimir Mironov, Thomas Boland, Thomas Trusk, Gabor Forgacs, and Roger R Markwald. Organ printing: computer-aided jet-based 3d tissue engineering. *TRENDS in Biotechnology*, 21(4):157–161, 2003.

[20] Vladimir Mironov, Richard P Visconti, Vladimir Kasyanov, Gabor Forgacs, Christopher J Drake, and Roger R Markwald. Organ printing: tissue spheroids as building blocks. *Biomaterials*, 30(12):2164–2174, 2009.

[21] Lawrence E Murr, Sara M Gaytan, Edwin Martinez, Frank Medina, and Ryan B Wicker. Next generation orthopaedic implants by additive manufacturing using electron beam melting. *International journal of biomaterials*, 2012:14, 2012.

[22] Jayson Paulose, Anne S Meeussen, and Vincenzo Vitelli. Selective buckling via states of self-stress in topological metamaterials. *Proceedings of the National Academy of Sciences*, 112(25):7639–7644, 2015.

[23] TR Jackson, H_ Liu, NM Patrikalakis, EM Sachs, and MJ Cima. Modeling and designing functionally graded material components for fabrication with local composition control. *Materials & Design*, 20(2):63–75, 1999.

[24] Peter Fratzl. Biomimetic materials research: what can we really learn from nature9s structural materials? *Journal of the Royal Society Interface*, 4(15):637–642, 2007.

[25] Mahmoud Nemat-Alla. Reduction of thermal stresses by developing two-dimensional functionally graded materials. *International Journal of Solids and Structures*, 40(26):7339–7356, 2003.

[26] Jeffery Roesler, Glaucio Paulino, Cristian Gaedicke, Amanda Bordelon, and Kyoungsoo Park. Fracture behavior of functionally graded concrete materials for rigid pavements. *Transportation Research Record: Journal of the Transportation Research Board*, (2037):40–49, 2007.

[27] Ian Gibson, David Rosen, and Brent Stucker. *Additive manufacturing technologies: 3D printing, rapid prototyping, and direct digital manufacturing*. Springer, 2014.

[28] Jeffrey W Stansbury and Mike J Idacavage. 3d printing with polymers: Challenges among expanding options and opportunities. *Dental Materials*, 32(1):54–64, 2016.

[29] H Bikas, Panagiotis Stavropoulos, and George Chryssolouris. Additive manufacturing methods and modelling approaches: a critical review. *The International Journal of Advanced Manufacturing Technology*, 83(1-4):389–405, 2016.

[30] Tomaž Brajlih, I Drstvensek, M Kovacic, and J Balic. Optimizing scale factors of the polyjet rapid prototyping procedure by genetic programming. *Journal of achievements in materials and manufacturing engineering*, 16(1-2):101–106, 2006.

[31] Michael W Barclift and Christopher B Williams. Examining variability in the mechanical properties of parts manufactured via polyjet direct 3d printing. In *International Solid Freeform Fabrication Symposium*, pages 6–8, 2012.

[32] Lindsey Bass, Nicholas A. Meisel, and Christopher B. Williams. Exploring variability of orientation and aging effects in material properties of multi-material jetting parts. *Rapid Prototyping Journal*, 22(5):826–834, 2016.

[33] P Gay, D Blanco, F Pelayo, A Noriega, and P Fernández. Analysis of factors influencing the mechanical properties of flat polyjet manufactured parts. *Procedia Engineering*, 132:70–77, 2015.

[34] Jochen Mueller, Kristina Shea, and Chiara Daraio. Mechanical properties of parts fabricated with inkjet 3d printing through efficient experimental design. *Materials & Design*, 86:902–912, 2015.

[35] Emily Cleary Mikkelson. *Characterization and Modeling of the Thermal Properties of Photopolymers for Material Jetting Processes*. PhD thesis, Virginia Tech, 2014.

[36] W Jacob Monzel, Brad W Hoff, Sabrina S Maestas, David M French, and Steven C Hayden. Dielectric breakdown of additively manufactured polymeric materials. *IEEE Transactions on Dielectrics and Electrical Insulation*, 22(6):3543–3549, 2015.

[37] Aitor Cazón, Paz Morer, and Luis Matey. Polyjet technology for product prototyping: Tensile strength and surface roughness properties. *Proceedings of the Institution of Mechanical Engineers, Part B: Journal of Engineering Manufacture*, 228(12):1664–1675, 2014.

[38] Jacob P Moore and Christopher B Williams. Fatigue properties of parts printed by polyjet material jetting. *Rapid Prototyping Journal*, 21(6):675–685, 2015.

[39] Stanisław Adamczak, Jerzy Bochnia, and Bożena Kaczmarska. An analysis of tensile test results to assess the innovation risk for an additive manufacturing technology. *Metrology and Measurement Systems*, 22(1):127–138, 2015.

[40] David Blanco, Pelayo Fernandez, and Alvaro Noriega. Nonisotropic experimental characterization of the relaxation modulus for polyjet manufactured parts. *Journal of Materials Research*, 29(17):1876–1882, 2014.

[41] Shanmugam Kumar, Brian L Wardle, and Muhamad F Arif. Strength and performance enhancement of bonded joints by spatial tailoring of adhesive compliance via 3d printing. *ACS applied materials & interfaces*, 9(1):884–891, 2016.

[42] David Moinina Sengeh and Hugh Herr. A variable-impedance prosthetic socket for a transtibial amputee designed from magnetic resonance imaging data. *JPO: Journal of Prosthetics and Orthotics*, 25(3):129–137, 2013.

[43] EL Doubrovski, Elizabeth Yinling Tsai, Daniel Dikovsky, Jo MP Geraedts, Hugh Herr, and Neri Oxman. Voxel-based fabrication through material property mapping: A design method for bitmap printing. *Computer-Aided Design*, 60:3–13, 2015.

[44] Andrew T Gaynor, Nicholas A Meisel, Christopher B Williams, and James K Guest. Multiple-material topology optimization of compliant mechanisms created via polyjet three-dimensional printing. *Journal of Manufacturing Science and Engineering*, 136(6):061015, 2014.

[45] Robert MacCurdy, Jeffrey Lipton, Shuguang Li, and Daniela Rus. Printable programmable viscoelastic materials for robots. In *Intelligent Robots and Systems (IROS), 2016 IEEE/RSJ International Conference on*, pages 2628–2635. IEEE, 2016.

[46] Nicholas W Bartlett, Michael T Tolley, Johannes TB Overvelde, James C Weaver, Bobak Mosadegh, Katia Bertoldi, George M Whitesides, and Robert J Wood. A 3d-printed, functionally graded soft robot powered by combustion. *Science*, 349(6244):161–165, 2015.

[47] Leon S Dimas, Graham H Bratzel, Ido Eylon, and Markus J Buehler. Tough composites inspired by mineralized natural materials: computation, 3d printing, and testing. *Advanced Functional Materials*, 23(36):4629–4638, 2013.

[48] Theresa Swetly, Jürgen Stampfl, Gero Kempf, Rainer-Michael Hucke, Marcus Willing, and Marina Warkentin. Bioinspired engineering polymers by voxel-based 3d-printing. *BioNanoMaterials*, 17(3-4):145–157, 2016.

[49] M Mooney. A theory of large elastic deformation. *Journal of applied physics*, 11(9):582–592, 1940.

[50] Ronald S Rivlin and DW Saunders. Large elastic deformations of isotropic materials. vii. experiments on the deformation of rubber. *Philosophical Transactions of the Royal Society of London A: Mathematical, Physical and Engineering Sciences*, 243(865):251–288, 1951.

[51] RS Rivlin. Large elastic deformations. In *Collected Papers of RS Rivlin*, pages 318–351. Springer, 1997.

[52] TYP Chang, AF Saleeb, and G Li. Large strain analysis of rubber-like materials based on a perturbed lagrangian variational principle. *Computational mechanics*, 8(4):221–233, 1991.

[53] Majid Shahzad, Ali Kamran, Muhammad Zeeshan Siddiqui, and Muhammad Farhan. Mechanical characterization and fe modelling of a hyperelastic material. *Materials Research*, 18(5):918–924, 2015.

[54] Nomesh Kumar and V Venkateswara Rao. Hyperelastic mooney-rivlin model: Determination and physical interpretation of material constants. *Parameters*, 2(10):01, 2016.

[55] K Larson. Can you estimate modulus from durometer hardness for silicones. *Dow Corning Corporation*, pages 1–6, 2016.

[56] Iranthi M Meththananda, Sandra Parker, Mangala P Patel, and Michael Braden. The relationship between shore hardness of elastomeric dental materials and young's modulus. *Dental materials*, 25(8):956–959, 2009.

[57] Alan N Gent. On the relation between indentation hardness and young's modulus. *Rubber Chemistry and Technology*, 31(4):896–906, 1958.

[58] HJ Qi, K Joyce, and MC Boyce. Durometer hardness and the stress-strain behavior of elastomeric materials. *Rubber chemistry and technology*, 76(2):419–435, 2003.